COMPUTATIONAL SIMULATIONS OF SHEAR BHAVIOUR OF JOINTS IN BRITTLE GEOMATERIALS

Qifeng Yu

October, 2001

Department of Civil Engineering and Applied Mechanics
McGill University, Montreal

Thesis submitted to the Faculty of Graduate Studies and Research in partial fulfillment of the requirements of the degree of

Master of Engineering

(Geomechanics and Geotechnical Engineering)

0-612-79106-8

ABSTRACT

The mechanical behavior of fractures in geological media is important to geotechnical and geoenvironmental engineering. Considerable investigations have been conducted on, firstly, the characterization of the fracture topography and secondly, on the assessment of the influence of fracture topography on the mechanical behavior, particularly the dilatancy of the discontinuity. The studies of the mechanical behavior of fracture surfaces have invariably been concerned with the examination of the mechanics of the contact surfaces, to the virtual exclusion of the progress of failure zones into regions adjacent to the contacting fracture surfaces. This thesis conducts a computational assessment of the role of geomaterial plasticity and surface topography on the behavior of a fracture. The computational modelling takes accounts of the irregularity of the joint surface, the frictional and elasticity characteristics of the contact zones, the elasto-plastic failure of the material and incompatible deformations that arise during shear of an irregular fracture surface. The computational shear responses are compared for the cases where a regular fracture surface exhibits identical shear behavior in the presence of geomaterial plasticity. For an irregular joint, it is observed that the shear behavior is relatively unaffected by material plasticity. Variation of dilatancy with shear cycles, however, can be directly attributed to the presence of material plasticity. Plastic energy dissipation is related to the normal restraints specified. Shear behavior of a specific joint appears to depend mainly on the interfacial behavior of the limited number of asperity contact during shear. The surface geometry of these asperities governs the dilatancy and their slopes control the peak shear resistance. The thesis also examines briefly the influence of initial separation of joints on the shear behavior.

RÉSUMÉ

Le comportement mécanique des fractures dans les milieux rocheux a une importance considérable pour la conception d'ouvrages geotechniques. De nombreuses investigations ont été conduites, en premier lieu, pour carāctériser la topograhie, des surfaces, puis pour analyser l'īnfluence de la morphologie sur le comportement mécanique des joints rocheux, plus particulierement sur la dilatance. Le comportement mécanique des joints rocheux est, le plus souvent, étudié grâce à la mécanique de contact, sans prendre en compte la propagation des fractures qui se produisent dans les zones à proximité de ces zones de contact. Dans cette thèse, le rôle du comportement plastique des geomateriaux et de la morphologie des surfaces sur le comportement mécanique des joints rocheux, est etudié de manīere numérique. Un modèle numérique prenant en compte les irrégularités de la surface des joints, les paramètres mécaniques tels que le coefficient de frottement et l'élasticité des zones de contact et les déformations incompatibles qui resultent du cisaillement des joints rocheu. Des surfaces régulières et irregulières ont été testeés, et les résultats ont été comparés dans le cas de matériaux plastique. Il y a aussi été observé que le comportement en cisaillement et peu affecté par le fait que le matériaux a un comportement élastoplastique en le comparant aux résultats obtenus pour les materiaux élastiques. Cependant, la variation de la dilatance pour un essai cyclique de cisaillement peut être directement attributée à la présence de materiaux aux comportement plastique. La dissipation de l'energie plastique est liée aux conditions aux limites dans la direction normale du joint. Le comportement en cisaillement semble dépendre directement du comportement mécanique des asperités localiseés dans les zones de contact. La géomètrie de ces asperités gouverne la dilatance et leurs pentes controlent l'intensité du pic de cisaillement. L'influence de l'ouverture initiale des joints est aussi étudiée pour mieux comprendre le comportement mécanique des joints.

ACKNOWLEDGEMENTS

The author wishes to express his great gratitude to his supervisor, Professor A.P.S. Selvadurai, Department of Civil Engineering and Applied Mechanics, McGill University, for suggesting the research topic, his extensive guidance and support.

The author would also like to thank to Dr. G. Armand, Post Doctoral Fellow and Mr. A. Shirazi, doctral student at Department of Civil Engineering and Applied Mechanics, McGill University, for their assistance and useful discussions. Thanks are also due to Professor J. Nemes, Department of Mechanical Engineering, McGill University, for making available the ABAQUS software. The author acknowledges the assistance of Dr. W.D. Cook, Department of Civil Engineering and Applied Mechanics, McGill University, with regard to computer facilities at geomechanics laboratory. The research described in the thesis was supported through an NSERC Operating Grant awarded to Professor A.P.S. Selvadurai.

Finally, the author wishes to thank his family, relatives and friends for their understanding, support and encouragement during the course of this work.

TABLE OF CONTENTS

LIST OF FIGURES

Chapter 1

JOINTS IN BRITTLE GEOMATERIALS

1.1 Joints in brittle materials

The development of brittle fracture in an intact material or at the bond of two distinct materials leads to the development of discontinuities (Figure 1.1). A planar discontinuity between two material regions with similar or identical mechanical properties can be defined as a joint (Figure 1.2). Joints in brittle geomaterials, such as rock and concrete, will exhibit quite similar mechanical behavior primarily due to their brittle character.

Load transfer at joints constitutes an important aspect of the study of brittle materials in contact. Geotechnical stability of excavations in rock, cracked concrete, flow and transport of fluid and chemicals through materials are also influenced by the mechanical behavior of the joints.

In current usage, the term interface, which, in the context of the study of geomaterials, is usually regarded as the physical boundary between dissimilar materials, is also sometimes used to signify a joint (see e.g. Selvadurai and Boulon, 1995).

Figure 1.1 A single shear fracture in Westerly granite [after Friedman et al. (1970)].

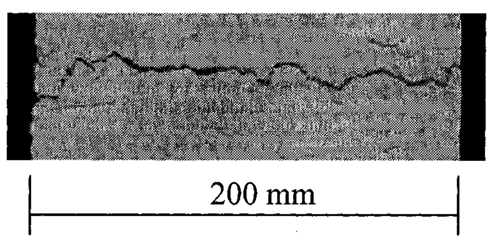

Figure 1.2 A joint in Limestone [after Armand (2000)]

1.2 Review of research of rock joints

It is generally accepted that, strength, deformability and fluid flow characteristics of rock joints depend on the roughness of the joint. Characterisations of joint surfaces have been extensively treated by a number of researchers. Patton (1966) idealized the random joint profile as a regular 'saw-tooth' profile. He defined a asperity angle to propose a Mohr-Coulomb-type bilinear model of a shear strength criterion: at low normal stresses, the joint shows dilatancy due to overriding of the asperities; at high stresses, shear failure can occur through intact material in asperities. Barton (1971, 1973, 1976) examined the effect of the roughness on the peak shear strength and proposed a *JRC* value (Joint Roughness Coefficient) to aid his analysis. The joint roughness was then simply characterized as an empirical value, which can be determined either in laboratory or *in situ*. The procedure for determining *JRC* is given in ISRM (1978). This empirical determination of *JRC* is quite subjective and the value for a same 3D profile differs at different scales (Bandis, 1981) and in different directions of shearing. Therefore in addition to the implementation of *JRC* value, some conventional statistical methods have been used to supplement the joint characterization. Among such studies are those given by Wu and Ali (1978), Tse and Cruden (1979), Krahn and Morgenstern (1979), Dight and Chiu (1981), and Maerz et al. (1990). The limitations of both *JRC* and the conventional statistical method have also been pointed out by Maerz et al. (1990), Miller et al. (1990), Kulatilake et al. (1995), Wakabayashi and Fugushige (1995), and Kodikara and Johnston (1994). In an attempt to avoid directional dependence and scale effects, fractal methods, that characterize the concept of self-similarity and self-affinity, have been vigorously accepted by many researchers (see e.g. Brown, 1985; Matsushita and Luchi, 1989; Malinverno, 1990; Miller et al., 1990; Power et al., 1991; Huang et al., 1992; Odling, 1994; den Outer et al., 1995; Lee, 1997; Kulatilake et al., 1995; Shirono and Kulatilake, 1997). A number of methods have been suggested for estimation of the fractal parameters for joints. There include the divider (Mandelbrot, 1983), box counting (Feder, 1988), variogram (Orey, 1970), spectral (Berry, 1980), and roughness length

(Malinverno, 1990). The trends linking fractal parameters with various mechanical parameters of rock joints have been studied by Brown and Scholz (1985), Turk et al. (1987), Lee et al. (1990), Maerz et al. (1990), Huang et al. (1992), Xie et al. (1993, 1994, 1997a), Odling (1994), den Outer et al. (1995), Kwasniewski and Wang (1993), Bobji et al. (1999). Kwafniewski and Wang (1997) have examined the damage process of joint surface during shear. A law for surface morphology evolution, based on fractal method, has been developed by these researchers to predict the changes of surface as functions of the plastic work (see also Nguyen and Selvadurai, 1998). Further information on the evolution of rock joint morphology during shear are given by Sabbadini et al. (1994, 1995), and Homand-Etienne et al. (1995). Xie et al. (1997b) examined the stress fields near fractal joints during compression and shear using photoelastic method. Roughness was found to be an important factor affecting the stress field. Re et al. (1997) explored the mechanisms underlying scale effect by focusing in particular on the variation in the contact areas as a function of joint size using fractal analysis. Fox et al. (2000) recently presented the effect of roughness on multi-cycle dynamic shear behavior of a natural rock joint. Gentier et al. (2000) recently also examined influence of fracture geometry on shear behavior and established a strong link between them. They described results from a series of shear tests performed on identical cement mortar replicas formed from a natural granite fractures. Mechanical parameters measured during experiments varied depending on the shear direction. Using a three-directional geostatistical method of fracture surface characterization, they analyzed the dependence of size and location of damage zones on local geometry and proposed an algorithm.

Materials such as clay, silt and fine sand which infiltrate rock joints are expected to reduce the overall shear strength of the joint. Many laboratory tests on infilled joints have been conducted under constant normal stress (see e.g. Goodman, 1970; Kanji, 1974; Ladanyi and Archambault, 1977; Lama, 1978; Barla et al., 1985; Pereira, 1990; Phien-wej et al., 1990; Toledo and de Freitas, 1992). Pereira (1997) used rotary shear tests to investigate the stress change near the rock surface during shear. When the shear load was applied, the stress field changed continuously during the test on an unfilled joint, due to the removal of the asperities from the rock surfaces. For filled discontinuities this re-orientation of the stress field became less probably since not many asperities had been damaged during the shear process. Indraratna (1999) recently performed tests on some filled regular triangular joints under constant normal stiffness. Appearance of additional normal stiffness causes a greater suppression of dilatancy and leads to higher shear stresses than those results obtained under constant normal stress. The failure intersected the asperity when fill height was less than asperity height; it only passed through the fill material when the ratio of fill height and asperity height was greater than some critical value, which varies from about 1.4 to 1.8.

A clear understanding of the mechanism of fluid movements through joints becomes necessary for the study of geoenvironmental problems. The cubic law of hydraulic permeability of a joint surface is developed from the classic "parallel plate model". The applicability of the cubic law to flow through fractures has been explored experimentally and analytically, such as by Snow (1965), Iwai (1976), Gangi (1978), Witherpoon et al. (1980), Engelder (1981), Raven and Gale (1985), Pyrak-Nolte et al. (1987), Tsang (1987), Zimmerman et al. (1991), Iwano and Einstein (1995), Durham and Bonner (1995) and Selvadurai (2000). Deviations from cubic law, which stems from surface roughness, were examined by Kranz et al. (1979), Raven and Gale (1985), Brown (1987) and Boulon et al. (1993).

Mechanical deformation of a rock joint results in changes to its aperture and consequently its hydraulic conductivity. The behaviour of fluid flow can be coupled with evolution of normal stress and closure of joint. Most of the modelling and experiments conducted in connection with hydromechanical coupling problems were performed mainly under normal loading conditions (Raven and Gale, 1985; Gentier, 1986; Billaux and Gentier, 1990; Amadei and Illangasekare, 1992). Modelling of these couplings requires a precise characterization of joint roughness morphology. Pyrak-Nolte and Morris (2000) found that the fluid flow through a single fracture subjected to normal stress was dependent on spatial correlation of the aperture distribution. In the case of shear loading conditions, the modelling of hydromechanical coupling is much more complex and difficult. Relevant experimental investigations have been made by Makurat et al. (1990), Olsson and Brown (1993), Esaki et al. (1996, 1999) and Yeo (1998). The tests by Esaki et al. (1999) revealed that, the change of permeability of the joint was approximately similar to that of the change in its dilatancy. Initially there was some permeability decrease due to the closing of contact points and then the permeability increased rapidly due to the increase of dilatancy. Chen et al. (2000) performed experiments to investigate the influence of shear displacement and normal stress on the mechanical and hydraulic behavior of rock joints. Dilatancy induced by shear displacement significantly enhanced the permeability of joints at high normal stress up to $40\,\mathrm{MPa}$. It was reported that equation proposed by Willis-Richard et al. (1996) underestimated dilatancy angle while the model by Barton et al. (1985) overestimated results for shear on joints with low-*JRC* and underestimated them for shear on joints with high-*JRC*.

The experimental research on rock joints have been complemented and aided by the development of computational approaches. In the early approaches to such modelling, the finite element method featured prominently. Finite element analysis of rock joints is often made through implementation of joint or interface elements. Goodman (1968) proposed the first interface element specially developed for modelling rock joints. Gens (1995) gave a classification of these elements: the link element (Frank, 1982; Ahmad et al., 1987), continuum finite elements of small but finite thickness (Zienkiewicz et al., 1970; Desai, 1984; Schiweiger et al., 1990) and zero thickness joint or interface elements (Goodman, 1968; Carol, 1983). Also many investigators have proposed constitutive models of interfaces for finite element implementation to account for dilatancy, normal stress and shear displacement. Roberds and Einstein (1978), using Patton (1966)'s yielding criterion, proposed a comprehensive model to include shear, dilatancy and normal stress. Desai et al. (1985) introduced a non-linear elastic model. Fishman and Desai (1987) developed an elasto-plastic constitutive model for the hardening behavior of rock joints using associative and non-associative flow rules. The same model was modified by Navayogarajah et al. (1992) to account for monotonic and cyclic behavior of interfaces. Plastic deformation can be divided into a slip component and damage component. Fakharian and Evgin (2000) adopted this model to numerically simulate 3D behavior of interface under various normal boundary conditions. Plesha (1987) considers a rough joint element with normal stiffness and shear stiffness. Important aspect of asperity degradation was considered in this model in that the decrease of dilatancy angle is in an exponential relationship with total plastic energy dissipation. Nguyen and Selvadurai (1998) implemented this model in their finite element code FRACON to examine computationally asperity degradation, permeability evolution during dilatancy and shearing of joints in geomaterial. In addition to finite element method, recent numerical research has featured the promising development of other approaches in analysis of interfaces or joints in geomaterials, which includes the boundary element method (Banerjee and Butterfield, 1981; Crouch and Starfield, 1983; Selvadurai, 1995; Selvadurai and Au, 1987; Grabinsky and Kamaleddine, 1997), the distinct element method (Cundall, 1971; Cundall and Strack, 1979; Williams et al., 1985, 1993; Pande et al., 1992; Selvadurai and Sepehr, 1997, 1998, 1999) and the discontinuous deformation analysis method (Shi, 1988; Maclaughlin and Sitar, 1996; Ohnishi et al., 1996).

1.3 Scope of the thesis

In the conventional analysis of joint behavior, attention is usually restricted to the non-linear contact behavior between surfaces composing the joints. With certain types of rocks or other brittle geomaterials, failure in the form of plastic flow and brittle fracture can also extend to the regions in the proximity of the joints. The scope of this research work is to use existing documented computational methodologies to examine the manner in which the non-linear process in regions adjacent to the joint surfaces can influence the overall shear behavior of the joints. The availability of computational methodologies, which accommodate for elastic-plastic frictional model and finite sliding formulations, makes it possible to account for discontinuous displacement at joints.

Chapter 2

GEOMECHANICAL BEHAVIOR OF ROCK JOINTS

The majority of current rock joint models are capable of predicting the shear behavior of joint surfaces with relatively simplified surface topography. Many of these do not take account of complex surface characteristics. Tentative quantitative description of roughness, which greatly influences shear behavior and hydraulic conductivity of rock joints, has been paid more attention with the help of graphical, statistical and fractal methods. This has led to a better understanding of complex shear mechanism and its relation to joint roughness.

2.1 Characterization of joint surface roughness

Patton (1966) performed experiments on artificial plaster joints with regular 'saw-tooth' profile, as shown in Figure 2.1. He proposed a Mohr-Coulomb-type bilinear model as the failure criterion for the joint. At low normal stresses, the joint shows dilatancy due to overriding of the asperities and at higher stresses, dilatancy is suppressed and shear through intact material is observed. Huang (1990), in his multi-cyclic shear tests conducted under constant normal stress and one-cycle shear test conducted under constant normal displacement, also observed the phenomenon of shear through intact material in asperities.

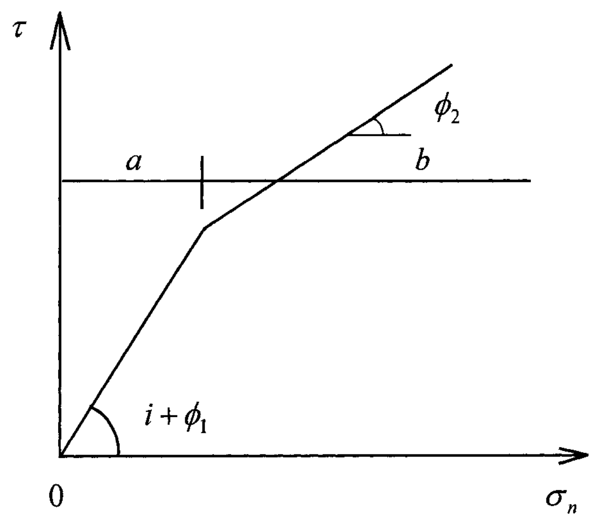

a: Relative movement at joint during asperity over-ride

b: Relative movement during shear through asperities

i : Asperity angle

ϕ_1 : Friction angle for the joint

ϕ_2 : Friction angle for the material

(a). Bilinear peak shear strength criterion

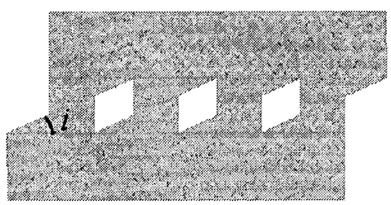

(b). Relative movement at joint during asperity over-ride

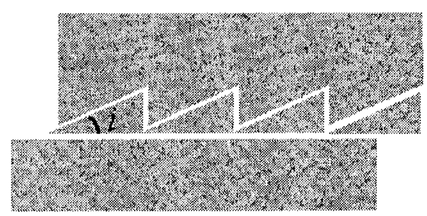

(c). Relative movement during shear through asperities

Figure 2.1 Bilinear peak shear strength [after Patton (1966), Goodman (1976), and Brady and Brown (1993)].

Real joints have spatially irregular profiles. Barton (1971, 1973, 1976) has examined the effect of roughness of the irregular profile on the peak shear strength. The irregular joint roughness was simplified as a value of *JRC* (Joint Roughness Coefficient), and the angle of inclination of the asperities (as defined in Patton's model) was replaced by a dilatancy angle $JRC\log_{10}[JCS/\sigma_n]$, which dependeds on normal stress σ and compressive strength of the joint surface defined as JCS. These coefficients *JRC* (Joint Roughness Coefficient) and *JCS* (Joint Compressive Strength) can be empirically and visually determined in laboratory or *in situ*. The procedures are described by ISRM (1978). The Figure 2.2 illustrates the *JRC* values and corresponding joint profiles.

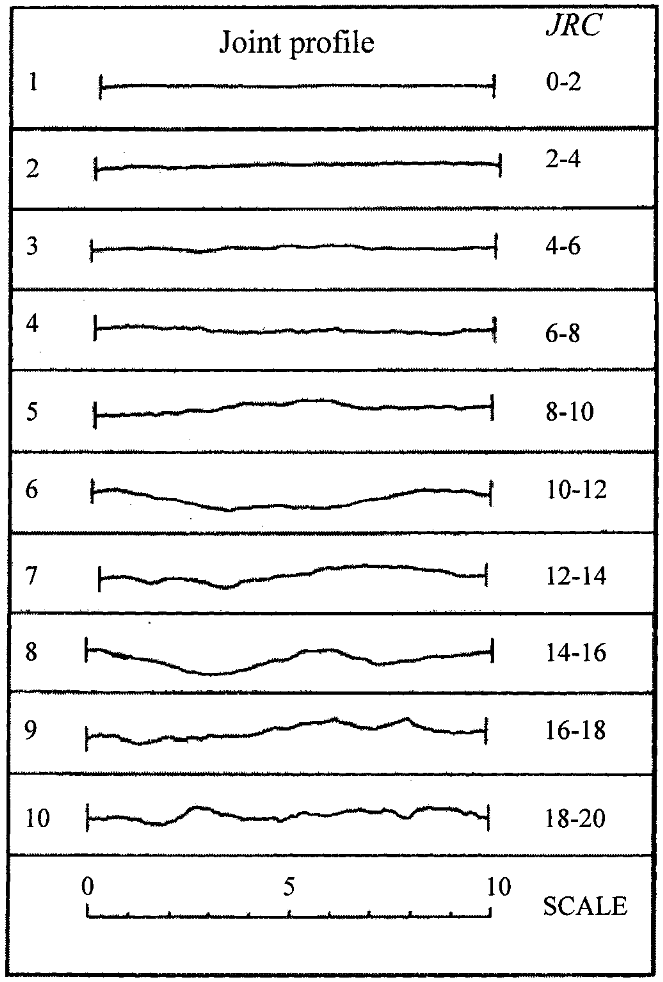

Figure 2.2 *JRC* and joint profiles [after Barton (1971, 1973, 1976)]

The empirical determination of the *JRC* value is prone to subjectivity and will depend on the direction of shearing (Huang and Doong, 1990; Jing et al., 1992). For this reason, some researchers have investigated methods with direction independent information obtained through statistical analysis. Examples of these are given by Tse and Cruden (1979), Roberds et al. (1990), and Yu and Vayssade (1991). The use of fractal methods for joint characterization is also discussed by Lee et al. (1990), and Seidel and Haberfield (1995).

For example, Seidel and Haberfield (1995) described the fractal parameters of roughness and their relation to shear behavior. It was concluded that, if the asperity angle followed a Gaussian distribution, the mean angle statistic $\overline{\theta}$ was related to standard deviations of angle s_θ through the relationship $s_\theta = \sqrt{\frac{\pi}{2}}\left|\overline{\theta}\right|$; s_θ is also related to fractal parameters of joint through approximate relation $s_\theta \approx \cos^{-1}(N^{(1-D)/D})$, where D is the fractal dimension of joint and N is the number of equal length chords, into which the joint length L is divided. A typical comparison between s_θ and *JRC* is shown in Figure 2.3.

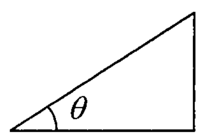

Idealized triangular asperity

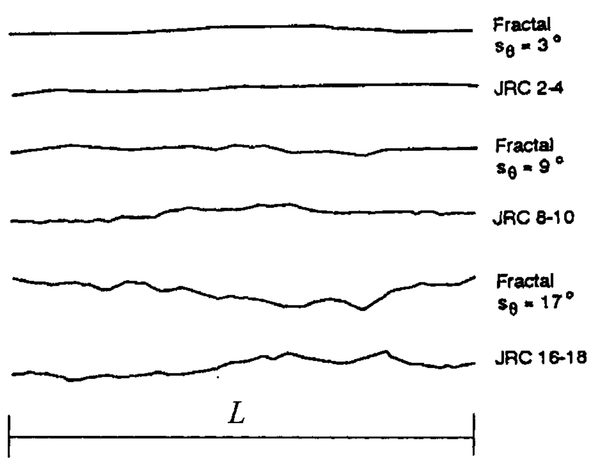

Figure 2.3 *JRC* and fractal profile [after Seidel and Haberfield (1995)]

2.2 Asperity behavior

Roughness or frictional characteristics of the joint surfaces influence their mechanical behavior. Shear load can only be transferred through asperity contact. Deformation or damage of surfaces in contact and asperities in contact can influence the mechanical behavior of rock joints.

The mechanical behavior of asperities is governed by the constitutive behavior of the parent geomaterials. Failure in form of plastic flow and brittle failure can extend to the regions near joints. Handanyan et al. (1990) pointed out three modes of asperity failure in their paper: these include (i) shearing of asperities (ii) the elastic or plastic deformation and eventually sliding at the asperities and (iii) the tensile splitting of asperities. The failure modes are schematically illustrated in Figure 2.4 (a). The model material used in their tests was used as a synthetic gypsum which exhibited linear elastic behavior in both unconfined compressive testing and direct tension testing and had medium strength and average modulus characteristics of a medium strength igneous rock. Handanyan et al. (1990) obtained the failure planes for three formed asperities, as shown in Figure 2.4(b).

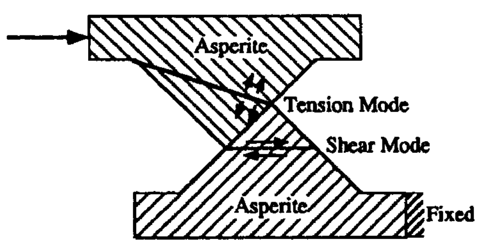

(a). Failure modes

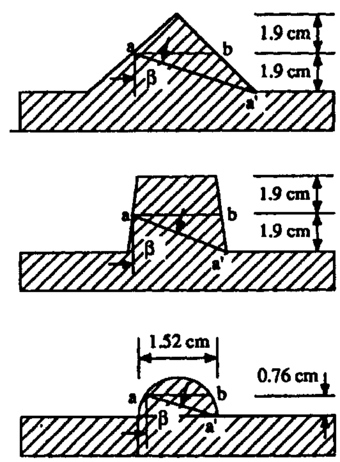

(b). Failure planes in various shaped asperities

Figure 2.4 Failure of asperities [after Handanyan et al. (1990)]

2.3 Three modes of testing

Sliding of potentially unstable rock blocks is restrained between two parallel dilatant rock joints (Figure 2.5). The joint exhibits dilatancy due to overriding at asperities. When dilation of the rock joints during shearing is constrained or partially constrained, an increase in the normal stress over the shear plane occurs, which increases the shear resistance of joints. Normal stress is a monotonic incremental function of $\phi(k,v')$ that satisfies that $\phi(0,v') = \phi(k,0) = 0$, where k is the stiffness of surrounding rock mass and v' is the dilatancy. Experimental techniques provide the most reliable methods for the investigation of the mechanics of rock joints. In experiments involving rock joints, the experimentation can follow three different modes of testing (Figure 2.6). There include experiments conducted under conditions where (i) the plane of the joint is subjected to a constant normal stress or (ii) the plane of the joint is subjected to a constant normal stiffness and where (iii) the joint is constrained from movement normal to its plane. The shear test under normal stiffness more realistically provides the shear behavior of natural joints in a sense that it considers the contribution of rock mass stiffness of k on the shear behavior. Test conducted under constant normal stress, which is a limit case of a test under constant normal stiffness when $k = 0$, yields shear strength too low for practical situations (Goodman, 1976). Shear under constant normal displacement represents the limit case when $k \to \infty$.

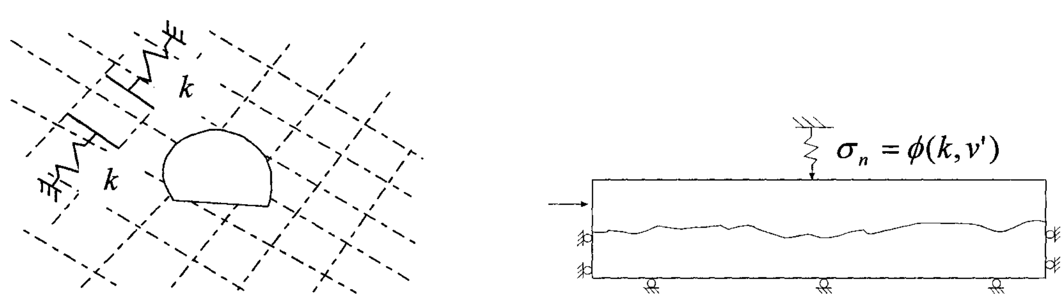

(a). Underground excavation in jointed rock (b). Equivalent 2-D model

Figure 2.5 Joint behavior at the roof of an excavation [after Indraratna et al. (1999)]

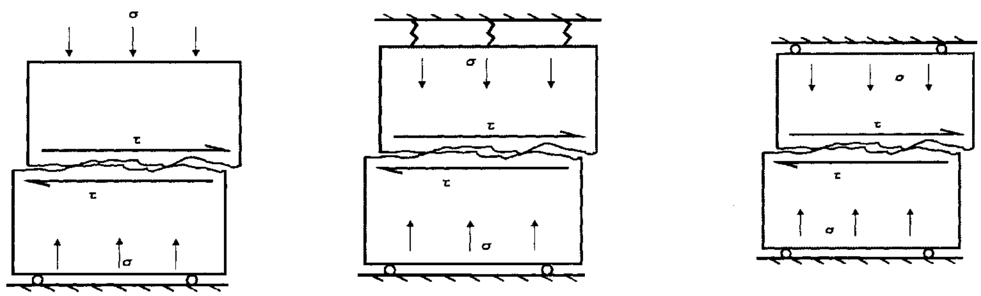

(a) Shear under constant normal stress (b) Shear under constant normal stiffness (c) Shear under constant normal displacement

Figure 2.6 Experimental study of shear under different normal boundary conditions.

2.4 Shear tests of joints under constant normal stress

Several investigators have examined the experimental behavior of rock joints during shear under constant normal stress states. Among these are Patton (1966), Barton (1973, 1976, 1986), Hoek (1977,1983, 1990), Bandis et al. (1981), Hencher and Richards (1989), Saeb and Amadei (1992), and Kulatilake et al. (1995).

Bandis and Barton (1983) gave their results for experiments conducted on five natural rock joints, both fresh and weathered, in slate, dolerite, limestone, silstone and sandstone. The results of shear test on the fresh dolerite joints are documented in detail since these results will be used in the numerical modelling exercises. The choice for dolerite is dictated by avability of supplemetary information concerning the failure properties of the material. Test specimens used were single-jointed rectangular blocks. Shear tests were conducted on a portable shear apparatus under constant normal stress. The shear loads were applied in an incremental fashion. Once the peak shear strength was reached, the shear load was released, the joint halves reassembled, and a new run performed under a higher normal stress. In such arrangement, since the normal stress levels applied are relatively low compared to the compressive strength, the contribution of asperity damage due to shear behavior on one identical profile has been minimized. We document here the results for dolerite joints, which are classified as being both fresh and weathered. Weathering effects in the dolerite were visible along the joint planes, which were covered by a layer of limonite (hydrated ferric oxide). The joint profiles for two cases are shown in Figure 2.8. The results for the variation of shear stress with shear displacement are also shown in Figure 2.8. The shear behavior of weathered joints is distinctly different from the results for the fresh joint. The material parameters relevant to the computational modelling are the tensile and compressive strength and the elastic constants. These correspond to

$$f_t = \text{tensile strength} = 17.3\,\text{MPa}$$
$$f_c = \text{uniaxial compressive strength} = 165.0\,\text{MPa}$$
$$E = \text{Young's modulus} = 78.0\,\text{GPa}$$

The Possion's ratio was not given in experitments. Uniaxial compression tests were performed on a single cylindrical and prismatic specimens. Axial strain was recorded by means of electrical resistance strain gauges. The axial stress-strain relationship for fresh dolerite is illustrated in Figure 2.7. The Young's modulus was calculated from the slope of the tangent to the stress-strain curve at 50% of the maximum axial compressive stress.

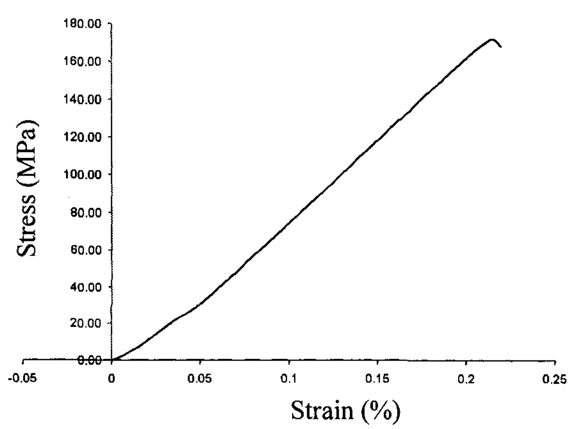

Figure 2.7 Uniaxial stress-strain relation for fresh dolerite (after Bandis et al. (1983)]

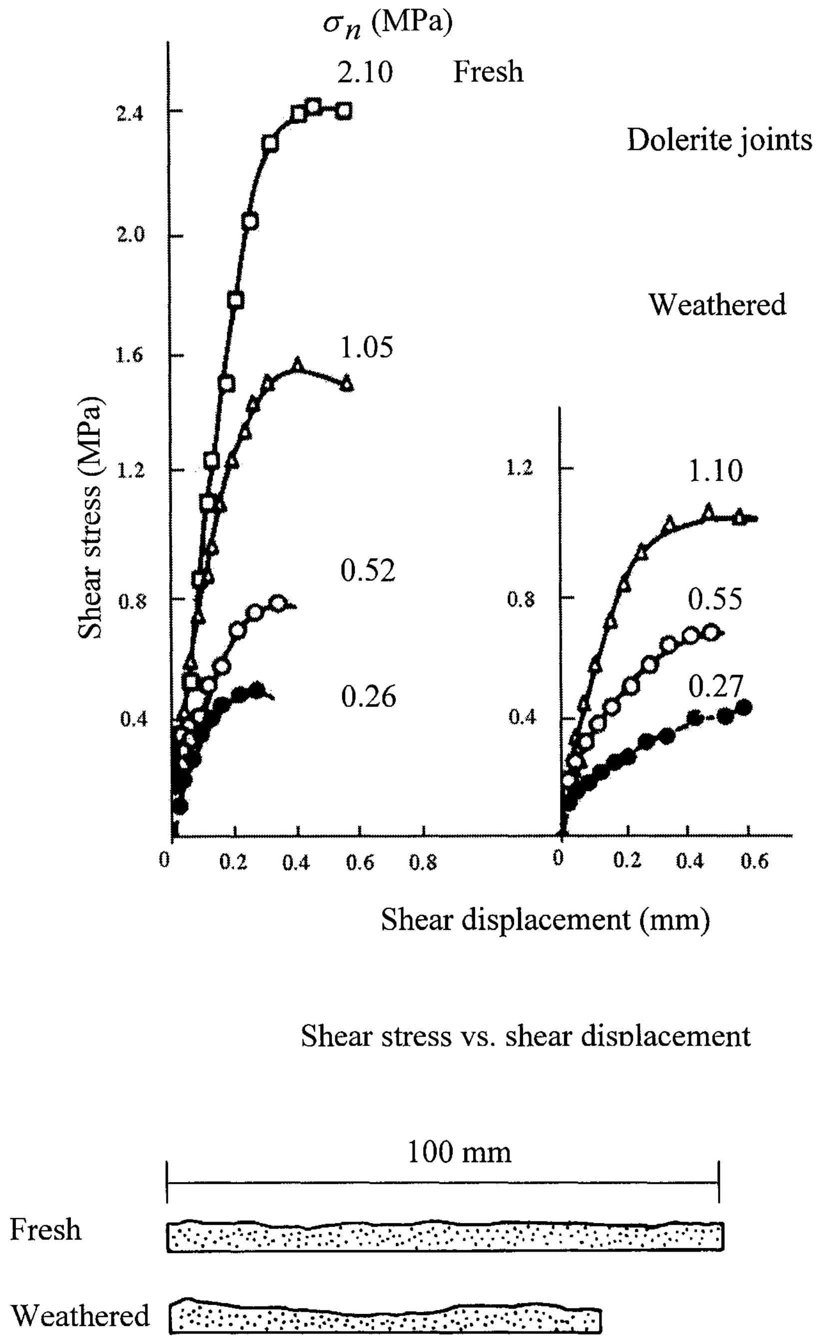

Joint profile

Figure 2.8 Shear behavior of fresh and weathered dolerite joint and corresponding joint profile [after Bandis et al. (1983)] ($f_c = 165.0$ MPa; $f_t = 17.3$ MPa; $E = 78.0$ GPa)

Sabbadini el al. (1995) measured the 3D morphology of a joint using a digitizing 3D-videolaser processing. Joint surfaces of schist and granite were first replicated with a silicon polymer resin model. The resin replicas were then used for moulds cast in mortar composed of fine sand, cement, silica fume and water. No strength variables for material are recorded. The surface morphology of the two joints and corresponding shear behavior are shown in Figure 2.9. Although the value of the fractal analysis indicated that granite replica surface was rougher in a 3D sense, the shear stress for the schist replica was slightly larger than that for granite replica under the same normal stress and at the same displacement in shear direction specified.

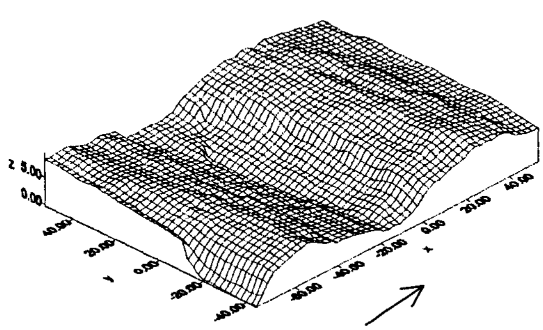

(a). Morphology of a schist joint replica

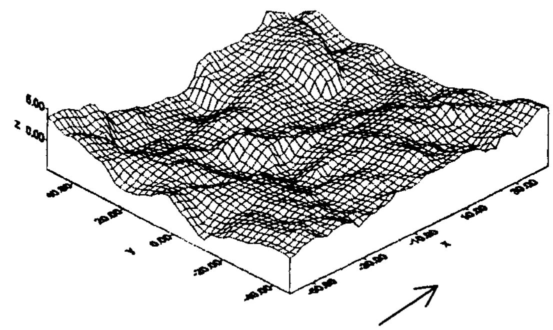

(b). Morphology of a granite joint replica

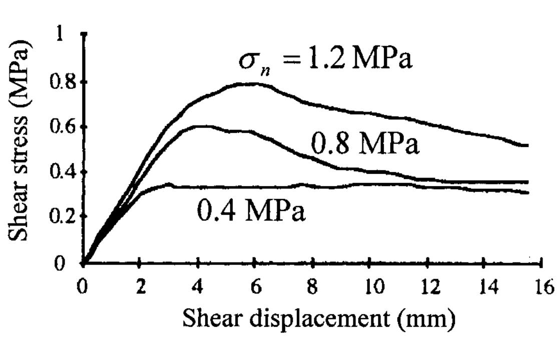

(c). Shear behavior of the schist replica

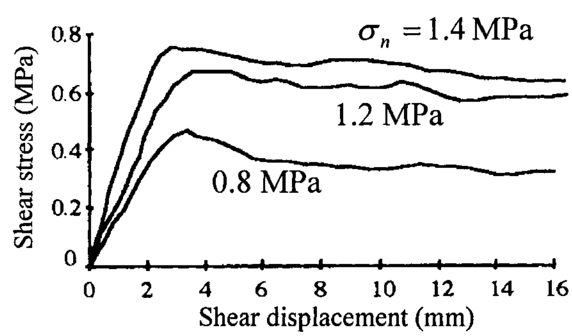

(d). Shear behavior of the granite replica

Figure 2.9 3D joint profile and related shear behavior under constant normal stress [after Sabbadini et al. (1995)]

2.5 Shear tests of joints under constant normal stiffness

At present, the published literature on tests involving constant normal stiffness is relatively limited compared to those under constant normal stress. The earliest work is due to Byerlee and Brace (1968) who considered the effects of mass stiffness on fault shearing. More recently, Leichnitz (1985), Indraratna et al. (1998, 2000), Benmokrane and Ballivy (1989), Van Sint Jan (1990), Ohnishi and Dharmaratne (1990), Benjelloun et al. (1990) have presented experimental results for tests on geomaterial joints conducted under constant normal stiffness.

Skinas et al. (1990) also documented the experimental results for tests conducted under constant normal stiffness. The tests were conducted on $15\,\text{cm} \times 10\,\text{cm}$ model joints, which were cast from natural joint surfaces, using a brittle, artificial material, which was prepared from a sand-barytes-cement mixture. A typical set of results is presented in Figure 2.10. Under constant normal stress $k = 0$, joint behaved in a relative brittle manner with a peak shear stress at $1.3\,\text{MPa}$. Under increasing value of k, shear behavior gradually transformed into plastic response. An increase in the normal stiffness leads to an increase in the normal stress and a reduction in the dilatancy.

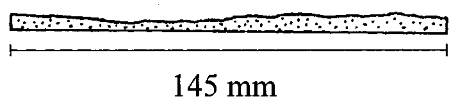

(a). 2D joint profile

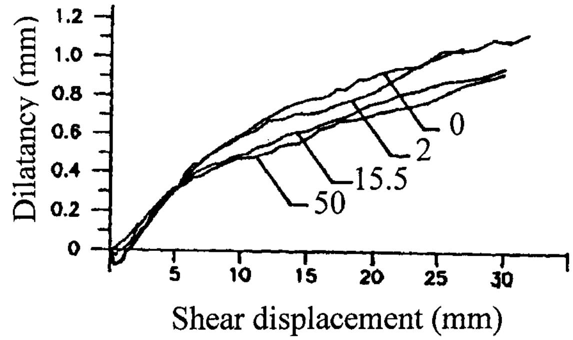

(b). Dilatancy vs. shear displacement

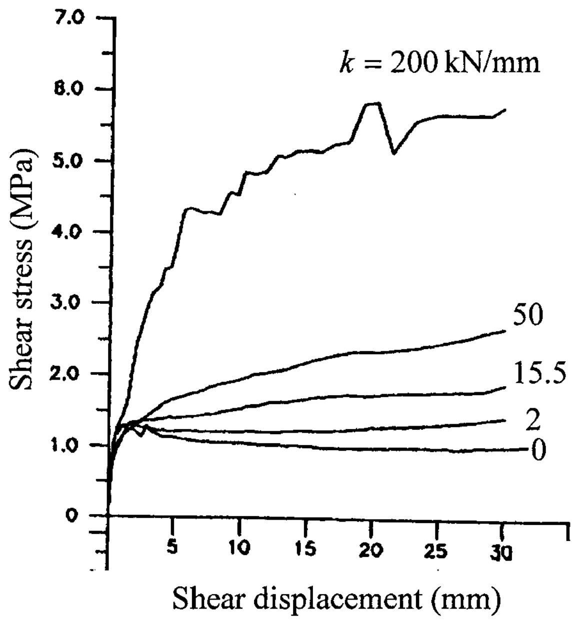

(c). Shear stress vs. shear displacement

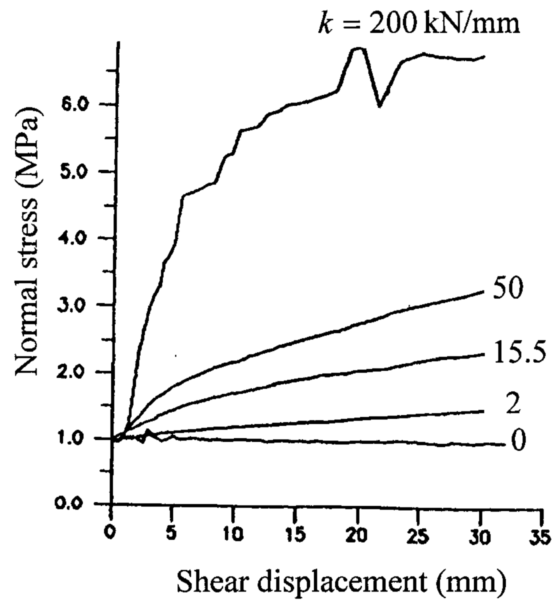

(d). Normal stress vs. shear displacement

Figure 2.10 Shear tests on identical joint surfaces under constant normal stiffness [after Skinas et al. (1990)]

[f_c ~ (25.0 - 30.0) MPa; E ~ (3.0 - 3.5) GPa; ν ~ (0.22 - 0.25)]

Van Sint Jan (1990) presented experimental data on the shear of a random joint tested under constant normal stiffness of 0 and $0.039\,\text{MPa/mm}$. Plaster of Paris is used as the model material. The model material is weak in a sense that it has a small compressive strength $f_c = 0.92\,\text{MPa}$. Joint profile is shown in Figure 2.11(a) and corresponding shear behavior is presented in Figure 2.11(b) to Figure 2.11(d). Due to the low value of f_c and low initial applied normal stress, the shear stresses in such cases are also low.

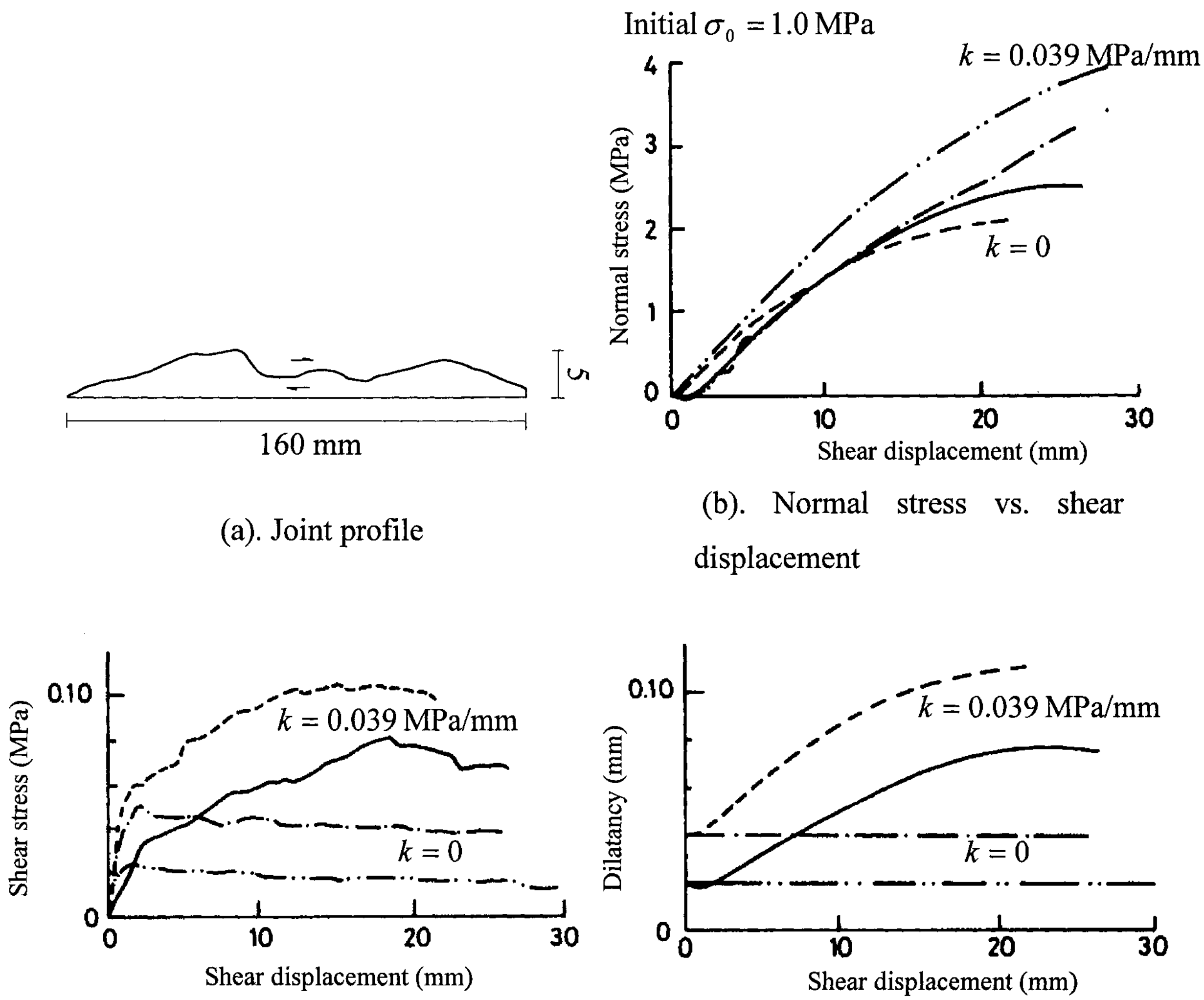

(a). Joint profile

(b). Normal stress vs. shear displacement

(c). Shear stress vs. shear displacement

(d). Dilatancy vs. shear displacement

Figure 2.11 Shear behavior under constant normal stiffness $k = 0.039\,\text{MPa/mm}$ [after Van Sint Jan (1990)] ($f_c = 0.92\,\text{MPa}; E = 1.06\,\text{GPa}$)

Thomas and Johnston (1987) and Kodikara and Johnston (1994) conducted shear tests under constant normal stiffness in order to examine the behavior of the rock socketed pile.

An artificial rock is made to simulate and examine both the regular and irregular rock (Mudstone)-concrete joints. The friction angle between rock and concrete was measured between 24° and 36°. Material properties are

$f_c = 2.8$ MPa; $E = 360$ MPa; $v = 0.3$.

An idealization of the test is shown in Figure 2.12,

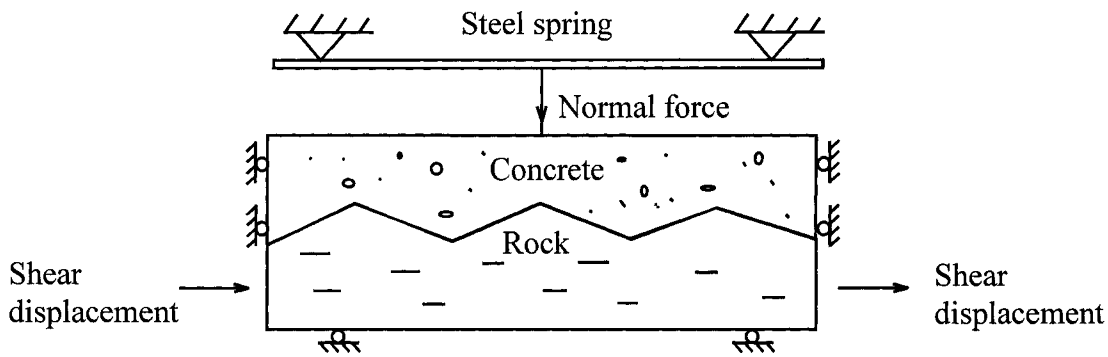

Figure 2.12 Configuration of test under constant normal stiffness [after Kodikara and Johnston (1994)]

Typical results for shear test results conducted on regular and irregular triangular concrete-rock joints are shown in Figure 2.13. It was reported that, the asperities of the regular joints all failed at the same values of shear displacement whereas for the irregular joints, the asperities failed at different values of shear displacement. The regular joints showed a relatively brittle response with a high shear resistance at the same shear displacement. The irregular aperities were more ductile with generally a lower peak resistance.

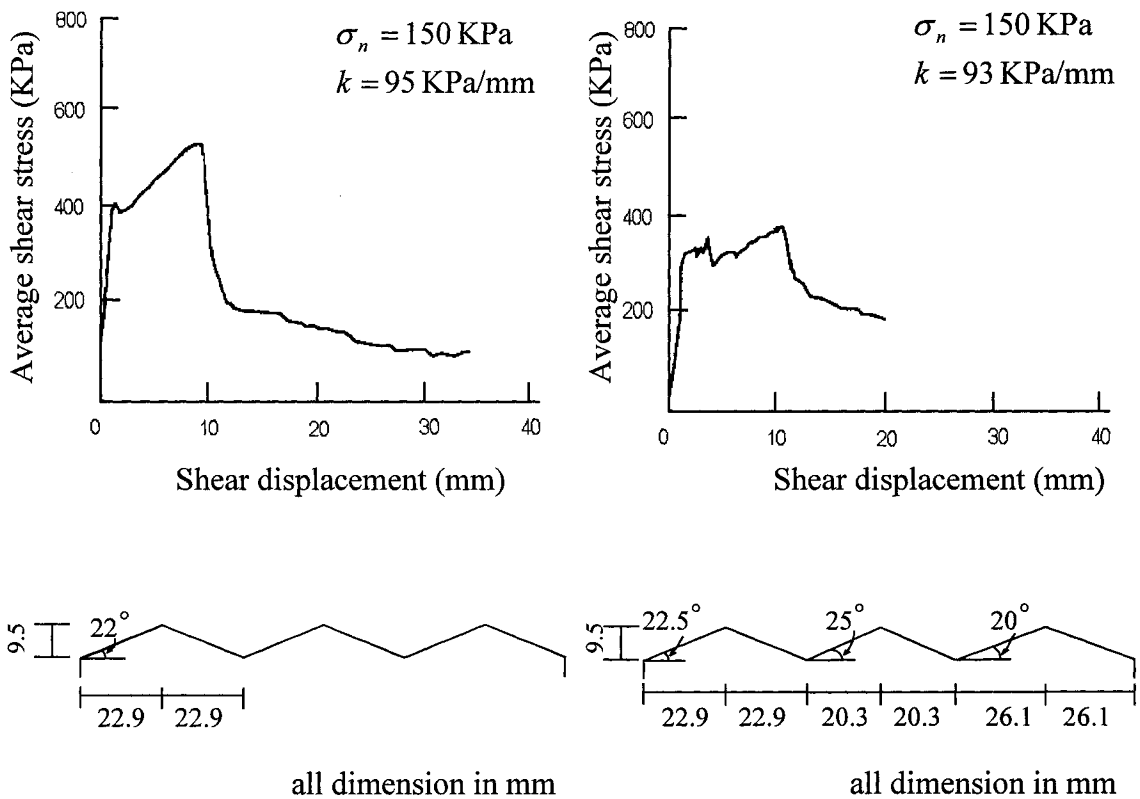

(a) Regular joint profile and its shear behavior

(b). Irregular joint profile and its shear behavior

Figure 2.13 Shear stress vs. shear displacement of regular and irregular joint under constant normal stiffness [after Kodikara and Johnston (1994)] ($f_c = 2.8$ MPa; $E = 360$ MPa; $\nu = 0.3$)

Seidel and Haberfield (1995) numerically generated the 2D-fractal joint profiles and performed experimental shear tests on joints with these profiles under constraints of constant normal stiffness. Model material used was the same as that used by Kodikara and Johnston (1994). Figure 2.14(a) shows three different levels of numerical approximation of random joint profiles based on the same algorithm. In this algorithm, an initial straight-line chord was bisected and mid-point was allowed to displace a random distance according to the Gaussian distribution of the asperity angle. The definition of asperity angle is given in Figure 2.3. The same process was applied to each of the two resulting chords. The roughness of resulting profile could be characterized by s_θ, which was the standard deviation of asperity angle. The coarser approximation was taken as a base from which finer approximation was generated. Graphical comparison between values of s_θ and *JRC* are given in Figure 2.3. A finer approximation of fractal profile led to higher roughness parameter s_θ. It appears that higher values of shear stress could be obtained during shear for the finer approximation although the indicated variation of shear stress in different cases was considered to be within the bounds of experimental error.

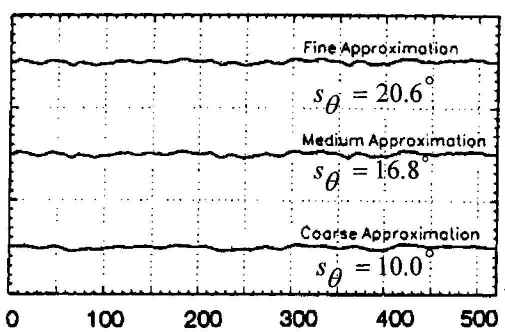

(a). Numerically generated fractal profile

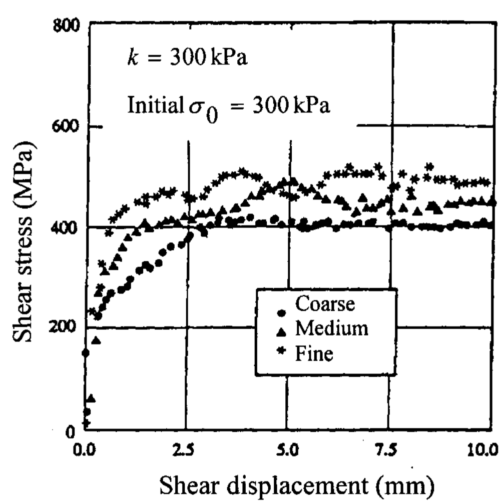

(b). Shear behavior of fractal profiles under constant normal stiffness

Figure 2.14 Test results for numerically generated fractal profile [after Seidel and Haberfield (1995)]

Recently, Indraratna et al. (2000) presented results for tests conducted on natural (field) joints under constant normal stiffness. The natural sandstone joints were sampled from a rockslide site at Kangaroo Valley in New South Wales, Australia. Petrological studies showed that it was a poorly sorted medium to coarse-grained sandstone having 68-70% quartz (Geological Survey of New South Wales, 1974). The field joints were cut at the site in the form of a block and transported to the laboratory. The specimens [shown in Figure 2.15(c)] were finally cut into a size measuring $250\,\mathrm{mm} \times 75\,\mathrm{mm} \times 150\,\mathrm{mm}$ for top part and $250\,\mathrm{mm} \times 75\,\mathrm{mm} \times 100\,\mathrm{mm}$ for bottom part to fit the shear mould. The highly weathered sandstone had uniaxial compressive strengths of $19\,\mathrm{MPa}$ to $21\,\mathrm{MPa}$.

The initial normal stress was applied through a hydraulic jack. The normal stiffness was provided by a set of normal springs. The shear load was applied via a horizontally aligned hydraulic jack. The details of shear apparatus are shown in Figure 2.15(a).

All natural joints were tested under constant normal stiffness $k = 8.5\,\mathrm{kN/mm}$. The results for the variation of shear stress with shear displacement are presented in Figure 2.15(c). Generally, a higher normal stress led to a higher shear stress at the same values of shear displacement. Since the tests were performed on different natural joints with different profiles, it was not necessary to reduce the shear stiffness as the initial normal stress was increased.

Dilatancy was monitored at the center of the top of the specimen. As can been from Figure 2.16(a), unconventional negative dilatancy was recorded with increasing initial normal stress. In such cases, the normal stress would decrease rather than increase with shear displacement. The negative dilatancy during shear could be attributed to the weathered condition, which improved the compressibility of the rock joint, but no clear explanations were provided.

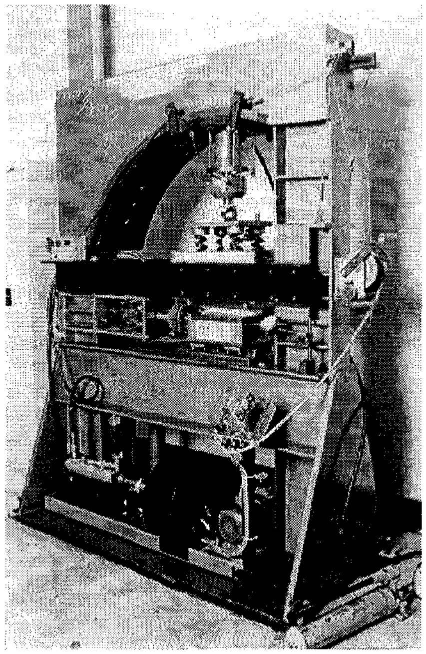

(a). Machine for shear under constant normal stiffness

(b). Close view of one natural (field) joint prepared for testing

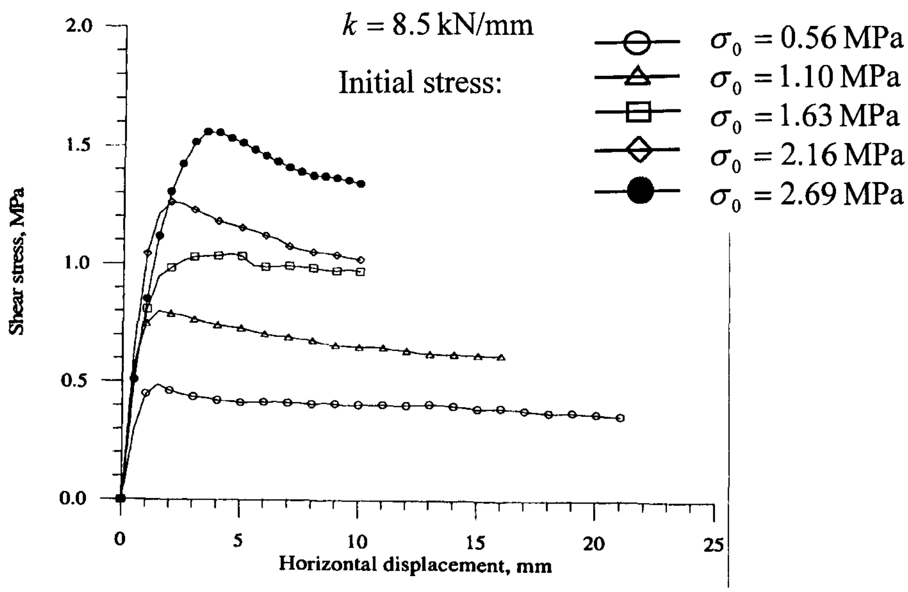

(c). Shear stress vs. shear displacement

Figure 2.15 Test machine, rock specimen and variation of shear stress during shear conducted on natural rock under constant normal stiffness [after Indraratna et al. (2000)]

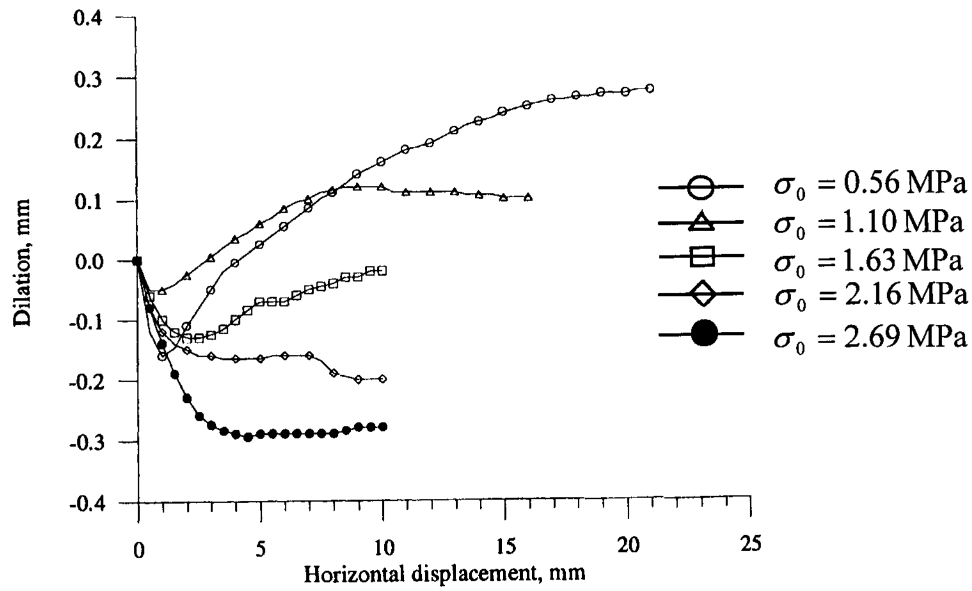

(a). Dilatancy vs. shear displacement

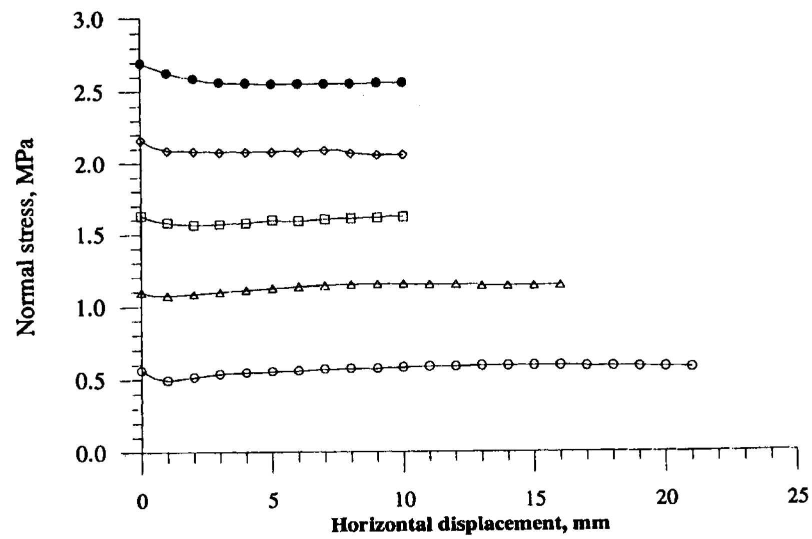

(b). Normal stress vs. shear displacement

Figure 2.16 Variation of dilatancy and normal stress during shear conducted on natural rock joint under constant normal stiffness [after Indraratna et al. (2000)]

2.6 Scale effect on shear behavior

Differences in the shear behavior of a joint at different scales are noticeable in results obtained in many experimental programs. Several authors, such as Barton and Choubey (1977), Bandis et al. (1981), Swan and Zongqi (1985), Yoshinaka et al. (1991), Ohnishi and Yoshinaka (1992) have extensively investigated scale effect on shear behavior of rock joints. The factors that contribute to the scale effects are still not well understood.

Bandis and Barton (1981) points out the overall scale effects on joint behavior under constant normal stress. Model materials were used and joint replicas had the same joint profile as those of the prototype natural rock. Larger model joints were broadly divided into smaller ones to account for the scale effects (Figure 2.17). It is observed that, increasing block size or length of joint leads to:

(i) a gradual increase in peak shear displacement;
(ii) an apparent transition from a "brittle" to "plastic" mode of shear behavior;
(iii) insignificant scale effects in the case of relatively planar and smooth joint types.

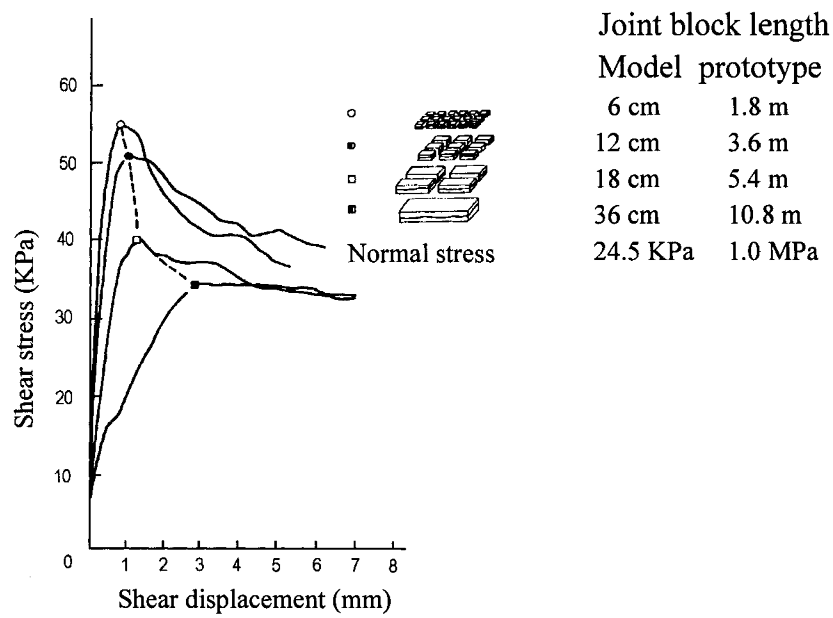

Figure 2.17 Scale effect on the relationship of shear stress vs. shear displacement [after Bandis and Barton (1981)]

Ohnishi and Yoshinaka (1992) performed experiments on regular and irregular joints at different sizes under constant normal stress to examine the factors influencing scale effect on shear behavior in joints. In their opinion, scale effect was strongly related to the regularity and irregularity of the surface shape. Their test results did not show any scale effect on the shear strength of regular or smooth joint surface. They made one conceptual understanding of the scale effect; i.e., joints with different number of repeated pattern of size B mm (Figure 2.18) were expected to have a same shear behavior; the scale effect would, however, appear if the specimen of size B mm was divided into smaller pieces and tested.

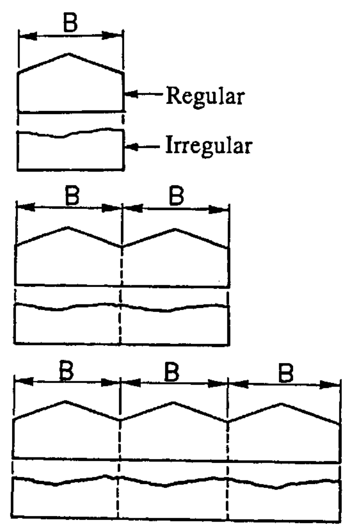

Figure 2.18 Repeated joint pattern, which is expected to have no scale effect on shear behavior [after Ohnishi and Yoshinaka (1992)].

2.7 Cyclic shear behavior of rock joints

Asperties are damaged during shearing. These asperities can further be crushed between contacted surfaces and become gouge materials residing in the valley of the asperities, which decrease the dilatancy angle and would likely decrease the permeability of the joint. Mechanical asperity degradation becomes obvious during cyclic shear tests under different constraints normal to the joint.

Huang (1993) presents some experimental results of cyclic shear behavior conducted on some regular joints of artificial plaster material under constant normal stress. The compressive strength f_c of the material is 38 MPa.

Figure 2.19 illustrates relative displacement between joint surfaces during one complete cycle of shear. Corresponding curves for shear and dilatancy are shown in Figure 2.20(a) and 2.20(b). Shear displacement is first increased in "forward" direction from the original position *a* to maximum displacement *b* and decreased again to the original position *c* again. The dilatancy exhibited maximum value at *b*. Then shear displacement is applied in "reverse" direction from original position *c* to maximum displacement *d* and decreased to original position *e*. The maximum displacements in "forward" and "reverse" directions have the same values. During shear in the "forward" direction, dilatancy observed is greater in unloading process from *b* to *c* than that in loading process from *a* to *b*. Similar phenomenon is found during shear in the "reverse" direction, where dilatancy is also larger in unloading process from *d* to *e* than in the loading process from *c* to *d*.

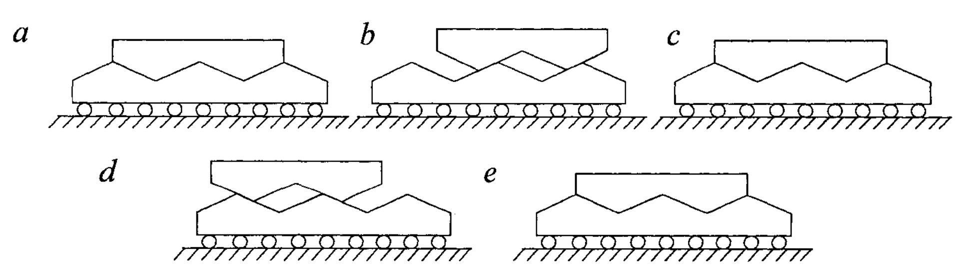

Figure 2.19 Schematic illustration of one complete cycle of shear [after Huang (1993)]

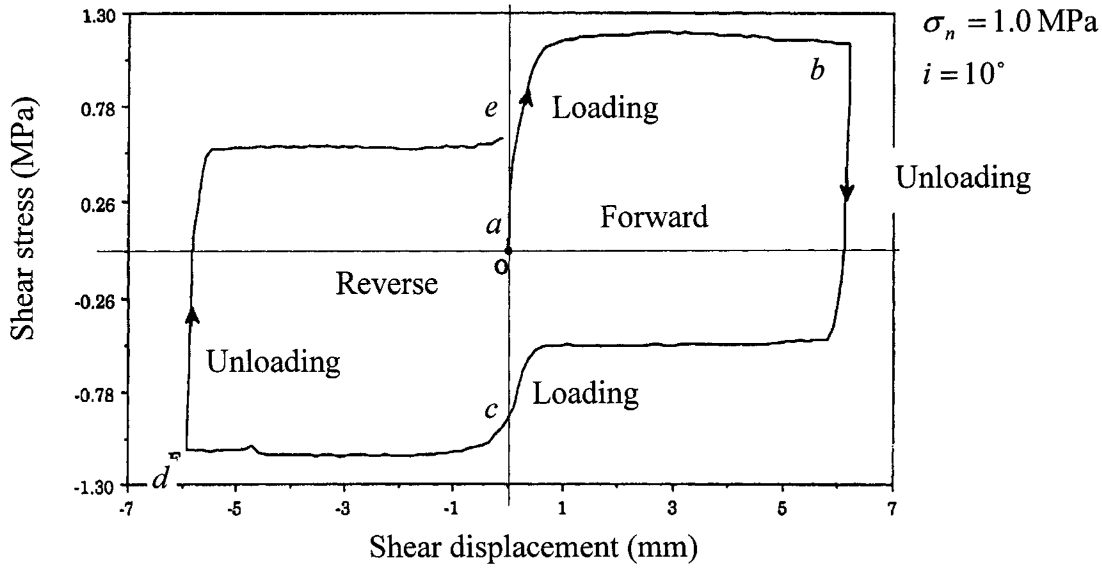

(a). Shear stress vs. shear displacement

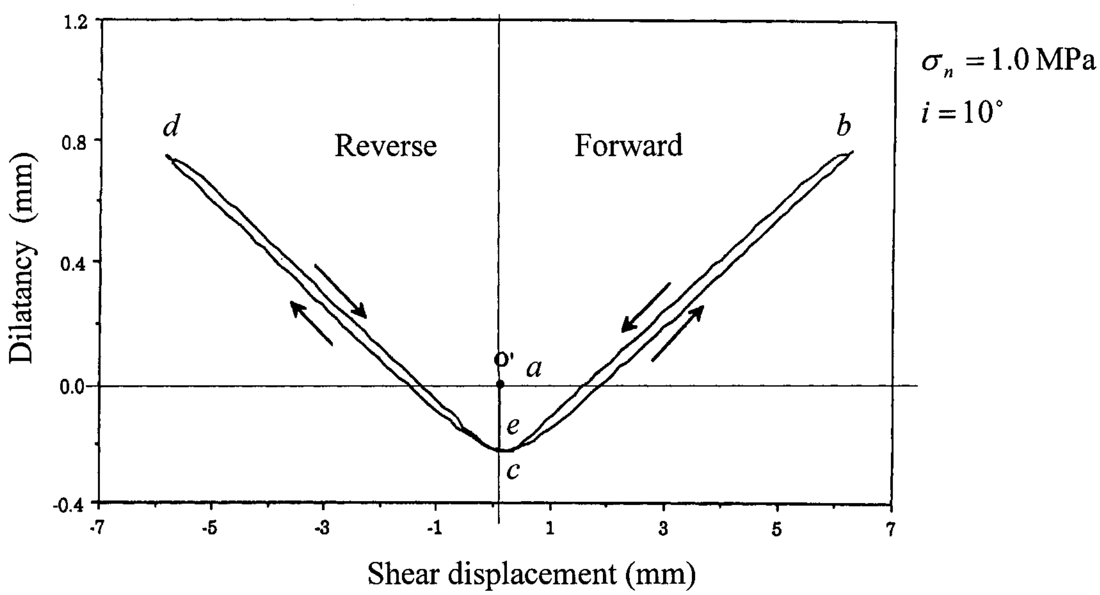

(b). Dilatancy vs. shear displacement

Figure 2.20 A single cycle of shear behavior under constant normal stress [after Huang (1993)]

Wibowo et al. (1992) conducted a series of 5-cycle tests under constant normal stress and constant normal stiffness. A fracture at size $15.24\,\text{cm} \times 7.62\,\text{cm} \times 7.62\,\text{cm}$ was created by tensile splitting. Gypsum cement with a compressive strength of $27.58\,\text{MPa}$ was used as the model material to duplicate the joint profile. A constant normal load of $13.12\,\text{kN}$ ($\sigma_n = 2.26\,\text{MPa}$) was applied during the test under conditions of constant normal stress. In another test, the stiffness $k = 25.86\,\text{kN/mm}$ was added for shear under constant normal stiffness. Comparison of shear behavior under two different constraints normal to the plane of shear is shown in Figure 2.21.

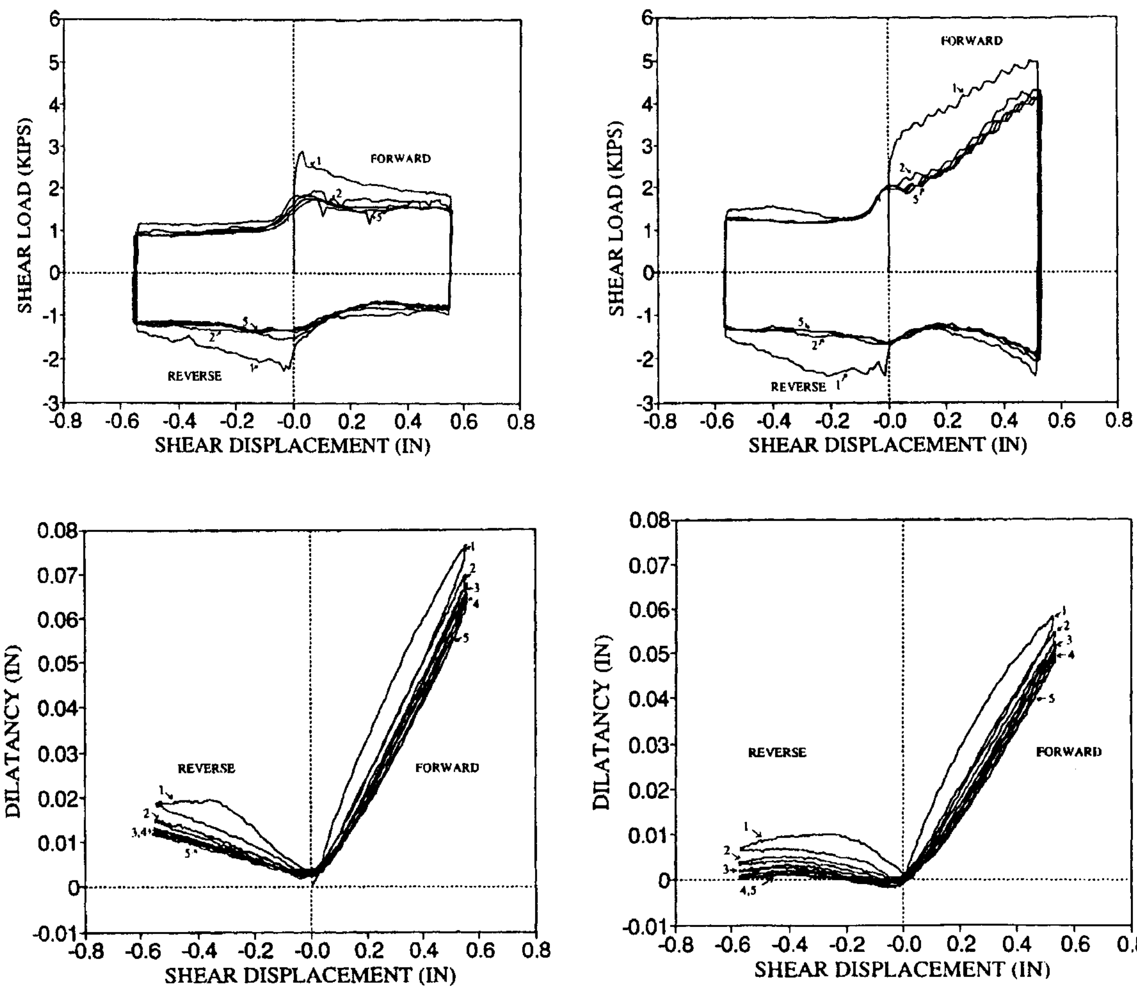

(a). Shear under constant normal stress (b). Shear under constant normal stiffness

Figure 2.21 Shear under two different boundary conditions up to 5 cycles [after Wibowo et al. (1992)]

Asperity degradation during multi-cycles of shear had an obvious effect on shear behavior. Due to the damage of asperities, dilatancy and dilatancy angle all reduced with the increase in the number of cycles, for both constant normal stress and constant normal stiffness type tests. Shear loading damaged some relatively sharp asperities and decreased the asperity angle, which subsequently reduced the dilatancy value and shear stress. Asymmetry of shear behavior was found for shear of am irregular joint under two different loading directions. Dilatancy and shear stress showed different values in the "forward" and "reverse" directions.

The normal stiffness caused a greater suppression of dilatancy and higher shear stresses. The contribution from normal stiffness to shear behavior was related to dilatancy. In reverse shear, dilatancy was generally small and the shear behavior under constant normal stiffness was very close to that obtained under constant normal stress, especially in later cycles where dilatancy was nearly zero.

2.8 Shear induced changes in hydraulic conductivity of fractures

The normal and shear action on a joint might close or open the joint aperture due to contraction or dilatancy. Consequently, the hydraulic properties vary due to the changes in the aperture. Recent results of experimental investigations in this area are given by Makurat et al. (1990), Olsson and Brown (1993), Esaki et al. (1996,1999), and Yeo (1998).

Makurat et al. (1990) presented the experimental results of variation of hydraulic conductivity with shear displacement conducted on natural joints in igneous rocks. A biaxial cell is used for test shown in Figure 2.22(a). With this equipment, joints could be closed, sheared and dilated under controlled normal stress condition, and at the same time, fluid could be flushed through the joint. Deformation, flow rate and stresses could be recorded simultaneously.

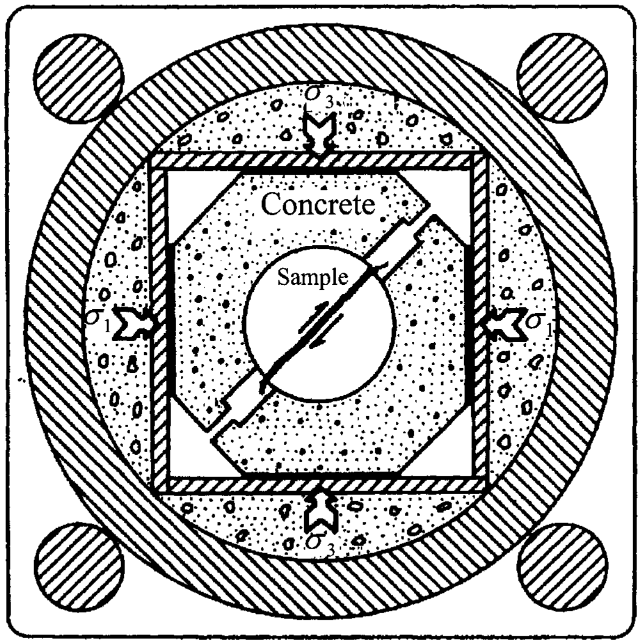

(a). Biaxial cell for testing on natural joints

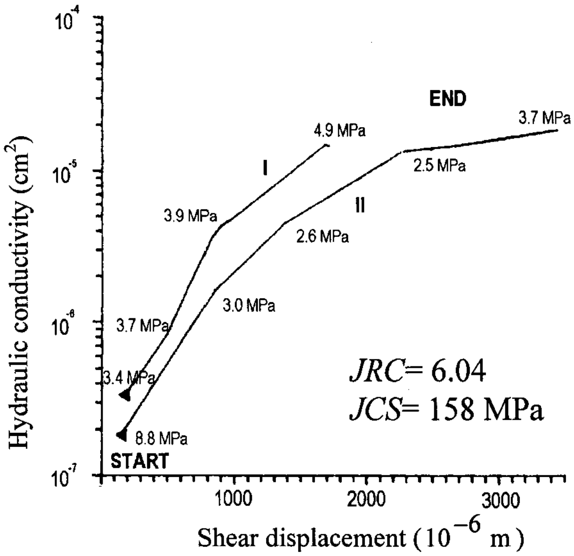

(b). Joint conductivity for shear under low normal pressure (compared to $f_c = 221\,\text{MPa}$)

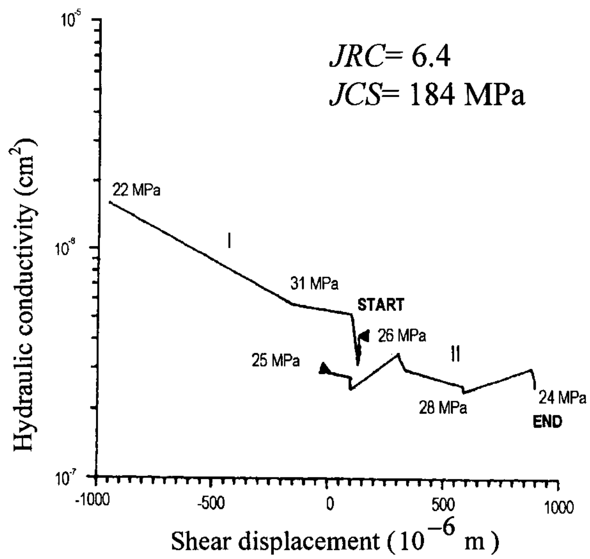

(c). Joint conductivity for shear under high normal pressure (compared to $f_c = 210\,\text{MPa}$)

Figure 2.22 Hydraulic conductivity of joints obtained by biaxial cell testing [after Makurat et al. (1990)]

Figure 2.22(b) presents the change of hydraulic conductivity of joint with shear displacement for one joint under low normal stresses (compared to f_c). The hydraulic conductivity increased by nearly two orders of magnitude after 3.5 mm of shear. This was due to the low restraint to dilatancy. Figure 2.22(c) presents the hydraulic conductivity change during a test conducted on another joint with similar *JCS* and *JRC* properties, but under much higher normal stress. Hydraulic conductivity increased corresponding to shear tests in direction I, whereas it exhibited no major change in reverse shear in direction II.

Esaki et al. (1999) measured hydraulic conductivity during shear of granite joints with an artificial created profile. The test apparatus had the following characteristics: (a) an artificial stationary joint could be created from an intact rock specimen; (b) large shear displacement could be applied beyond residual stresses; (c) constant normal loads could be applied and (d) hydraulic tests could be conducted by supplying a constant water head to the joint during normal and shear process.

The rocks used were hard granites with porosity at 0.37% and uniaxial compressive strength of $162\,\mathrm{MPa}$. The size of specimens was $120\,\mathrm{mm}$ in length, $100\,\mathrm{mm}$ in width and $80\,\mathrm{mm}$ in height. The artificial fracture was then created at the mid-height of the specimen using a pair of horizontal jacks, which applied loads perpendicular to the direction of shear. Based on the water flow measured, the hydraulic conductivity was estimated by using an approximating equation assuming the cubic law applicable to the parallel plate. The tests revealed that the trend of change of hydraulic conductivity was approximately similar to that of the dilatancy of a joint. For the first $5\,\mathrm{mms}$ of shear displacement, the hydraulic conductivity increased rapidly by about 1.2 to 1.6 orders of magnitude. After reaching the residual stress level, the hydraulic conductivity became almost constant. Reverse shear was also applied and dilatancy was lower than that in forward shear. However, when shearing in reverse direction is close to the initial zero point, the value of normal displacement is greater than that prior to shear. This indicates the possible deposit of gouge materials in the valleys of joint surface. The theoretical prediction based on Barton (1985)'s empirical relation between hydraulic aperture and mechanical aperture E, that is, $e = E^2/JRC^{2.5}$, generally over-estimated the experimental results slightly.

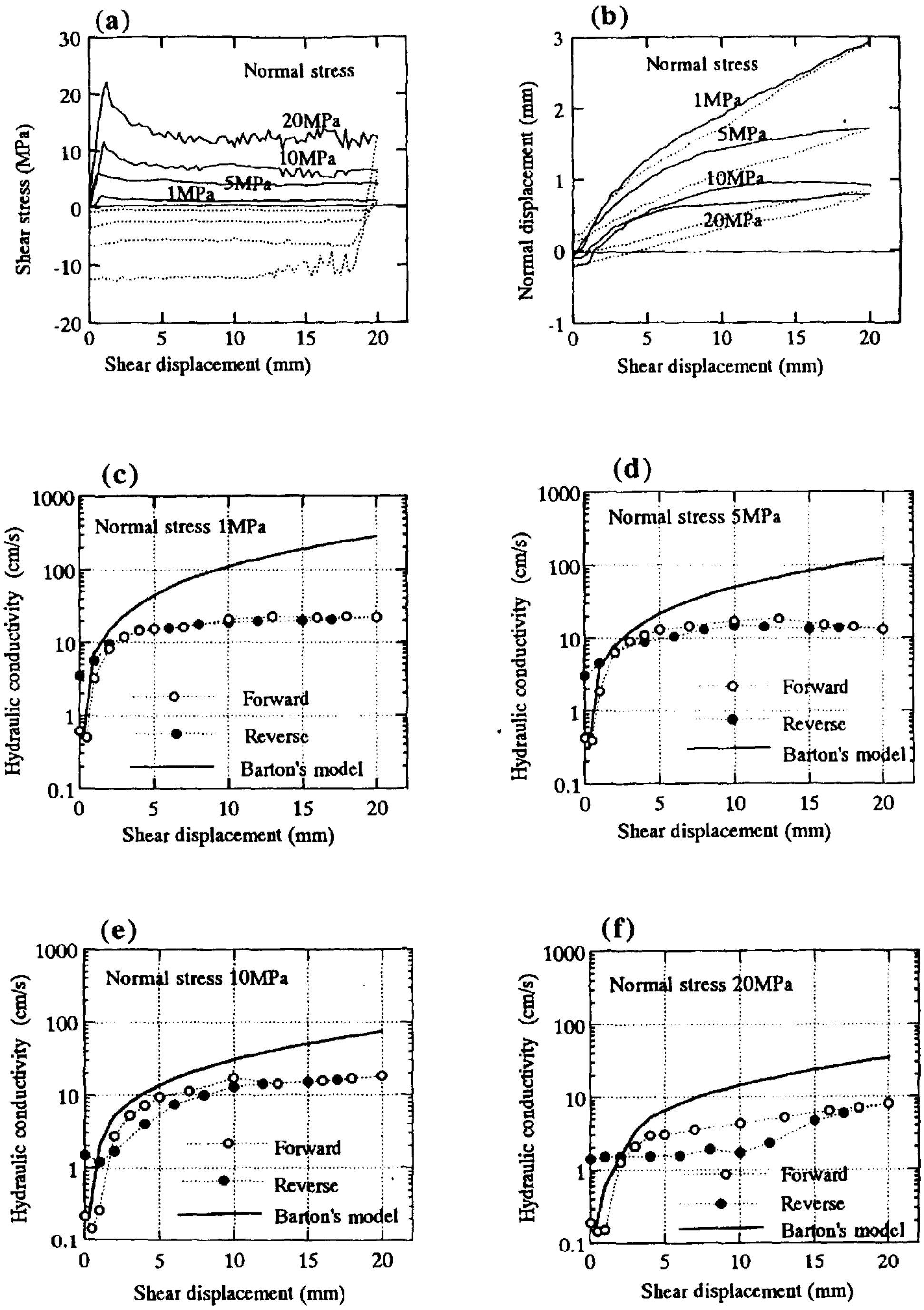

Figure 2.23 Shear infuced changes in hydraulic conductivity of joints [after Esaki et al. (1999)]

2.9 Summary

Although complex behavior of shear in joints is not completely understood, some general conclusions can be observed:

(i) The surface roughness has important influence on the shear behavior of rock joints. Traditional determination of *JRC* (Joint Roughness Coefficient) is prone to subjectivity and depends on the direction of shearing. Statistical and fractal methods give possible alternative methods with no direction and scale-dependency in the information.

(ii) Normal stiffness causes a greater suppression of dilatancy. Shear behavior conducted under constant normal stiffness exhibits a greater ductile behavior and higher shear stress at the same displacement, than those obtained under constant normal stress.

(iii) The asperities deform and possibly fail during shear. Asperity damage influences dilatancy and shear stresses during cyclic shear. Asperity degradation becomes evident during multi-cycle shear, which decreases the dilatancy angle with increase in the number of cycles.

(iv) Differences in the shear behavior at different scale of the joint are noticeable. The factors that contribute to scale effects are still not well known. Joints with repeated profile pattern will not, in general, exhibit differences in shear behavior at different scales.

(v) Hydraulic conductivity of a joint can change by 1 to 2 orders of magnitude during shear. The variation of hydraulic conductivity follows closely the variation of dilatancy during shear.

Chapter 3

CONSTITUTIVE CRITERIA FOR BRITTLE GEOMATERIALS AND MODELLING OF CONTACT INTERACTION

Geomaterials such as rocks and concrete exhibit brittle behavior at values of confining stress significantly lower than their tensile and compressive strengths. Although this behavior is well recognized, the failure of such materials is usually characterized in relation to theory of plasticity, which is normally applicable to materials with predominantly ductile behavior. Investigations relating to the failure of rocks and concrete are quite extensive and comprehensive accounts of research in this area are given by Coates (1967), Goodman (1976, 1989), Assonyi (1979), Jaeger and Cook (1976), Jumikis (1983), Charlez (1991), Brady and Brown (1993). The theoretical formulation of the plastic failure of a geomaterial requires the specification of three criteria: namely a failure criterion, a hardening rule and a flow rule. We shall briefly discuss those three aspects with special reference to the application of the theories of materials such as rocks and concrete. This chapter also contains a brief summary of the various failure criteria in the literature that have been developed for describing the failure characteristic of brittle geomaterials. For simplifity, perfect plasticity is assumed.

3.1 Failure criterion of brittle geomaterials

The failure characteristics of brittle geomaterials such as rock depends on a variety of factors including the types of forming minerals, the fabric of rocks, the distribution of grain size and the degree of weathering. Igneous rocks generally consist of a crystalline assemblage of minerals such as quartz, plagioclase, pyroxene, mica, etc (Jaeger and Cook, 1976). Sedimentary rocks consist of an assemblage of detrital particles and possibly pebbles from other rocks in a matrix of materials such as clay minerals, calcite, quartz, etc. Metamorphic rocks are produced by the action of heat, stress, or heated fluid on other rocks, sedimentary or igneous. All these minerals have anisotropic properties. Most rocks consist of an aggregate of crystals and amorphous particles jointed by varying amounts of cementitious materials. The boundaries between crystals represent weakness in the structure of the rock. The size of the crystals may be uniform or variable. The dimension of grain size of coarse granite can sometimes reach up to several centimetres (Wahlstrom, 1994). Figure 3.1 shows a close view of section of alkali dolerite. On a scale with dimensions ranging from decimeters to meters, the rock mass contains sufficient number of crystals and it can be regarded as continuous. If the interactions between grain boundaries are sufficiently random, the average properties can be regarded as homogeneous and isotropic. However, the failure of such a multiphase geomaterial can be more complex and influenced by the existence of cracks at variable scales, either within the phases or at the phase interfaces, resulting in a variability in the strength. The most noticeable feature of failure of such a brittle geomaterial is that the strength in uniaxial tension is significantly different from the strength in uniaxial compression (Goodman, 1976; Chen, 1981). Although in both modes, the strength is governed by microcrack development within the various phases and inter-phases, the closure of cracks and frictional effects at the faces of such cracks lead to the development of plasticity type phenomena. When the disturbance from appearance of cracks are small in relation to the dimensions of a structure in rock, the rock mass can be treated as a continuum. Figure 3.2 shows results of typical stress-strain data obtained through compression testing of some brittle rocks. The tensile response of geomaterials exhibits similar behaviour. The mechanical behavior of concrete follows a similar pattern. A typical example is shown in Figure 3.3. Typical features of the uniaxial stress-strain curve for a brittle geomaterial are summarised in Figure 3.4. This figure also presents suitable idealization within the content of elasto-plastic behavior.

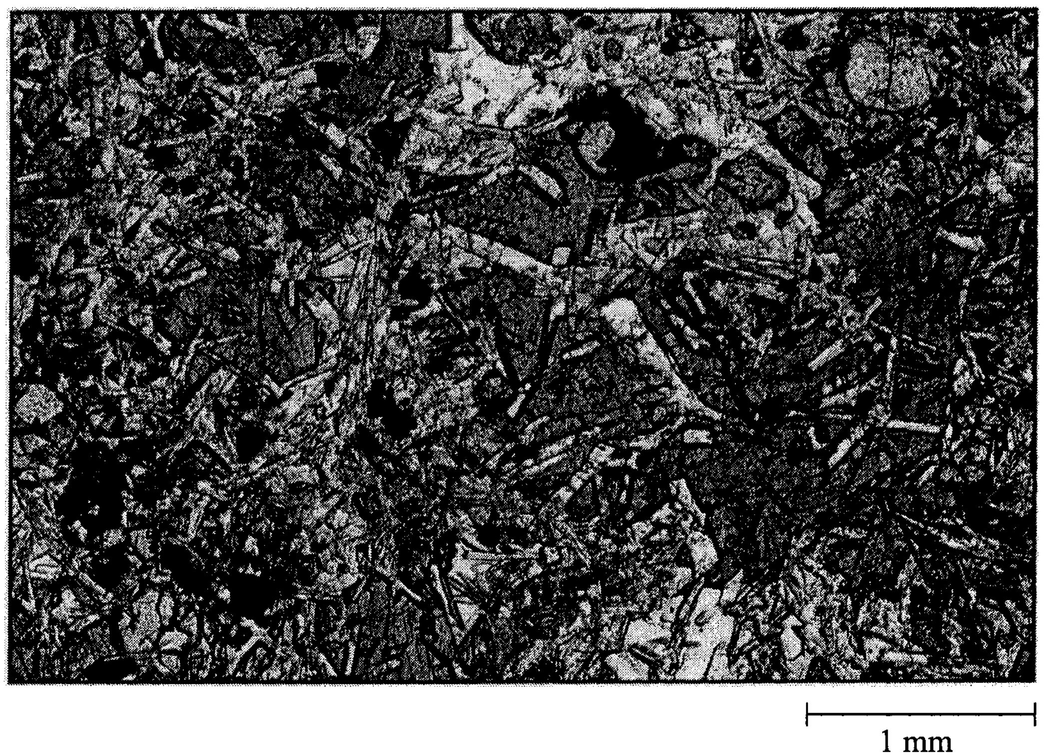

Figure 3.1 Ophitic texture of alkali dolerite: the larger clinopyroxene crystals enclosing lath-shaped crystals of plagioclase feldspar [after MacKenzie and Adams (1994)].

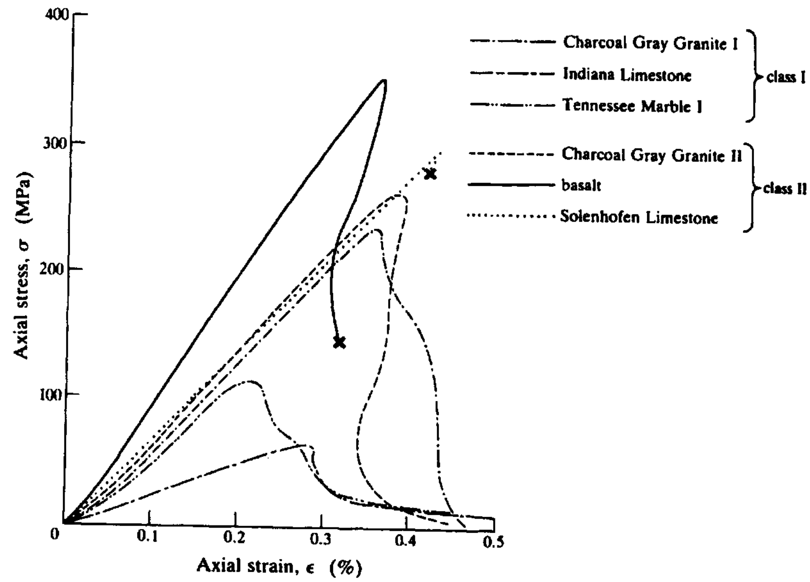

Figure 3.2 Uniaxial stress-strain curves for six rock types [after Wawersik and Fairhurst (1970)] (Class I: local tensile fracture predominantly parallel to the applied stress; Class II: local and macroscopic shear fracture)

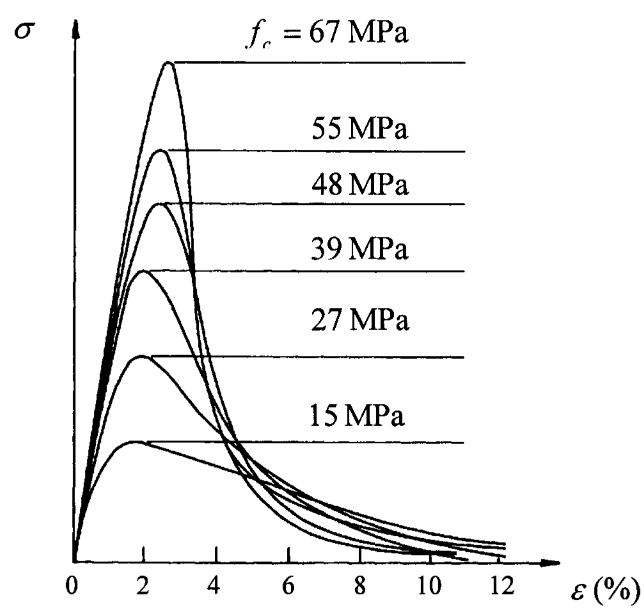

Figure 3.3 Uniaxial compressive stress-strain curves for concrete [after Wischers (1978)]

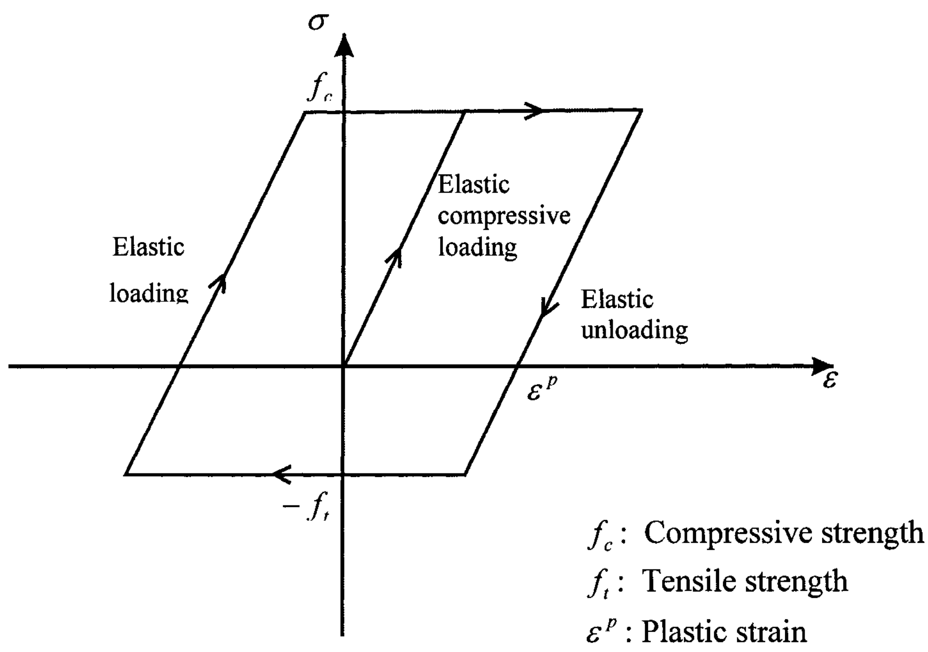

Figure 3.4 Elasto-plastic response of geomaterials with perfect plastic idealization

3.2 Multiaxial failure criteria for brittle geomaterials

The description of the failure behavior of brittle geomaterials due to a three-dimensional stress state is an essential requirement for the formulation of a theory of plasticity for brittle geomaterials. In general, the failure criterion for a material can be represented in the form

$$f(\sigma_{ij}) = k' \tag{3.1}$$

where k' is a material parameter which can depend on the post-failure hardening characteristics of the geomaterials. In (3.1),

$$\sigma_{ij} = \begin{bmatrix} \sigma_{xx} & \sigma_{xy} & \sigma_{xz} \\ \sigma_{yx} & \sigma_{yy} & \sigma_{yz} \\ \sigma_{zx} & \sigma_{zy} & \sigma_{zz} \end{bmatrix} = \sigma_{ji}, \tag{3.2}$$

is the Cauchy stress tensor referred to the Cartesian coordinate system. For isotropic geomaterials, the failure criterion can also be represented in terms of the principal invariants I_n in the form

$$f(I_1, I_2, I_3) = \tilde{k} \tag{3.3}$$

where

$$\begin{aligned} I_1 &= tr(\sigma_{ij}) \\ I_2 &= \tfrac{1}{2}[tr^2(\sigma_{ij}) - tr(\sigma_{ij}{}^2)] \\ I_3 &= \det(\sigma_{ij}) \end{aligned} \tag{3.4}$$

and tr denotes the trace of the matrix. In some instance, it is also convenient to represent (3.1) in the form

$$f(I_1, J_1, J_3) = k^* \tag{3.5}$$

where J_2 and J_3 are the second and third principal invariants of the stress deviator tensor s_{ij} defined by

$$s_{ij} = \sigma_{ij} - \tfrac{1}{3} I_1 \delta_{ij}. \tag{3.6}$$

Similarly, the strain deviator tensor can be also defined by

$$\zeta_{ij} = \varepsilon_{ij} - \tfrac{1}{3} tr(\varepsilon_{ij}) \delta_{ij}. \tag{3.7}$$

The functional form $f(I_1, I_2, I_3)$ or $f(I_1, J_1, J_3)$ now needs to be specified by considering results of experiments. A variety of failure criteria have been proposed in the literature and detailed descriptions of these are given by Prager and Hodge (1951), Westergaard (1952), Prager (1959), Thomas (1961), Kachanov (1971), Chen (1981, 1994), Doltsinis (2000). Detailed description of classical failure criteria such as Rankine (maximum stress), and Von-mises (Maximum distortional energy) criteria are also given in the references cited previously. While all of these criteria have same relevance to the description of brittle failure, more relevant criteria have been proposed in recent literature.

3.2.1 The Mohr-Coulomb failure criterion

The Mohr-Coulomb failure criterion is one of the earliest failure criteria that have been proposed for the description of failure of brittle geomaterials including soils, rocks and concrete. The basic hypothesis assumes that the failure of the geomaterial is governed by the normal and shear stress at the potential plane of failure

i.e.

$$\tau = c + \sigma \tan\phi \tag{3.8}$$

where τ is the shear stress on the failure plane, σ is the normal stress on the failure plane and c and ϕ are the strength parameters derived, respectively, from cohesion and angle of friction. In terms of the stress invariants, the above failure criterion can be represented in the form

$$\tfrac{1}{3} I_1 \sin\phi + \sqrt{J_2}\sin(\theta + \frac{\pi}{3}) + \frac{\sqrt{J_2}}{\sqrt{3}}\cos(\frac{\pi}{3} + \theta)\sin\phi - c\cos\phi = 0 \tag{3.9}$$

where

$$\theta = \cos^{-1}\{\frac{2\sigma_1 - \sigma_2 - \sigma_3}{2\sqrt{3}\sqrt{J_2}}\}\,;\ \theta \in (0\,, 60^\circ) \tag{3.10}$$

and σ_i are the principal stresses.

3.2.2 Drucker-Prager failure criterion and its modification

The failure criterion proposed by Drucker and Prager (1952) is a simplification of the Mohr-Coulomb failure criterion to take into account the dependence on both $\sqrt{J_2}$

and I_1. The standard failure criterion is a linear combination of these invariants and can be written in the form

$$\alpha I_1 + \sqrt{J_2} = \bar{k} \tag{3.11}$$

where α and $\bar{k}$ are material parameters governing failure.

In the computational code ABAQUS, a choice of three different yield criteria is provided for extended Drucker-Prager type models, which are described as being either linear, hyperbolic, or an exponential forms. In this thesis, the hyperbolic form of Drucker-Prager failure criterion is selected due to its ability to combine simultaneously the compressive and tensile failure, which is considered to be suitable for brittle materials, such as rocks and concrete. The extended form of Drucker-Prager failure criterion is given by the relationship

$$\sqrt{l_0^{\,2} + 3J_2} + \tfrac{1}{3} I_1 \tan\beta = d' \tag{3.12}$$

with an asymptotic line defined by

$$\sqrt{3J_2} + \tfrac{1}{3} I_1 \tan\beta = d' \tag{3.13}$$

where $l_0 = d' - \dfrac{f_t}{3}\tan\beta$; $d' = \sqrt{l_0^{\,2} + d^2}$ is hardening parameter; d is the cohesion of material; and β is the friction angle corresponding to the limiting values of $\frac{1}{3} I_1 = \infty$. The asymptotic line of the hyperbolic form of the extended Drucker-Prager failure criterion will be identical to the classical conical form of Drucker-Prager failure criterion if

$$\begin{aligned} \alpha &= \frac{1}{3\sqrt{3}}\tan\beta \\ \bar{k} &= \frac{d'}{\sqrt{3}} \end{aligned} \quad . \tag{3.14}$$

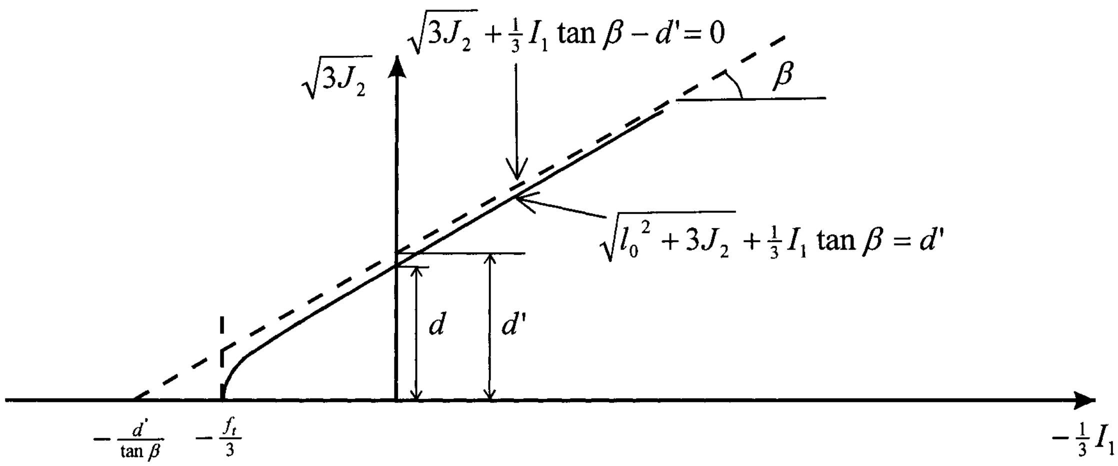

Figure 3.5 Drucker-Prager failure criterion with tension cut-off (hyperbolic form of Drucker-Prager failure criterion)

3.3 Flow rules

To complete the description of plastic behavior of the geomaterials, it is necessary to postulate a constitutive relation, which relates the mechanical variables to the kinematic variables. Since the plasticity theories generally involve non-linear responses, it is necessary to specify these constitutive responses in relation to incremental values of the mechanical and kinematic variables. The relationship between the incremental values of stresses $d\sigma_{ij}$ and the incremental values of strain $d\varepsilon_{ij}$ can only be postulated by examining experimental data conducted on specific geomaterials. A fundamental consideration in the development of incremental plastic stress-strain relations centers around the concept of a plastic potential. When considering elastic behavior of materials, the strain energy function can be expressed in terms of the stress state in the material and the strain components ε_{ij} can be obtained by differentiating the strain energy function W with respect to the corresponding stress component σ_{ij}, i.e.

$$W = W(\sigma_{ij}) \tag{3.15}$$

and

$$\varepsilon_{ij} = \frac{\partial W}{\partial \sigma_{ij}} \tag{3.16}$$

The plastic potential is the analogue of the strain energy function for plastic behavior of the material. If we assume the existence of a plastic potential $g(\sigma_{ij})$ then we can determine the incremental components of the plastic strains from the relationship

$$\mathrm{d}\varepsilon_{ij}^{p} = \mathrm{d}\lambda \frac{\partial g}{\partial \sigma_{ij}} \tag{3.17}$$

where $\mathrm{d}\lambda$ is a plastic multiplier or a loading parameters, which needs to be determined. Hence, if $\mathrm{d}\lambda$ and g can be determined, the plastic strain increments can be determined. When the plastic potential g is identical to the failure criterion f, the flow rule is said to be associated. Many of the plasticity theories currently employed in research and design take the advantage of the associative flow rule in view of its simplicity and other advantages resulting from development of collapse loads based on limit theorems.

In addition to plastic strains, the geomaterial can also exhibit elastic deformation and the incremental elastic strains, say, for an isotropic elastic material (see e.g. Timoshenko and Goodier, 1970; Davis and Selvadurai, 1996; Chen, 1981) are given by

$$\mathrm{d}\varepsilon_{ij}^{e} = \frac{1}{2G}\mathrm{d}\sigma_{ij} - \frac{1}{27K}\mathrm{d}\sigma_{kk}\delta_{ij} \tag{3.18}$$

and the total incremental strain tensor is given by

$$\mathrm{d}\varepsilon_{ij} = \mathrm{d}\varepsilon_{ij}^{e} + \mathrm{d}\varepsilon_{ij}^{p} \tag{3.19}$$

If the plastic potential $g \neq f$, then the resulting theory of plasticity is based on a non-associated flow rule and experimental results should be used to determine the specific form of g. Zienkiewicz and Taylor (2000) give a comparison of numerical results of slope stability when associate and non-associate plastic laws are used in conjuction with the Mohr-Coulomb failure criterion. It was found that, although very appreciable differences in plastic strain patterns exist, only moderate differences occur in the collapse load. Combining (3.16) and (3.17), the incremental strains in the plastically deforming geomaterial are defined provided that $\mathrm{d}\lambda$ is defined. Considering the definition of the plastic behavior we have

$$\mathrm{d}\lambda \begin{cases} = 0 & \text{if } f(\sigma_{ij}) < k' \text{ or } f = k' \text{ but } \mathrm{d}f < 0 \\ > 0 & \text{if } f = k' \text{ and } \mathrm{d}f = 0 \end{cases} \tag{3.20}$$

Using the consistency condition

$$\mathrm{d}f = \frac{\partial f}{\partial \sigma_{ij}} \mathrm{d}\sigma_{ij} = 0 \tag{3.21}$$

we can show (see e.g. Chen , 1981)

$$\mathrm{d}\lambda = \frac{\dfrac{\partial f}{\partial \sigma_{ij}} \mathrm{d}\varepsilon_{ij} + \dfrac{3K - 2G}{6G} \mathrm{d}\varepsilon_{kk} \dfrac{\partial f}{\partial \sigma_{ij}} \delta_{ij}}{\dfrac{\partial f}{\partial \sigma_{ij}} \dfrac{\partial f}{\partial \sigma_{ij}} + \dfrac{3K - 2G}{6G} \dfrac{\partial f}{\partial \sigma_{ij}} \dfrac{\partial f}{\partial \sigma_{mn}} \delta_{ij} \delta_{mn}} \tag{3.22}$$

once f is specified, $\mathrm{d}\lambda$ can be determined through (3.22). For example, for the Drucker-Prager material

$$\mathrm{d}\sigma_{ij} = 2G\mathrm{d}\xi_{ij} + K\mathrm{d}\varepsilon_{kk}\delta_{ij} - \mathrm{d}\lambda\left(\frac{G}{\sqrt{J_2}} s_{ij} + 3K\alpha\delta_{ij}\right) \tag{3.23}$$

where ξ_{ij} is the deviator tensor defined in equation (3.7), and

$$\mathrm{d}\lambda = \frac{(G / \sqrt{J_2}) s_{mn} \mathrm{d}\xi_{mn} + 3K\alpha \mathrm{d}\varepsilon_{kk}}{G + 9K\alpha^2} \tag{3.24}$$

and (3.23) can be rewritten as an incremental stress-strain relation in the form of

$$d\sigma_{ij} = (D^e_{ijkl} + D^p_{ijkl})d\varepsilon_{kl} \tag{3.25}$$

where

$$D^e_{ijkl} = 2G\delta_{ik}\delta_{jl} + (K - \tfrac{2}{3}G)\delta_{ij}\delta_{kl} \tag{3.26}$$

$$D^p_{ijkl} = -\frac{1}{G+9K\alpha^2}\left(\frac{G}{\sqrt{J_2}}s_{ij} + 3K\alpha\delta_{ij}\right)\left(\frac{G}{\sqrt{J_2}}s_{kl} + 3K\alpha\delta_{kl}\right) \tag{3.27}$$

3.4 The Coulomb friction model

The focus of the thesis involves the consideration of both plasticity of the geomaterial and non-linear process that can be attributed to surface in contact. Such surfaces in contact can result from interaction of fractured surfaces. The process that can occur at fractured or separated geomaterial can include Coulomb friction, separation and slip. The constitutive modelling of geomaterial and material interface responses has been the subject of several studies. Detailed accounts of current developments are given by Goodman and Brekke (1968), Selvadurai and Voyiadjis (1986), Selvadurai and Boulon (1995), Desai (2001). The most elementary form of constitutive modelling of non-linear processes at an interface utilizes the Coulomb friction model.

In the Coulomb friction model, it is assumed that, when the two planar surfaces are in contact, there is no relative motion between surfaces in contact until the frictional stress τ reaches a critical stress $\tau_{crit} = \mu p$, where μ is the coefficient of friction and p is the pressure normal to contact plane.

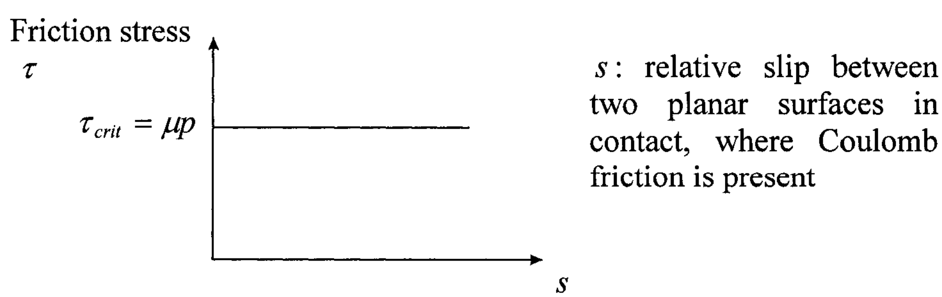

Figure 3.6 Mohr-Coulomb friction model

The classical Coulomb friction model as illustrated in Figure 3.6 is accurate only when the contacting surfaces are idealised planar surfaces. Surfaces in contact, in reality, are seldom planar. The fluctuation of the topography of the surfaces leads to the presence of contact only at a limited number of asperities (see Figure 3.7). This also occurs as a result of damage processes during movement of regular contacting surfaces, lodging debris at the contacting surfaces.

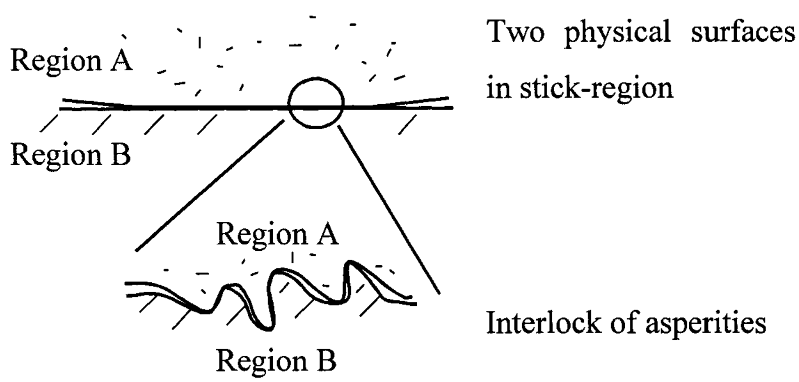

Figure 3.7 Illustration of limitation of numerical discretization of surface

This leads to the modification of Coulomb friction model, which exhibits deformation prior to slip. Such models have been considered extensively in the literature on both frictional contact modelling and modelling of geomaterial interfaces. This general constitutive behavior can be non-linear; a simplification, however, assumes an elastic-plastic response. In the elastic-plastic modelling, the notion of elastic stiffness in slip is introduced and the maximum elastic slip is restrained by the failure of asperities at the contacting surfaces, and the interface slip occurs in a linearly elastic fashion prior to the attainment of shear failure: i. e.,

$$\tau = k_s s \,, \tag{3.28}$$

where $k_s = \dfrac{\tau_{crit}}{s_{crit}} = \dfrac{\mu p}{s_{crit}}$ is the stiffness during slip and s_{crit} is the maximum elastic slip. A larger value of s_{crit} leads to a lower stiffness in slip. The elastic-plastic slip formulation for the shear behavior of the frictional surface takes the form

$$\begin{aligned} \mathrm{d}\tau &= k_s \mathrm{d}s + \frac{\mu s}{s_{crit}} \mathrm{d}p \qquad \text{if} \quad \tau < \tau_{crit} = \mu p \\ \mathrm{d}\tau &= \mu \mathrm{d}p \qquad\qquad\qquad \text{if} \quad \tau \geq \tau_{crit} \end{aligned} \tag{3.29}$$

The elastic-plastic frictional model is illustrated in Figure 3.8.

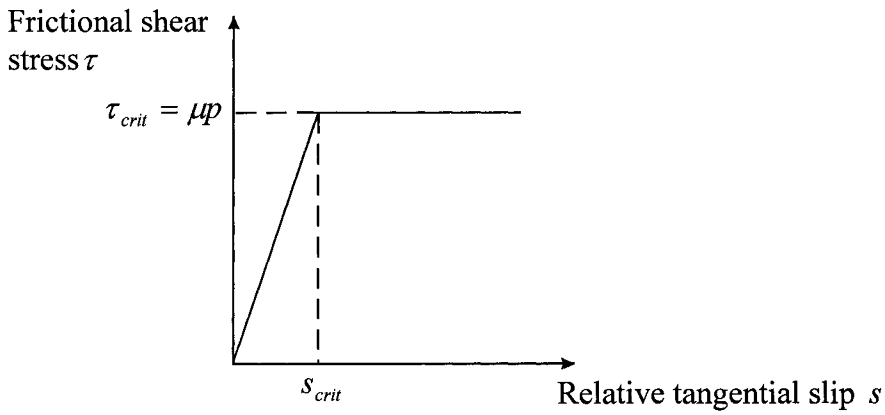

Figure 3.8 Elastic-sticky friction model when $\mathrm{d}p = 0$

3.5 Computational Implementation

Special efforts have been made to calibrate the parameters for the failure criterion of geomaterial. In view of the fact that computational modelling is performed using a commercially available computational code, the chapter also discusses the representation of the failure criterion in term of parameters used in the computational scheme.

3.5.1 Calibrating parameters for the hyperbolic form of Drucker-Prager failure criterion

The Mohr-Coulomb failure criterion assumes that failure is independent of the value of the intermediate principal stress σ_2. The Drucker-Prager model, however, accounts for the influence of σ_2. The failure of typical geomaterials generally includes some dependency on the intermediate principal stress σ_2. Implementation of Drucker-Prager model as a yield criterion for geomaterial will be more appropriate in situations involving plane strain behavior. The geomaterial strength parameters f_c and f_t, however, cannot be used directly to define the hyperbolic form of extended Drucker-Prager failure criterion as implemented in ABAQUS. They need to be related to parameters in Mohr-Coulomb failure criterion. This in turn can be related to parameters in Drucker-Prager failure criterion by a mapping method, where the strength variables of material f_c and f_t are expressed in terms of parameters in hyperbolic form of extended Drucker-Prager failure criterion.

The Mohr-Coulomb failure criterion can be rewritten in the form of

$$\left(\frac{\sigma_1 - \sigma_3}{2}\right) + \left(\frac{\sigma_1 + \sigma_3}{2}\right)\sin\phi - c\cos\phi = 0 \tag{3.30}$$

or in the form

$$\frac{\sigma_1}{f_t} - \frac{\sigma_3}{f_c} = 1 \tag{3.31}$$

where σ_1 and σ_3 are the major and minor principal stresses.

In (3.31),

$$f_c = \frac{2c\cos\phi}{1-\sin\phi}$$
$$f_t = \frac{2c\cos\phi}{1+\sin\phi}, \tag{3.32}$$

and the results can also be expressed in the form

$$\sin\phi = \frac{f_c - f_t}{f_c + f_t}$$
$$c = \frac{\sqrt{f_c f_t}}{2} \tag{3.33}$$

The modified equivalent of the Mohr-Coulomb failure criterion is illustrated in Figure 3.9.

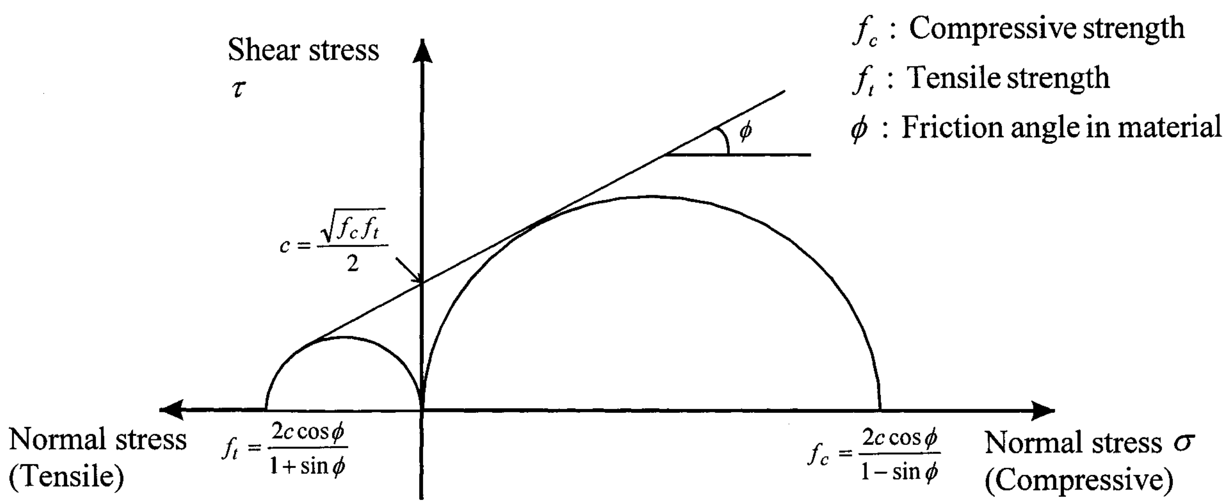

Figure 3.9 Modified form of Mohr-Coulomb criterion

The Mohr-Coulomb failure criterion has an irregular hexagonal three-dimensional shape in the principal stress space. As such, it has corners. In application of the theory to computation, these corner regions can contribute to numerical problems. The Drucker-Prager failure criterion is a conical surface in the principal stress space. It can be viewed as a smooth approximation to Mohr-Coulomb failure criterion to avoid such difficulties (Figure 3.10). The Drucker-Prager failure criterion can be made to match the Mohr-Coulomb failure criterion by adjusting the size of circle. For example, if the Drucker-Prager failure criterion is made to agree with the outer apices of the Mohr-Coulomb hexagon, the constant α and $\bar{k}$ can be related to c and ϕ according to

$$\begin{aligned} \alpha &= \frac{2\sin\phi}{\sqrt{3}(3-\sin\phi)} \\ \bar{k} &= \frac{6c\cos\phi}{\sqrt{3}(3-\sin\phi)} \end{aligned} \quad . \tag{3.34}$$

If the Drucker-Prager failure criterion is to match the inner apices of the Mohr-Coulomb hexagon, the constants of the two criteria can be related by the following equations as

$$\begin{aligned} \alpha &= \frac{2\sin\phi}{\sqrt{3}(3+\sin\phi)} \\ \bar{k} &= \frac{6c\cos\phi}{\sqrt{3}(3+\sin\phi)} \end{aligned} \quad . \tag{3.35}$$

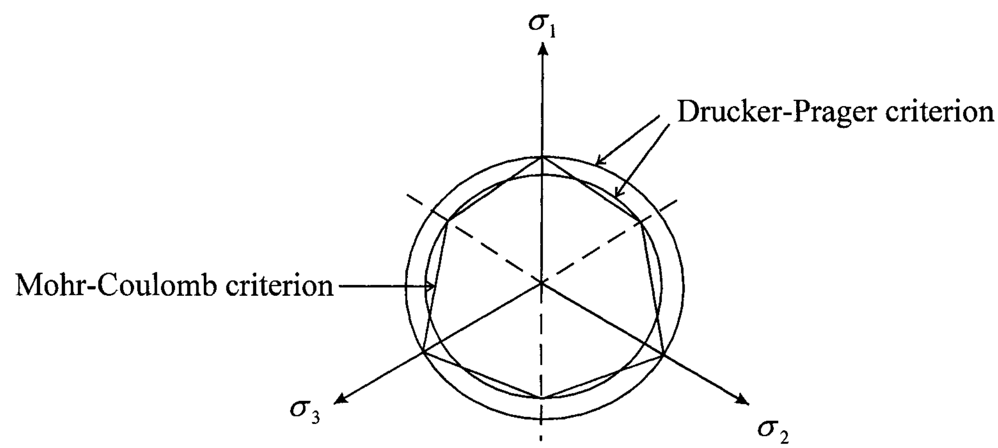

Figure 3.10 Shape of the yield criteria on the π plane

Under plane strain conditions, the two criteria give identical limit load for any region of a perfectly plastic material (see e.g. Chen, 1981). This is based on the assumption of perfect plasticity, where there are no elastic deformations at the collapse of material. The total-strain increment component $d\varepsilon_{ij}$ after yielding will be fully identical to the plastic-strain increment $d\varepsilon_{ij}^p$, which is

$$d\varepsilon_{ij}^p = d\lambda \frac{\partial f}{\partial \sigma_{ij}} = d\lambda(\alpha\delta_{ij} + \frac{1}{2\sqrt{J_2}} s_{ij}) \tag{3.36}$$

where s_{ij} is the stress deviator tensor. Assuming plane strain in y-direction or 2-direction and using plane strain condition, i.e. $d\varepsilon_{yy}^p = d\varepsilon_{xy}{}^p = d\varepsilon_{yz}{}^p = 0$, it follows that

$$\begin{aligned} s_{yy} &= -2\alpha\sqrt{J_2} \\ s_{xy} &= s_{yz} = \tau_{yz} = \tau_{yz} = 0 \end{aligned} . \tag{3.37}$$

and

$$\begin{aligned} I_1 &= \tfrac{3}{2}(\sigma_{xx} + \sigma_{zz}) - 3\alpha\sqrt{J_2} = \tfrac{3}{2}(\sigma_1 + \sigma_3) - 3\alpha\sqrt{J_2} \\ J_2 &= \frac{[(\sigma_{xx} - \sigma_{zz})/2]^2 + \tau_{xz}{}^2}{1 - 3\alpha^2} = \frac{[(\sigma_1 - \sigma_3)/2]^2}{1 - 3\alpha^2} \end{aligned} \tag{3.38}$$

The Drucker-Prager failure criterion can be rewritten as

$$3\alpha(\frac{\sigma_1 + \sigma_3}{2}) + (1 - 3\alpha^2)\sqrt{J_2} = 3\alpha\frac{\sigma_1 + \sigma_3}{2} + \sqrt{1 - 3\alpha^2}(\frac{\sigma_1 - \sigma_3}{2}) = \bar{k} \tag{3.39}$$

which is identical with Mohr-Coulomb failure criterion in equation (3.30), if we set

$$\begin{aligned} c\cos\phi &= \frac{\bar{k}}{\sqrt{1 - 3\alpha^2}} \\ \sin\phi &= \frac{3\alpha}{\sqrt{1 - 3\alpha^2}} \end{aligned} . \tag{3.40}$$

Solving for $\bar{k}$ and α, we obtain

$$\begin{aligned} \alpha &= \frac{\sin\phi}{\sqrt{3(3+\sin^2\phi)}} \\ \bar{k} &= \frac{3c\cos\phi}{\sqrt{3(3+\sin^2\phi)}} \end{aligned} \quad . \tag{3.41}$$

One possible way to obtain the parameters for the hyperbolic form of extended Drucker-Prager failure criterion from Mohr-Coulomb failure criterion is to match the Mohr-Coulomb failure criterion with the asymptotic line of the hyperbolic form. This line has the same form as that of classical form of Drucker-Prager failure criterion. Considering (3.14), (3.33) and (3.41), the parameters β and d' for the hyperbolic form of Drucker-Prager failure criterion are then available through equations

$$\begin{aligned} \tan\beta &= \frac{3\sin\phi}{\sqrt{3+\sin^2\phi}} \\ \frac{d'}{c} &= \frac{3\cos\phi}{\sqrt{3+\sin^2\phi}} \end{aligned} \tag{3.42}$$

where

$$\begin{aligned} \phi &= \sin^{-1}\left(\frac{f_c - f_t}{f_c + f_t}\right) \\ c &= \frac{\sqrt{f_c f_t}}{2} \end{aligned} \quad . \tag{3.43}$$

When f_c and f_t are obtained through experiments, then β and d' can be calculated using above results. Bandis and Barton (1983) conducted shear experiments on dolerite joints. The strength parameters for dolerite determined in these experiments are $f_c = 165\,\text{MPa}$ and $f_t = 17.3\,\text{MPa}$. Using (3.42) and (3.43), we obtain $\beta = 51.8^\circ$ and $d' = 24.6\,\text{MPa}$.

3.5.2 Strain energy in material regions

The relative shear between two material regions involves deformation of material and relative sliding between material boundaries. The total energy Π is then a combination of strain energy U in material region and frictional energy dissipation Θ in the interface. The stiffness matrix for the material experiencing elasto-plastic deformation can be found by using the incremental stress-strain relations (3.25), (3.26) and (3.27). Rewriting them in vector and matrix forms, we have

$$\mathrm{d}\boldsymbol{\sigma} = \mathbf{D}^{\mathrm{ep}}\mathrm{d}\boldsymbol{\varepsilon} \tag{3.44}$$

where

$$\mathbf{D}^{\mathrm{ep}} \begin{cases} = \mathbf{D}^{\mathrm{e}} & \text{when no plasticity occurs} \\ = \mathbf{D}^{\mathrm{e}} + \mathbf{D}^{\mathrm{p}} & \text{when yielding occurs} \end{cases} \tag{3.45}$$

where $\mathbf{D}^{\mathrm{e}}$ is constitutive matrix due to elastic deformation and $\mathbf{D}^{\mathrm{p}}$ is a constitutive matrix due to plastic deformation. The elasto-plastic constitutive matrix is combination of two factors, i.e., $\mathbf{D}^{\mathrm{e}}$ and $\mathbf{D}^{\mathrm{p}}$. In a displacement formulation involving small deformation, the rotations do not enter the computation. The degrees of freedom for a point coincide with its spatial coordinates $\mathbf{x}$, and can be interpolated by global nodal coordinates $\mathbf{x}_{\mathrm{i}}^{\mathrm{T}} = (x_i, y_i, z_i)$

$$\mathbf{x} = N_i \mathbf{x}_{\mathrm{i}} = \mathbf{N}^{\mathrm{T}}\mathbf{a} \tag{3.46}$$

where N_i is the interpolation function from contribution of node *i*. In (3.46) vector $\mathbf{N}^{\mathrm{T}}$ is a matrix of the form

$$\mathbf{N}^{\mathrm{T}} = \begin{bmatrix} N_1 & 0 & 0 & N_2 & 0 & 0 \ldots N_n & 0 & 0 \\ 0 & N_1 & 0 & 0 & N_2 & 0 \ldots 0 & N_n & 0 \\ 0 & 0 & N_1 & 0 & 0 & N_2 \ldots 0 & 0 & N_n \end{bmatrix}, \tag{3.47}$$

where n is the number of total nodes, and $\mathbf{a}$ is a sequential list of the spatial degrees of freedom of each node defined by

$$\mathbf{a}^{\mathrm{T}} = (x_1, y_1, z_1, x_2, y_2, z_2, \ldots x_n, y_n, z_n). \tag{3.48}$$

The strain vector $\boldsymbol{\varepsilon}$ is determined from the spatial coordinate $\mathbf{x}$

$$\boldsymbol{\varepsilon} = \mathbf{L}\mathbf{x} = \mathbf{L}\mathbf{N}^{\mathrm{T}}\mathbf{a} = \mathbf{B}\,\mathbf{a} \tag{3.49}$$

where $\mathbf{B} = \mathbf{L}\mathbf{N}^{\mathrm{T}}$ is a matrix relating the strain at one point to coordinates of each node and $\mathbf{L}$ is a combination of partial derivatives arranged in a matrix form, to determine strain at that point (see e.g. Zienkiewicz and Taylor, 2000)

$$\mathbf{L} = \begin{bmatrix} \frac{\partial}{\partial x} & 0 & 0 \\ 0 & \frac{\partial}{\partial y} & 0 \\ 0 & 0 & \frac{\partial}{\partial z} \\ 0 & \frac{\partial}{\partial z} & \frac{\partial}{\partial y} \\ \frac{\partial}{\partial z} & 0 & \frac{\partial}{\partial x} \\ 0 & \frac{\partial}{\partial z} & \frac{\partial}{\partial y} \end{bmatrix}. \tag{3.50}$$

The incremental strain vector can then be expressed in terms of incremental changes of each node's coordinates

$$\mathrm{d}\boldsymbol{\varepsilon} = \mathbf{B}\,\mathrm{d}\mathbf{a} + \mathrm{d}\mathbf{B}\,\mathbf{a}. \tag{3.51}$$

And the incremental stress can also be expressed in terms of incremental changes of each node's coordinates

$$\mathrm{d}\boldsymbol{\sigma} = \mathbf{D}^{\mathrm{ep}}\mathbf{B}\,\mathrm{d}\mathbf{a} + \mathbf{D}^{\mathrm{ep}}\mathrm{d}\mathbf{B}\,\mathbf{a}. \tag{3.52}$$

The strain energy δU then is determined by

$$\delta U = \int_V \delta\boldsymbol{\varepsilon}^{\mathrm{T}}\boldsymbol{\sigma}\,\Delta V \tag{3.53}$$

The complete form of second variation of strain energy U is

$$\begin{aligned}
\mathrm{d}\delta U &= \mathrm{d}\int_V \delta\boldsymbol{\varepsilon}^{\mathrm{T}}\boldsymbol{\sigma}\Delta V = \int_V \mathrm{d}\delta\boldsymbol{\varepsilon}^{\mathrm{T}}\boldsymbol{\sigma}\,\Delta V + \int_V \delta\boldsymbol{\varepsilon}^{\mathrm{T}}\mathrm{d}\boldsymbol{\sigma}\,\Delta V + \int_V \delta\boldsymbol{\varepsilon}^{\mathrm{T}}\boldsymbol{\sigma}\,\mathrm{d}\Delta V \\
&= \Big(\int_V \delta\mathbf{a}^{\mathrm{T}}\mathrm{d}\mathbf{B}\,\boldsymbol{\sigma}\,\Delta V + \int_V \delta\mathbf{a}^{\mathrm{T}}\mathbf{B}^{\mathrm{T}}\mathbf{D}^{\mathrm{ep}}\mathrm{d}\mathbf{B}\,\mathbf{a}\,\Delta V\Big) + \int_V \delta\mathbf{a}^{\mathrm{T}}\mathbf{B}^{\mathrm{T}}\mathbf{D}^{\mathrm{ep}}\mathbf{B}\,\mathrm{d}\mathbf{a}\,\Delta V \\
&+ \int_V \delta\boldsymbol{\varepsilon}^{\mathrm{T}}\boldsymbol{\sigma}\,\mathrm{d}\Delta V = \delta\mathbf{a}^{\mathrm{T}}(\mathbf{K}^{\mathrm{n}} + \mathbf{K}^{\mathrm{ep}} + \mathbf{K}^{\mathrm{V}})\mathrm{d}\mathbf{a}^{\mathrm{T}} \\
&= \delta\mathbf{a}^{\mathrm{T}}\mathbf{K}\,\mathrm{d}\mathbf{a}^{\mathrm{T}}
\end{aligned} \tag{3.54}$$

where $\mathbf{K}$ is the current stiffness matrix in material regions V, which is a combination of several contributions: (i) $\mathbf{K}^{\mathrm{n}}$ is a part of the stiffness matrix due to the non-linear geometry associated with large displacement, which reduces to zero in the absence of large displacements; (ii) $\mathbf{K}^{\mathrm{ep}}$ is a part of the stiffness matrix due to elastic and plastic deformation of the material; (iii) $\mathbf{K}^{\mathrm{V}}$ is a part of the stiffness term due to volume change or dilatancy of the material. If finite deformations or large strains are excluded, the effect from change of mass volume and geometry can be neglected, and the global stiffness matrix for the problem involving relative shear between two material regions is a combination of the contribution from elasto-plastic deformation in material regions and relative slip and separation in the interface, which will be discussed in Section 3.5.3.

3.5.3 Finite sliding between deformable bodies

Another part of comtribution to total energy Π is the frictional dissipatioin Θ in the interface. The application of shear forces to a joint results in relative sliding, seperation or establishment of new contacts between the contacting surfaces. The slip between surfaces of the joint, or relative shear displacement, is a different concept to tangential slip between surfaces in contact shown in Figure 3.11. Shear displacement describes the overall relative movement between joints, while tangent slip between surfaces in contact refers to the local relative movements between regions in contact, which are parts of the joint surfaces.

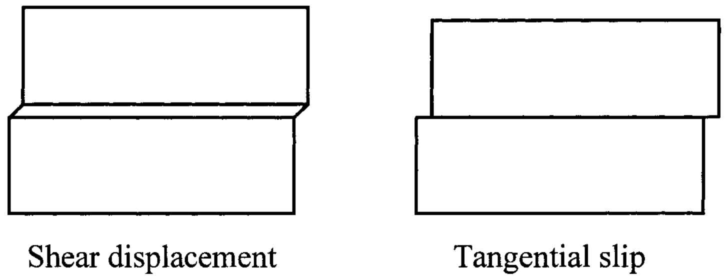

Figure 3.11 Concepts of shear displacement and tangent slip

The ABAQUS code adopts a *finite sliding formulation* to account for separation and sliding of finite amplitude and arbitrary rotation of the surfaces in contact. Consider a potential contact node n_1 with a segment of surface described by node n_2, n_3.... For a linear segment, the number of nodes is 2, whereas for a quadratic segment the number of nodes is 3 as shown in Figure 3.12.

To derive the equations governing the elements, the coordinates of nodes have been assigned, as shown in Figure 3.12. If we consider that point $\mathbf{x}$ on the segment is closest to the potential contact point $\mathbf{x}_1$, then the closure h between $\mathbf{x}$ and $\mathbf{x}_1$ can be expressed in terms of normal vector $\mathbf{n}$, coordinates $\mathbf{x}$ and $\mathbf{x}_1$ as

$$\mathbf{n}h = \mathbf{x} - \mathbf{x}_1 \tag{3.55}$$

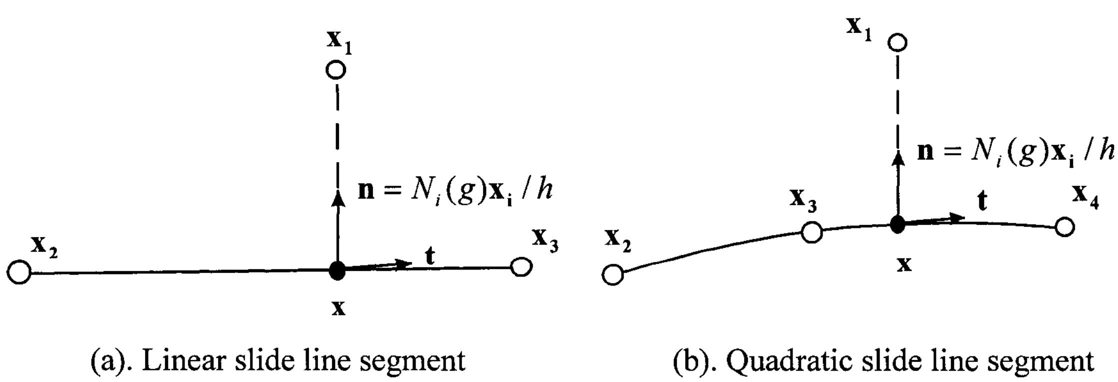

Figure 3.12 Contact of a node with a segment of the surface

Since $\mathbf{x}$ is on the segment, its position is defined completely by the interpolation function N_i for the segment, the position g and the position $\mathbf{x}_i$ of the nodes n_i that are part of the segment.

$$\mathbf{n}h = N_i(g)\mathbf{x}_i \tag{3.56}$$

where $N_1 = -1$ and N_2, N_3 ... are functions of g. For instance, for a linear segment,

$$\begin{aligned} N_2 &= \tfrac{1}{2}(1-g) \\ N_3 &= \tfrac{1}{2}(1+g) \end{aligned} . \tag{3.57}$$

For a quadratic segment,

$$\begin{aligned} N_2 &= \tfrac{1}{2}g(g-1) \\ N_3 &= 1-g^2 \\ N_4 &= \tfrac{1}{2}g(g+1) \end{aligned} . \tag{3.58}$$

The tangent $\mathbf{t}$ to sliding line at point $\mathbf{x}$ follows with

$$\mathbf{t} \stackrel{def}{=} \frac{\mathrm{d}\mathbf{x}}{\mathrm{d}s} = \frac{\mathrm{d}\mathbf{x}}{\mathrm{d}g} \bigg/ \left|\frac{\mathrm{d}\mathbf{x}}{\mathrm{d}g}\right| \tag{3.59}$$

where

$$\frac{\mathrm{d}\mathbf{x}}{\mathrm{d}g} = \frac{\mathrm{d}N_i}{\mathrm{d}g}\mathbf{x}_i \tag{3.60}$$

The position g of point $\mathbf{x}$ is determined from the condition that normal and tangent must be orthogonal, i.e.,

$$\mathbf{n} \cdot \mathbf{t} = N_i(g)\frac{\mathrm{d}N_j(g)}{\mathrm{d}g}\mathbf{x}_i \cdot \mathbf{x}_j = 0 \tag{3.61}$$

Linearization of equation (3.61) yields

$$\delta\mathbf{n}h + \mathbf{n}\delta h = \frac{\mathrm{d}N_i}{\mathrm{d}g}\mathbf{x_i}\delta g + N_i\delta\mathbf{x_i} = \mathbf{t}\delta s + N_i\delta\mathbf{x_i} \tag{3.62}$$

where δs is first variation of the slip. In the direction of contact, $\mathbf{n}$,

$$\delta h = N_i\mathbf{n}\cdot\delta\mathbf{x_i}; \tag{3.63}$$

In the direction of slip, $\mathbf{t}$,

$$\delta s = -N_i\mathbf{t}\cdot\delta\mathbf{x_i} - h\mathbf{t}\cdot\delta\mathbf{n}. \tag{3.64}$$

If the nodes are in contact with segment, then $h = 0$, and

$$\delta s = -N_i\mathbf{t}\cdot\delta\mathbf{x_i}. \tag{3.65}$$

To obtain the initial stress-stiffness terms, the second variations of h and s must be calculated. They are

$$\begin{aligned}
\mathrm{d}\delta h &= -\delta\mathbf{x_i}\cdot(\mathbf{n}\frac{\mathrm{d}N_i}{\mathrm{d}s}N_j\mathbf{t} + \mathbf{t}N_i\frac{\mathrm{d}N_j}{\mathrm{d}s}\mathbf{n} + \mathbf{t}N_i\rho_n N_j\mathbf{t})\cdot\mathrm{d}\mathbf{x_j} \\
\mathrm{d}\delta s &= \delta\mathbf{x_i}\cdot(\mathbf{t}\frac{\mathrm{d}N_i}{\mathrm{d}s}N_j\mathbf{t} - \mathbf{n}N_i\frac{\mathrm{d}N_j}{\mathrm{d}s}\mathbf{n} - \mathbf{n}N_i\rho_n N_j\mathbf{t})\cdot\mathrm{d}\mathbf{x_j}
\end{aligned} \tag{3.66}$$

where $\rho_n \overset{def}{=} -\mathbf{n}\cdot\dfrac{\mathrm{d}^2\mathbf{x}}{\mathrm{d}g^2}\Bigg/\left|\dfrac{\mathrm{d}\mathbf{x}}{\mathrm{d}g}\right|^2$.

Then the variation of frictional energy dissipation Θ in the interface can be expressed as

$$\delta\Theta = \int_\Gamma \tau\delta s\,\Delta\Gamma \tag{3.67}$$

where Γ denotes the interface at two material boundaries. The second variation of Θ is obtained by

$$\mathrm{d}\delta\Theta = \int_\Gamma \mathrm{d}\tau\delta s\,\Delta\Gamma + \int_\Gamma \tau\,\mathrm{d}\delta s\,\Delta\Gamma \tag{3.68}$$

By defining surface interaction conditions, such as frictional properties and potential contact surfaces, ABAQUS then automatically identifies nodes in contact with surface segments. Slip and closure between the node and surface segment can represent the relative slip and separation between surfaces in contact.

3.6 Summary

The failure criterion proposed by Drucker and Prager has the added advantage over the Mohr-Coulomb failure criterion in that the complete set of principal stresses is used in its formulation. The Mohr-Coulomb failure criterion, as has been indicated, is independent of the intermediate principal stress acting on the material. The parameters in the hyperbolic form of extended Drucker-Prager failure criterion, implemented in computational code ABAQUS, can be related to material strength parameters f_c and f_t by a mapping method.

In the Coulomb friction model, it is assumed that, when the two planar surfaces are in contact, no relative motion occurs between them and two surfaces adhere together before the attainment of a critical frictional stress. The elastic-plastic model takes account of the fact that contacting surfaces interact each other at limited number of points and that surfaces in contact can exhibit deformation prior to slip.

Chapter 4

COMPUTATIONAL SIMULATION OF EXPERIMENTAL RESULTS

This chapter describes the adaptation of the ABAQUS finite element code to examine computationally the shear behavior of a fracture, which experiences both elasto-plastic material failure and frictional phenomena. Numerical simulations will be compared with a set of experimental data obtained for the variation of shear stress with shear displacement conducted by Bandis et al. (1983) on a natural unweathered dolerite joint of 100 mm length.

4.1 Computational modelling of the dolerite joint

The general arrangement of the shear test conducted on the natural joint of unweathered dolerite is described in Chapter 2. Because it is difficult to obtain an identical profile of a natural dolerite joint, the same joint was sheared repeatedly. Once the peak shear stress was reached, the shear load was released and the joint sample reassembled. A new test was performed on the same joint at a higher normal stress. The disadvantage of such testing procedure is that some asperities could have been damaged during shear at lower normal stress and as a result the peak shear stress under the higher normal stress may also be reduced. The asperity damage can also introduce some difference in the shear stiffness.

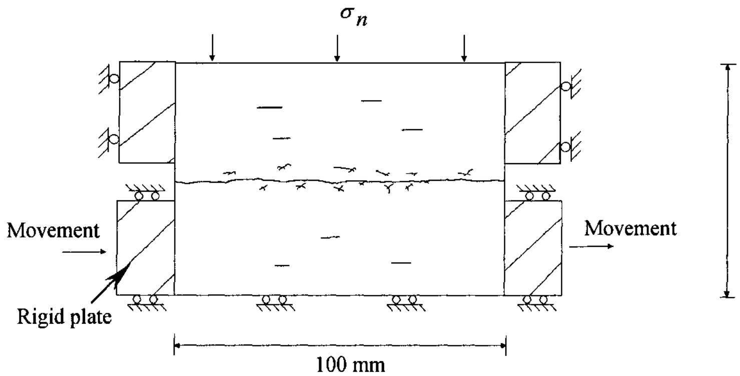

(a). Numerical model and boundary conditions

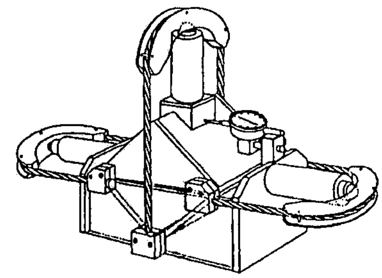

(b). Portable shear box

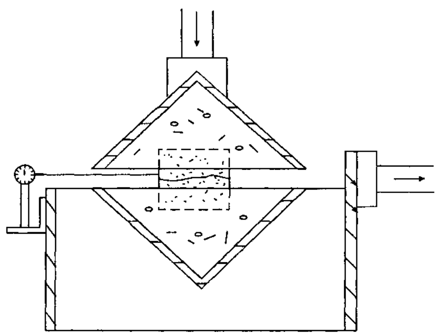

(c). Section view of shear box

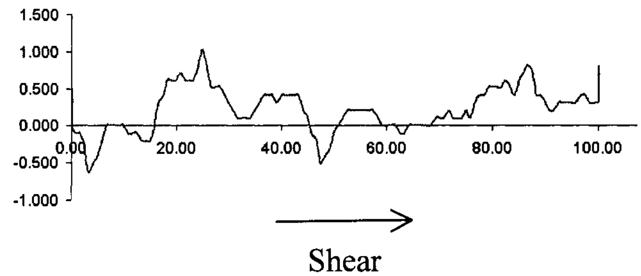

(d). 2D joint profile (after discretization)

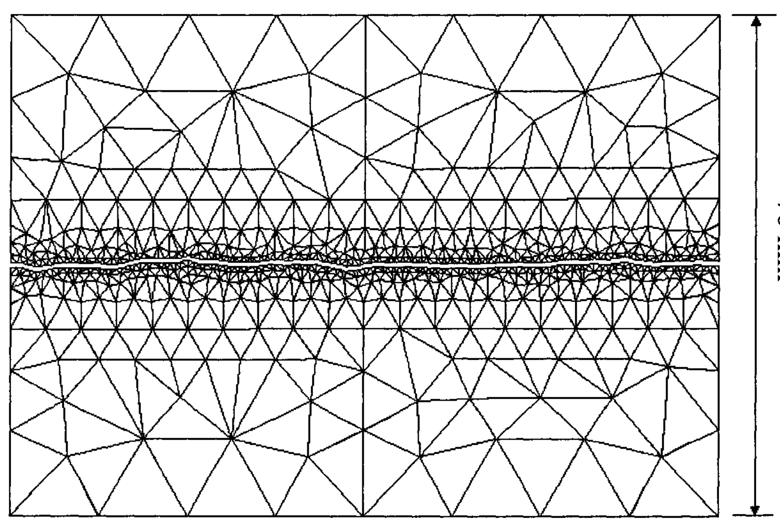

(e). Mesh configuration (initially compatible, 1194 elements and 2672 nodes)

Figure 4.1 Computational model for simulation

The joint is treated as a two-dimensional region, which exhibits plane strain behavior with the assumption that the behavior of the joint is interpreted through the behavior of a typical profile rather than that of a surface. This is the limitation in the modelling, which will not be discussed further. The Figure 4.1 shows the dimensions of the two-dimensional model used in computations. In the actual experiments, the lower part of the sample is constrained to move horizontally and the upper part is held by wire ropes. The rotation is not strictly controlled during the motion of upper part of the joint. The center of the rotation in the system is unknown. For a roughly planar joint similar to that used by Bandis et al. (1983), the effect from rotation is considered to be negligible. The upper and lower sections of the sample are cast in the shear box by concrete moulding material. The sample is assumed to be fully bonded to the moulding material. The loading, which induces shear, is applied on lower box through a system of jacks as shown in Figure 4.1(c). The line of application of horizontal force is approximately at the shear plane so that no moment is considered. A normal load is applied at the center of the upper box, which transmits this load directly to the joint surface.

To simulate the actual conditions of the experiments, constant stress is applied on the upper part of the model as shown in Figure 4.1(a). Two rigid plates are fully bonded on each side of upper part to simulate the fully bonded condition between the sample and the moulding material. Slip and separation are not allowed between the rigid plate and upper part of the sample. For the purpose of computational modelling, it is assumed that there is no rotation in two halves of the sample. Rotation of the whole upper part can be restrained on the rigid plates bonded on the segment of the upper part of the sample. The lower part is subjected to movement in the horizontal direction. Two rigid plates are also bonded on each side of the lower segment. In modelling the joint, the actual plane profile of the joint as determined from surface profiling is considered. It could be argued that infinite such representations are possible, depending on the accuracy of the measurement technique and location of the section considered. There are, however, certain constrainments that can be imposed as a result of the internal fabric of the rock and the necessity to include a sufficient number of particles on the scale of the grain of the rock to simulate a continuum point in the computational modelling. The grain size gives the smallest dimension of the surface discretization. The actual average grain size for dolerite varies between $0.05\,\text{mm}$ to $1\,\text{mm}$ (Wahlstrom, 1947). The value of $1\,\text{mm}$ roughly gives the smallest dimenstion of surface discretization. The accurate description of material at such a scale need take account of the microstructure of the material. The microstructure of rock mass is then disregarded in the computatinal simulation. Constraints are also imposed by the element size of the finite element discretization required for computational accuracy and efficiency. Within these constraints, the irregular surface profile [Figure 4.1(d)] as measured in an experiment is accurately duplicated in the discretization used in the finite element modelling as shown in Figure 4.1(e). The finite element discretization of the region close to the joint surface can be approached at various levels. This is largely influenced by the capacity of the computational facilities. The smallest element dimension near the joint is around $0.8\,\text{mm}$. Computational trials indicate that a further reduction in the size of an element close to the joint surface does not result in a marked change in numerical results. Modified 6-node triangular element, labeled as CPE6M and implemented in ABAQUS computational code, is used. In this formulation, stress is compatible between two adjacent elements.

The constitutive euqation used is the hyperbolic form of Drucker-Prager failure criterion discussed in Chapter 3. Material strength parameters f_c and f_t and Young's modulus E are given in the experimental data. The dilation angle and friction angle for the material are assumed to have a same value of β, which can be derived from f_c and f_t according to Chapter 3 [see equations (3.42) and (3.43)]. Poisson's ratio is chosen as 0.23, which is assumed to be a approximate value for dolerite type rock (Jaeger and Cook, 1976). The complete list of material properties is as follows

$$f_c = 159.0\ \text{MPa}; f_t = 17.3\ \text{MPa}; \beta = 51.8^\circ; E = 78\ \text{GPa}; \nu = 0.23. \tag{4.1}$$

With brittle geomaterials, the strains prior to failure are generally small; as such the large strain option is not necessary for the calculation of the stiffness matrix. To assure the numerical accuracy, a double precision solver is used at all times.

Complete computational simulation requires additional surface interaction modelling. Finite sliding formulation in computational code ABAQUS is adopted. Details of the finite sliding formulation were presented in Chapter 3. The surface interaction model is the Coulomb frictional model considering the elastic contact between surface asperities. Details are presented in Chapter 3. The parameters needed will include the coefficient of friction μ and the amount of maximum elastic slip γ_{crit}. The friction angle provided in experiments is approximately $\phi = 34^{\circ}$ or $\mu = 0.6745$. In literature, however, the friction coefficient for a planar dolerite surface is quite variable; i.e. 0.64 to 0.90. The actual variation of shear stress due to friction is expected to fall into a zone bounded by two limited cases where $\mu = 0.64$ and $\mu = 0.90$. No relevant information about the maximum elastic slip is available in the literature, as such, it needs to be back-calculated. The computational simulations are conducted on three cases involving changes in the normal stress. The normal stresses are assigned the values $0.52\,\mathrm{MPa}$, $1.05\,\mathrm{MPa}$ and $2.10\,\mathrm{MPa}$.

4.2 Some issues concerning computational simulation

The ability of the sample to rotate can influence the stress distribution normal to the shear plane. In the experiments conducted by Bandis et al. (1983), rotation is not strictly controlled. It is reported that rotation has some influence on the shear behavior for a very rough joint; for a relatively planar joint, influence of a rotation is negligible. For the convenience of computational modelling and throughout this thesis, the occurrence of a rotation is not considered.

A further aspect of the computational modelling involves the assessment of the mesh sensitivity (within restraints discussed in Section 4.1) on the compuational results. Figure 4.2 shows the computational results for shear behavior derived from two mesh configurations conducted at normal stress $2.10\,\mathrm{MPa}$. The finer mesh configuration includes double numbers of elements than the rougher one. No clear difference of shear behavior and dilatancy is observed for two cases. This proves the computational reliability.

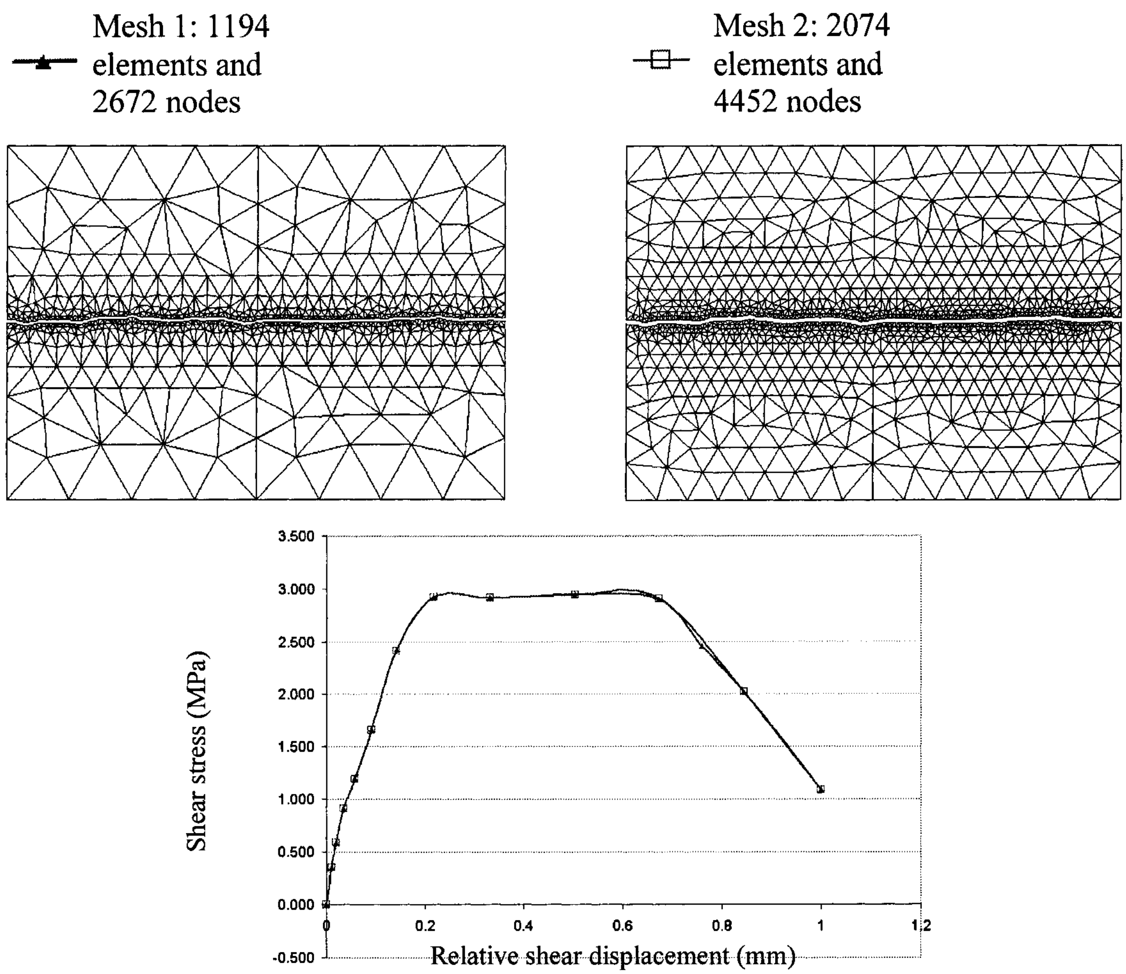

(a). Shear stress vs. relative shear displacement

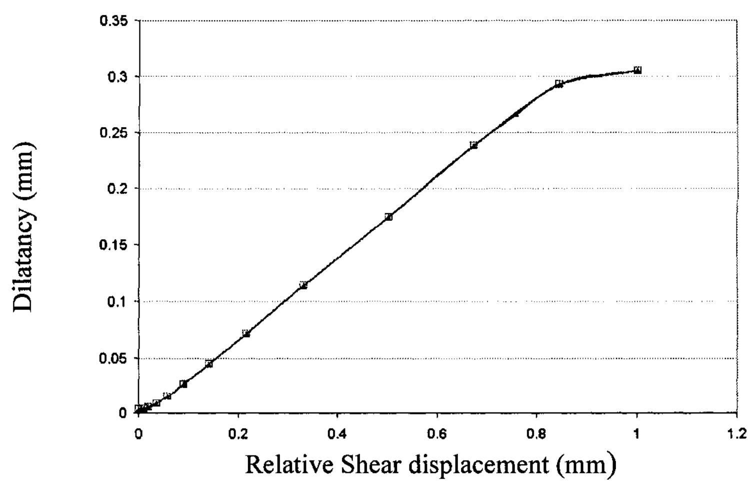

(b). Dilatancy vs. relative shear displacement

Figure 4.2 Shear behavior of the joint for two mesh discretizations

One unknown parameter is the maximum elastic slip γ_{crit}, which needs to be back-calculated through correlation with the experimental results. The effect of γ_{crit} can be examined by comparison of the shear behavior obtained by using different estimates of γ_{crit}. As indicated in Figure 4.3, different values of γ_{crit} do not affect peak shear stress, but results in twice different estimates of the shear stiffness.

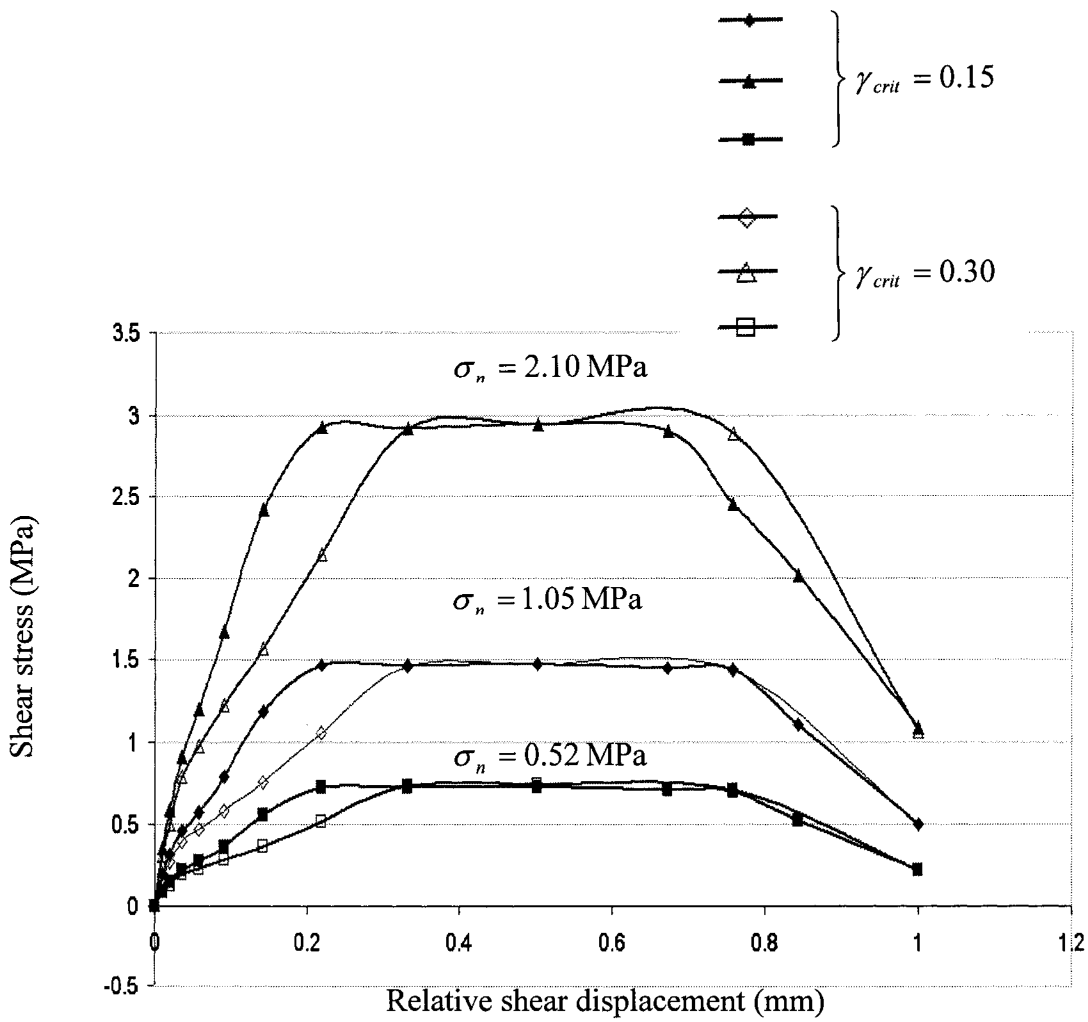

Figure 4.3 Effect from maximum elastic slip γ_{crit}

Finally, the remaining uncertainty in computational modelling is associated with the coefficient of friction μ. Although it is reported that $\mu = 0.6745$, it can vary depending upon the method of measurement. In literature, the friction coefficient for a planar dolerite surface is a variable, ranging from 0.64 to 0.90. The actual coefficient of friction might lie within this variation. Figure 4.4(a) and Figure 4.4(b) show the variation of shear behavior with the change of the coefficient of friction, for two cases where $\gamma_{crit} = 0.15$ and $\gamma_{crit} = 0.30$, respectively.

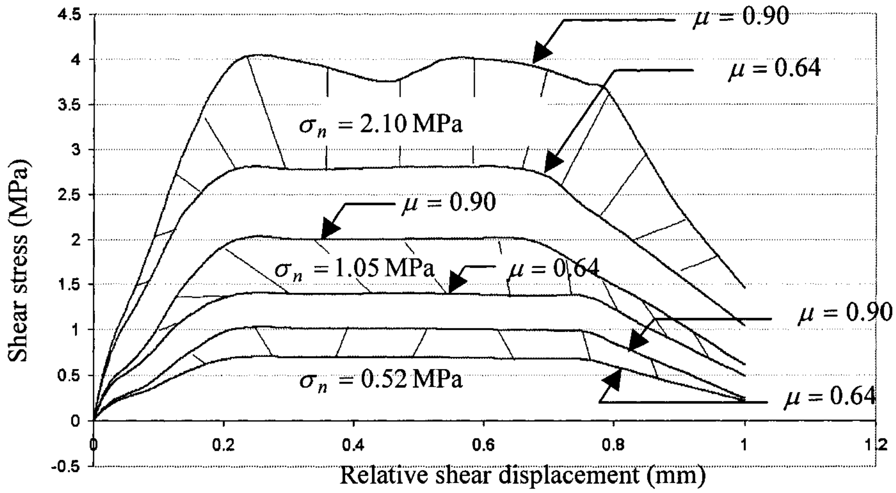

(a). $\gamma_{crit} = 0.15$

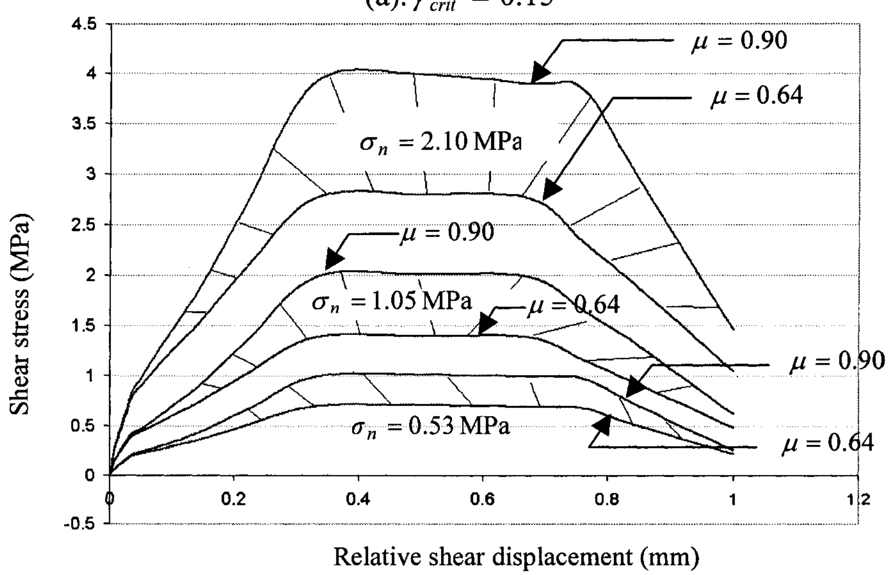

(b). $\gamma_{crit} = 0.30$

Figure 4.4 Variation of shear stress with the coefficient of friction

4.3 Comparison of computational results and experimental data

Both variation of maximum elastic slip γ_{crit} and the coefficient of friction have some influence on the computational simulation of experimental data. When the coefficient of friction at 0.6745 cited in experimental data and additional estimated value $\gamma_{crit} = 0.30$ is used, it is observed (Figure 4.5) that general trend of the computational estimates is similar to the experimental data. The peak shear stresses correlate well with results at lower normal stress values of $1.05\,\mathrm{MPa}$ and $0.53\,\mathrm{MPa}$. The shear stiffness is slightly overestimated at the higher normal stress of $2.10\,\mathrm{MPa}$, but slightly underestimated for lower stresses of $1.05\,\mathrm{MPa}$ and $0.52\,\mathrm{MPa}$.

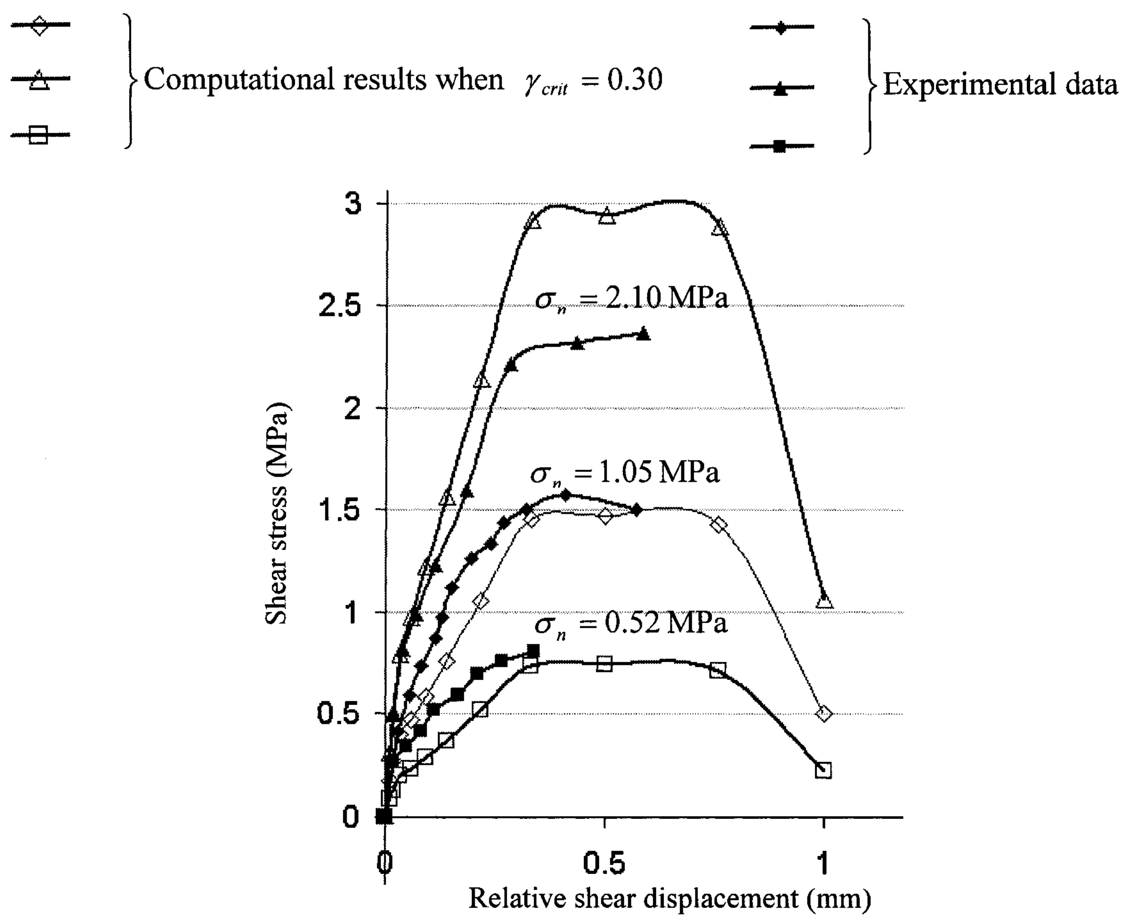

Figure 4.5 Computational simulation of experimental data when $\gamma_{crit} = 0.30$

When γ_{crit} is changed into 0.15, a better correlation is obtained at the lower normal stress values of 1.05 MPa and 0.52 MPa as shown in Figure 4.6. The peak shear stress is overestimated for the high normal stress of 2.10 MPa. This can be attributed to the repeated shear conducted on the same joint (discussed in Section 4.1), where some of the asperities are susceptible to damage at lower normal stresses and during peak shear stress. As a result, compuational results for shear stress and shear stiffness at higher normal stress are higher than those obtained in experiments.

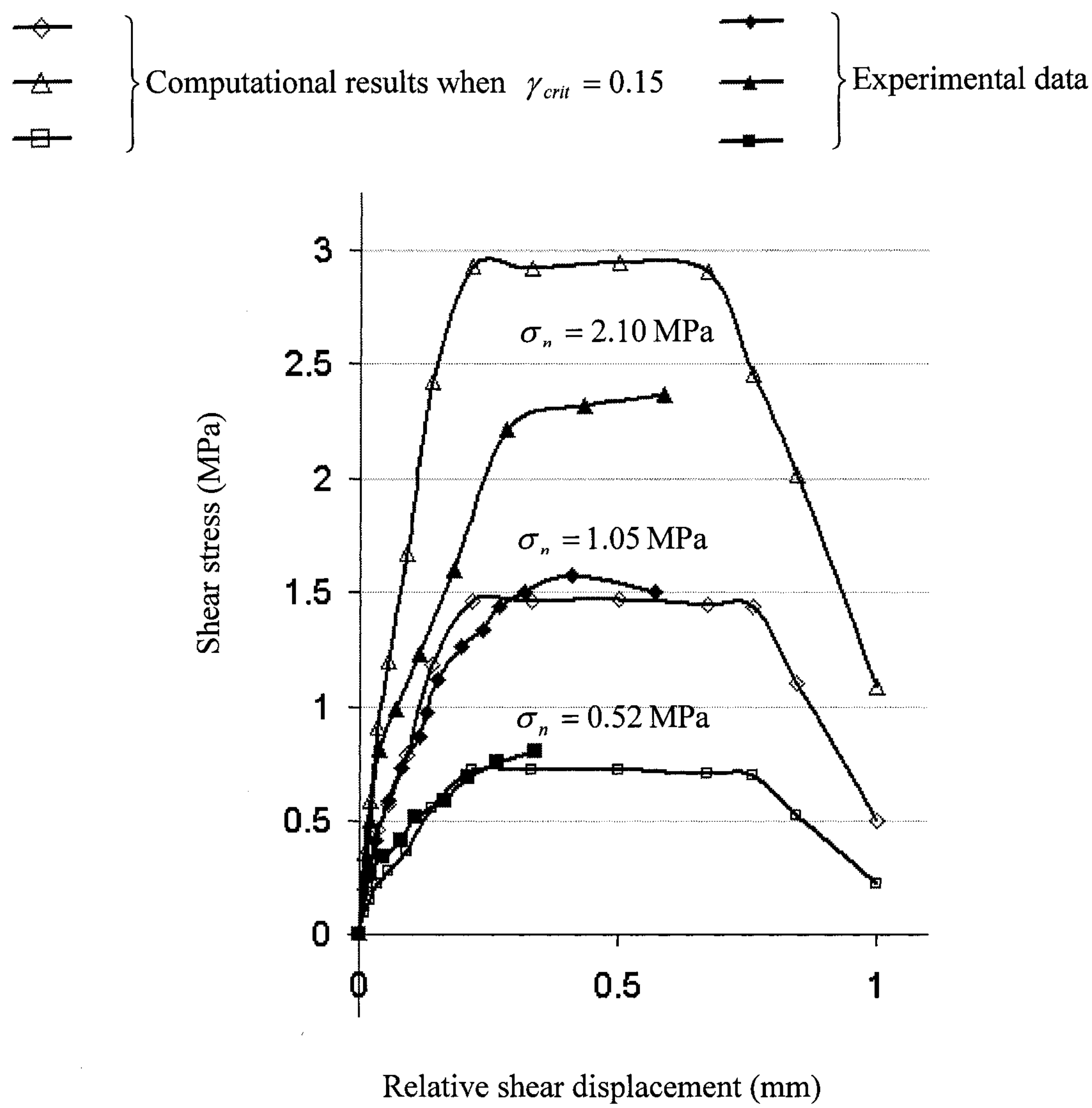

Figure 4.6 Computational simulation of experimental data when $\gamma_{crit} = 0.15$

The computational modelling is also conducted to account for cases involving material plasticity and in the absence of material plasticity. Figure 4.7 shows the results of the two computations. These results indicate that, at least for the unweathered dolerite joint examined here, material plasticity has no significant influence on the shear behavior of the joint. To obtain a better understanding of the shearing process, the Figure 4.11 shows the evolution of plastic zones during shear at normal stress of 2.10MPa with surface interaction properties, $\mu = 0.6745$ and $\gamma_{crit} = 0.15$. Only slight material plasticity is observed. Figure 4.9 and Figure 4.10 give the relative motion between two contacting regions, with corresponding shear stress and dilatancy. The incompatible element accounts for the discontinuous displacement at joint.

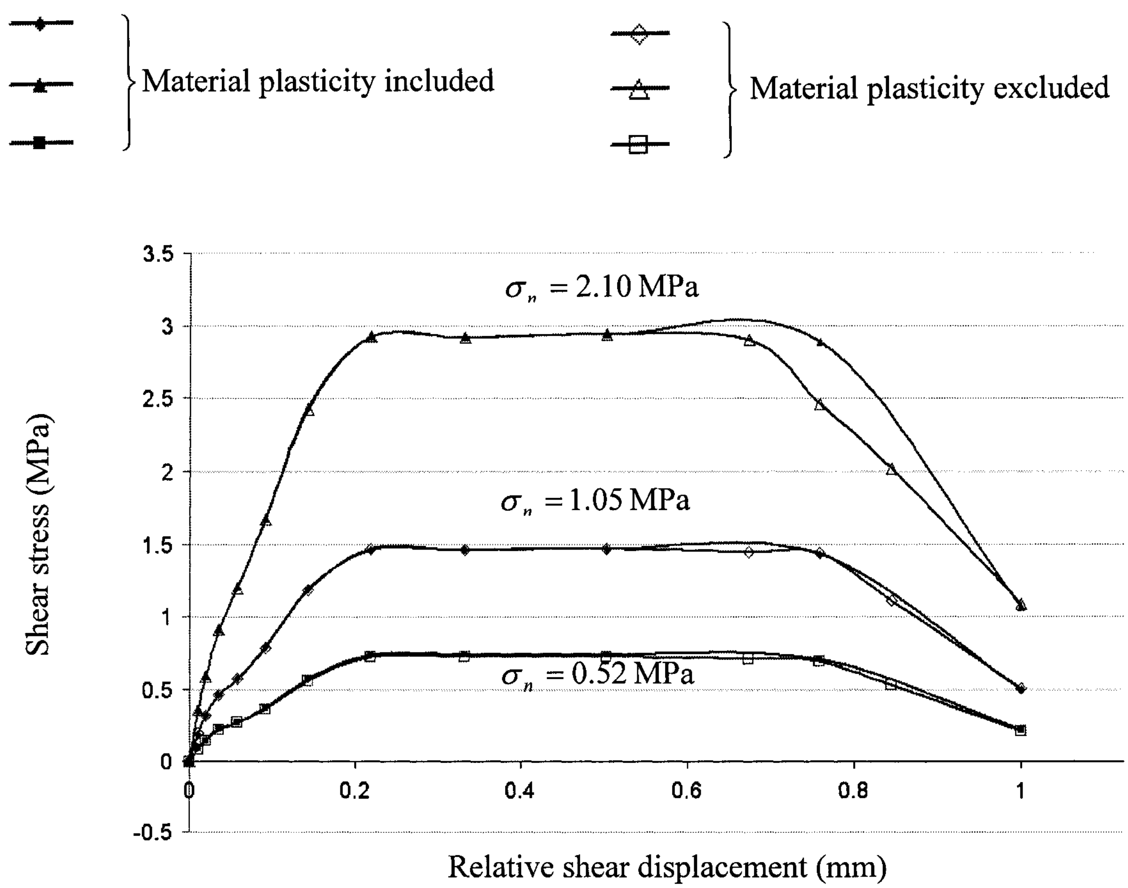

Figure 4.7 Variation of shear stress in the presence and absence of material plasticity

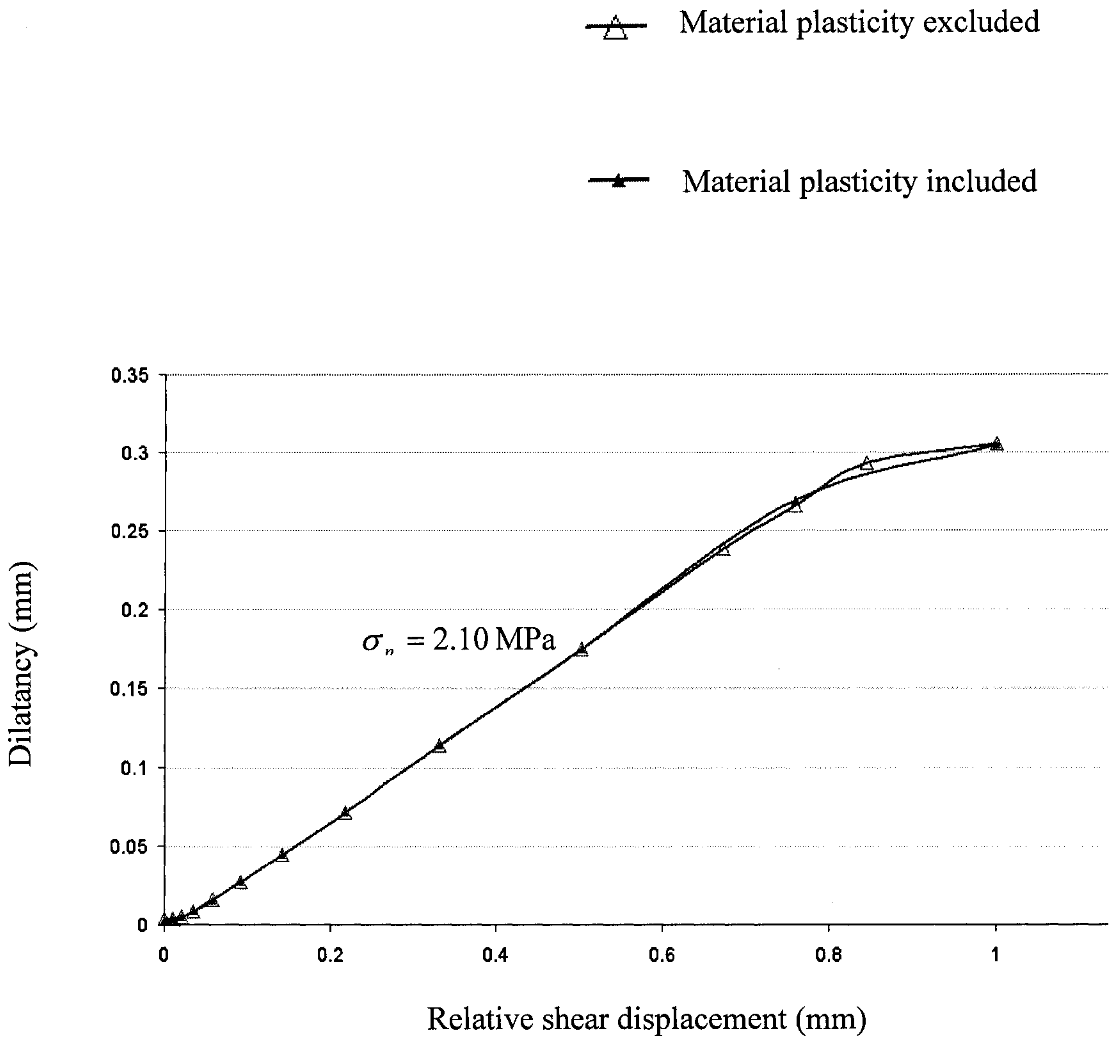

(b). Dilatancy vs. relative shear displacement

Figure 4.8 Variation of dilatancy in the presence and absence of material plasticity

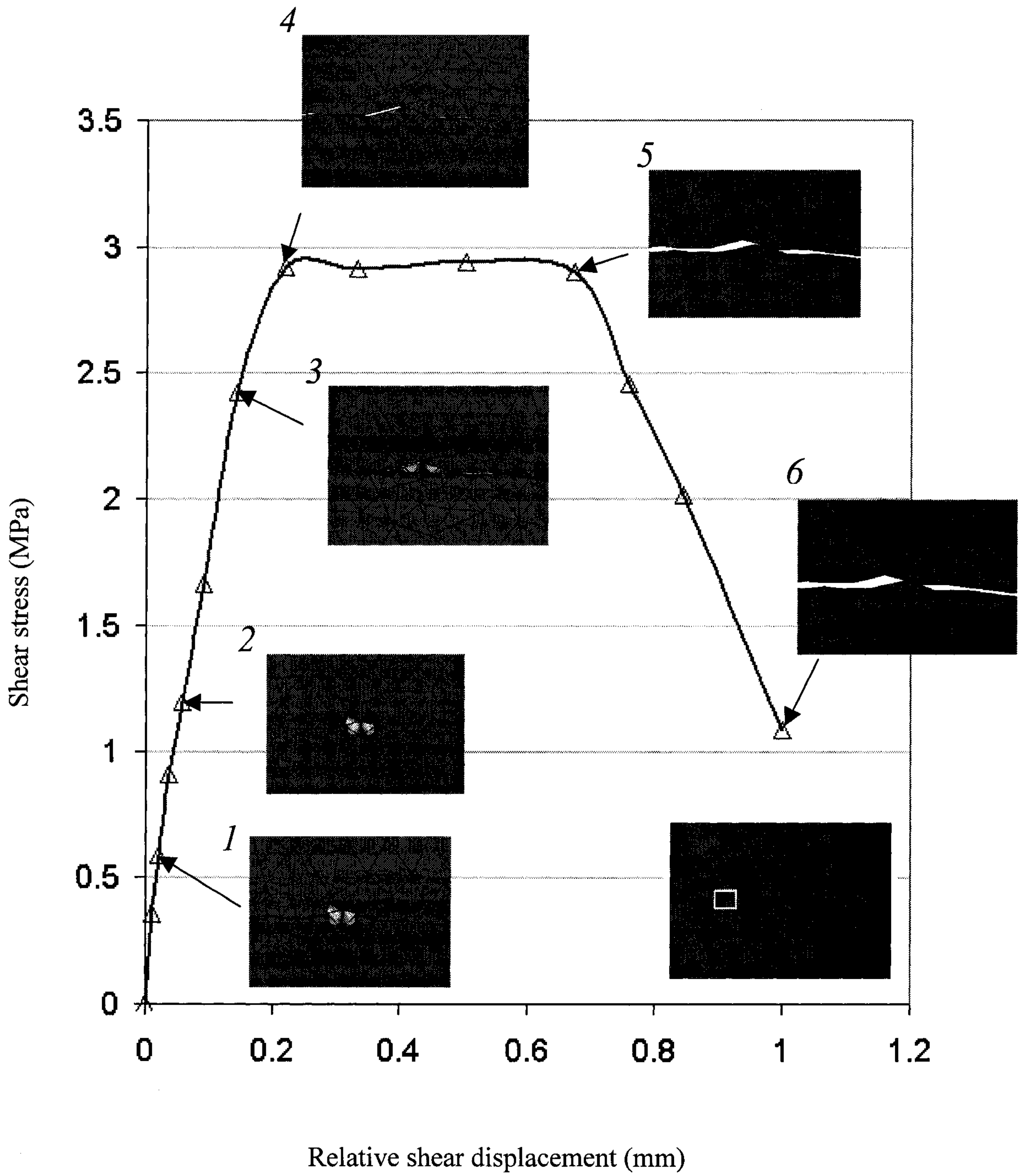

Figure 4.9 Shear stress vs. relative shear displacement for shear at $\sigma_n = 2.10$ MPa, $\mu = 0.6745$

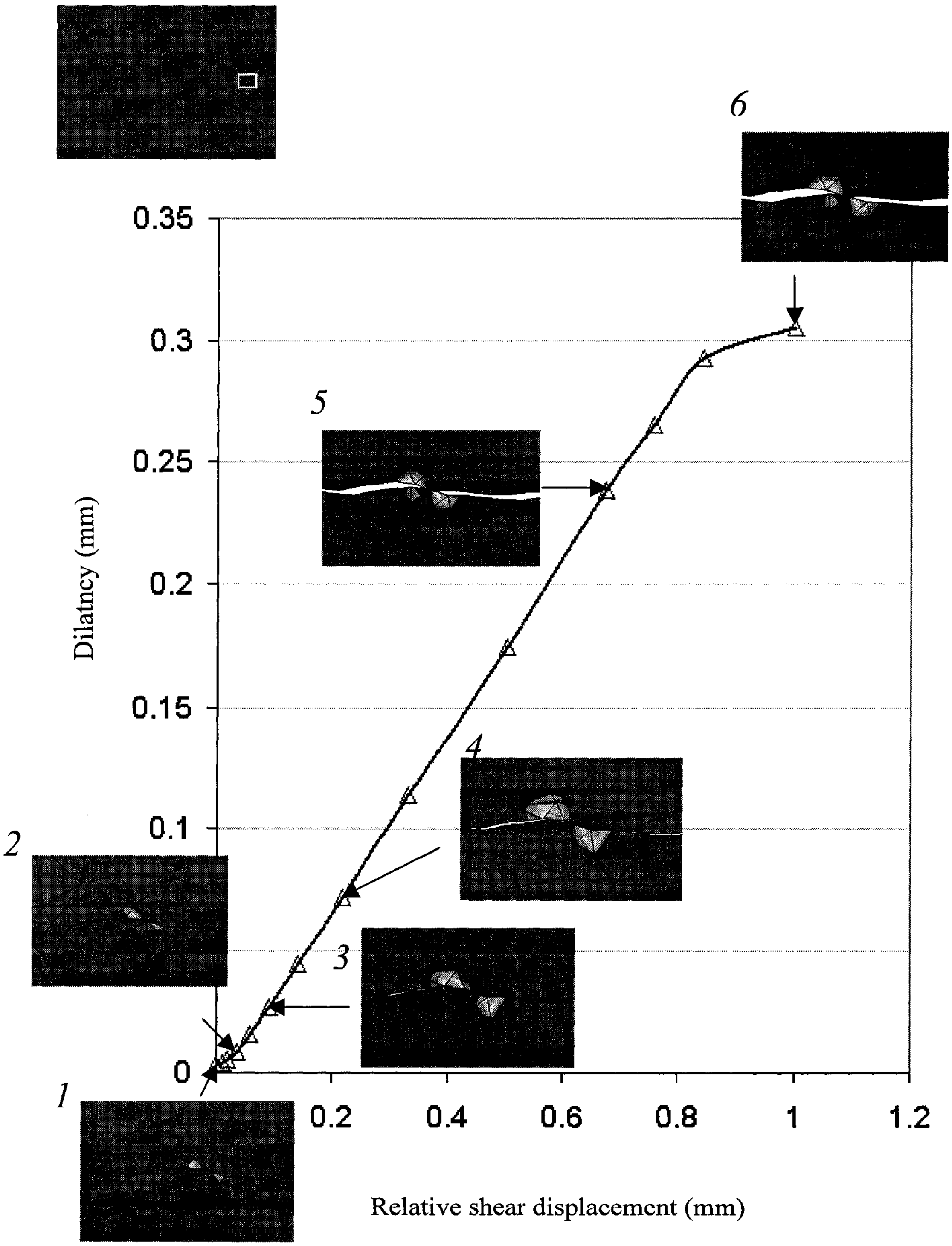

Figure 4.10 Dilatancy vs. relative shear displacement for shear at $\sigma_n = 2.10$ MPa, $\mu = 0.6745$

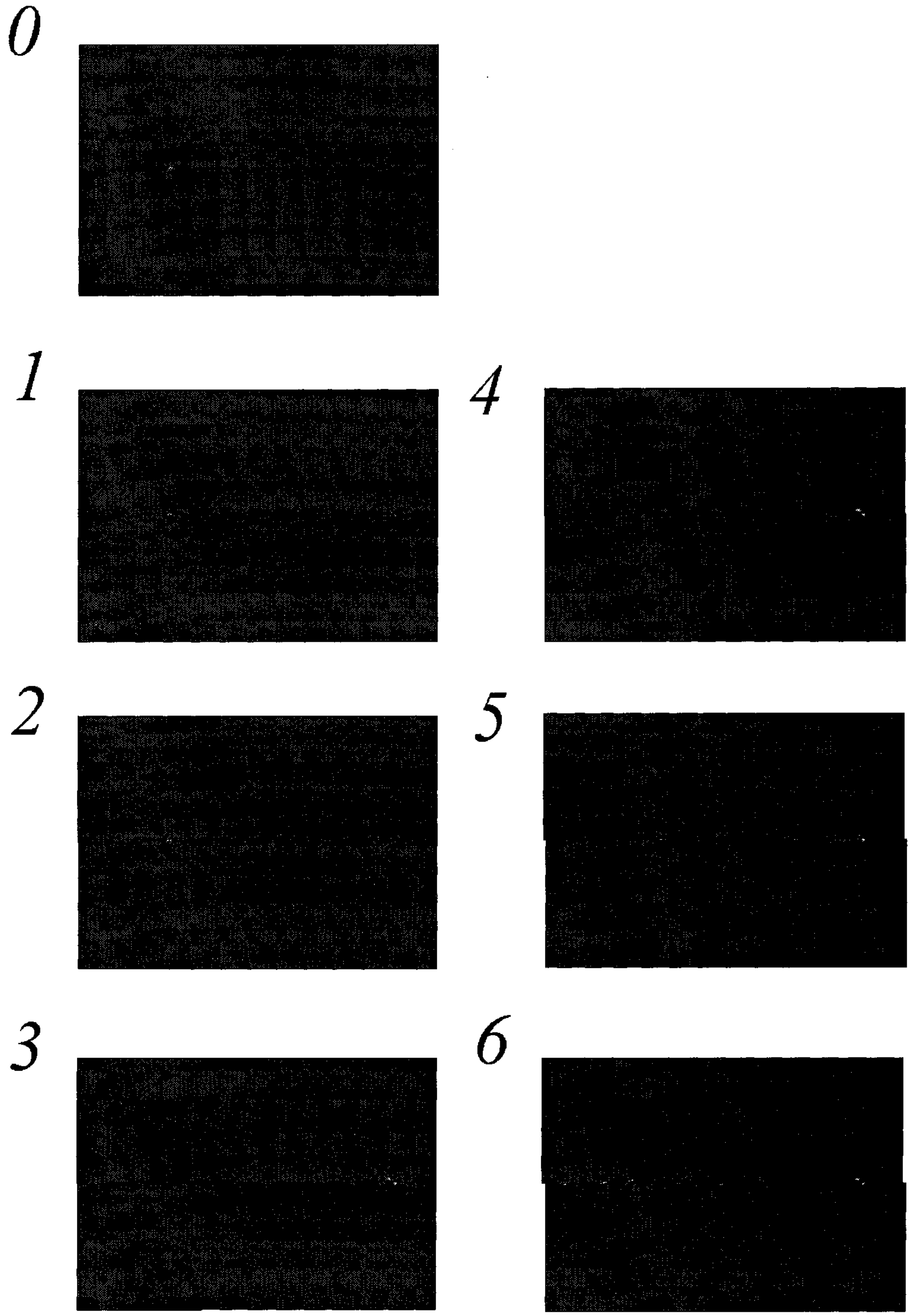

Figure 4.11 Evolution of plastic zones during shear at $\sigma_n = 2.10$ MPa, $\mu = 0.6745$

4.4 Summary

In the computational simulation conducted here, an elastic-plastic model has been used to examine the modelling of the surface interaction between joint surfaces. To obtain an accurate correlation with experimental data, reliable information is necessary, concerning the coefficient of friction μ and the amount of maximum elastic slip γ_{crit} incorporated in the model. The coefficient of friction influences the peak shear stress and the amount of maximum elastic slip influences the shear stiffness of joint.

This chapter has also examined the influence of material plasticity on the shear behavior. The results indicate that, at least for the unweathered dolerite joint examined here, material plasticity has no significant influence on the shear behavior of the joint. This aspect needs further investigations if the computational scheme is applicable to model joints and interfaces encountered in comparatively softer geological media such as sandstone, shale and other sedimentary rocks.

Chapter 5

SHEAR BEHAVIOUR OF DOLERITE JOINTS

In this chapter, we examine in some detail the shear behavior of rock joints for different cases involving the joint profile. The existence of governing asperity on the shear behavior is discussed first, and the shear responses of both irregular and regular joints are compared. The analysis is then extended to the consideration of shear behavior of an idealised triangular joint with steep asperity angles. Other factors, including influence of the boundary contributions, loading cycles, initial separation of joint are also examined. For the purposes of the computational modelling, attention is primarily restricted to the modelling of dolerite rock discussed previously in Chapter 4.

5.1 The existence of governing asperities

Experimental evidence shows that rock joint exhibits different shear behavior at different scales. The reasons for this phenomenon are diverse and sometimes are not completely understood. The computational modelling discussed here is a perliminary attempt to shed some light on how the scale of joint influences its mechanical behavior, we compare the shear behavior of three joint sections at lengths, $100\,\text{mm}$, $50\,\text{mm}$ and $25\,\text{mm}$. The irregular surface profile of $100\,\text{mm}$ length has been examined in detail in Chapter 4. The model of the dolerite joint with this irregular profile was presented in Chapter 4 (Figure 4.1). The application of shear results in the relative movement of the lower section of the test specimen. The maximum relative shear displacement is extended to $2.5\,\text{mm}$, which overrides three elements closest to joint surface. For the purpose of comparison, shear is conducted in both directions. No rotation is allowed in the upper section of the sample during shear. The joint is first subjected to a single cycle of shear commencing from unstressed state. During the application of the shear, the joint is subjected to a constant normal stress of either $3\,\text{MPa}$ or $11\,\text{MPa}$. The material properties for the dolerite required in the computational modelling are given in equation (4.1). As shown in Figure 5.1, the other two profiles are two subsets of this $100\,\text{mm}$ profile.

In all three simulations, the coefficient of friction between the joint surfaces is specified at the value $\mu = 0.6745$, which is given by Barton and Bandis (1983). The maximum elastic slip is back-calculated as $\gamma_{crit} = 0.15$ (see Chapter 4). When considering three joint sections, initially, compatible contacts are maintained over the entire lengths of the profiles.

We can deduce that, when the specimen is not allowed to rotate, contact occurs only at a limited number of points during shear of an irregular profile. In all three computational models, contacting during shear, either in the "forward" or the "reverse" direction, occurs only at one asperity, which is indicated in Figure 5.1 and Figure 5.2 as "*governing asperity*". The "*governing asperity*" usually has the largest asperity slope. The mechanical behavior of interface of other surface sections therefore has negligible effect on the shear behavior of the whole rock joint. Dilatancy appears to follow along the surface geometry of this "*governing asperity*" during shear for different lengths. The shear stress-relative shear displacement and dilatancy-relative shear displacement relationships do not vary significantly in the three different cases, either in "forward" or "reverse" direction. The dominant asperity therefore governs the shear behavior of the entire profile. Therefore, when rotation is excluded, the shear behavior of smaller section of joint surface including this "*governing asperity*" then appears to give a representative response applicable to larger sections of the profile.

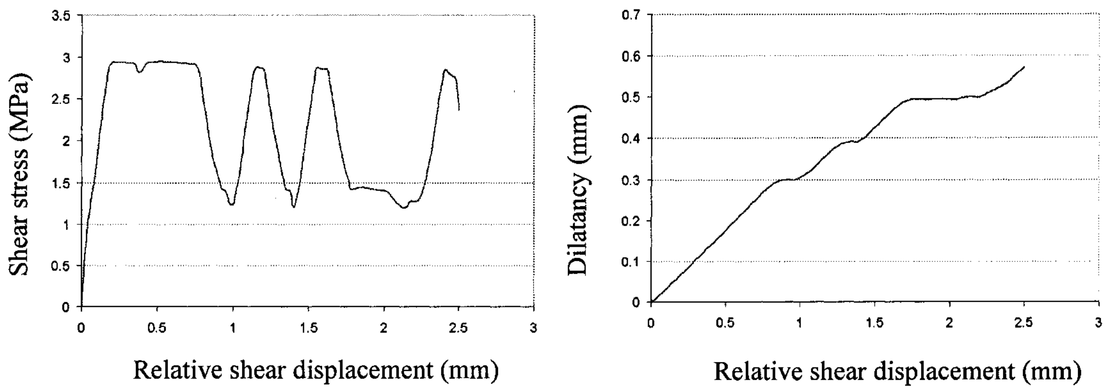

(a) Section 0-0

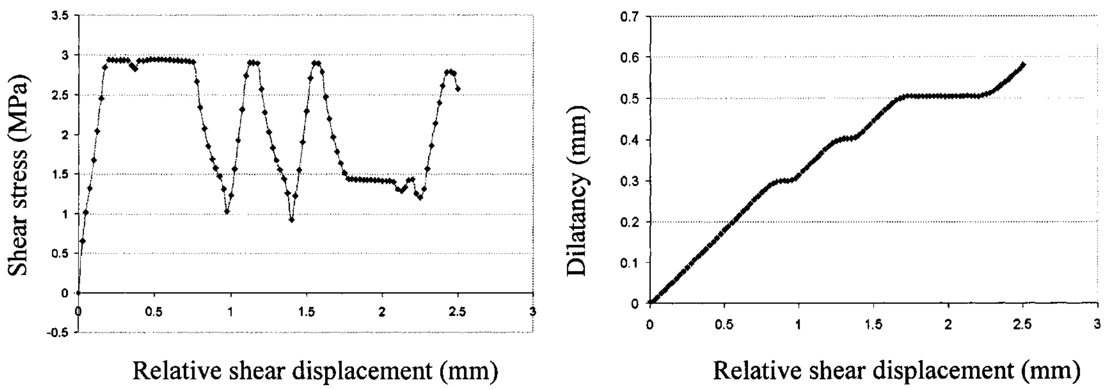

(b) Section 1-1

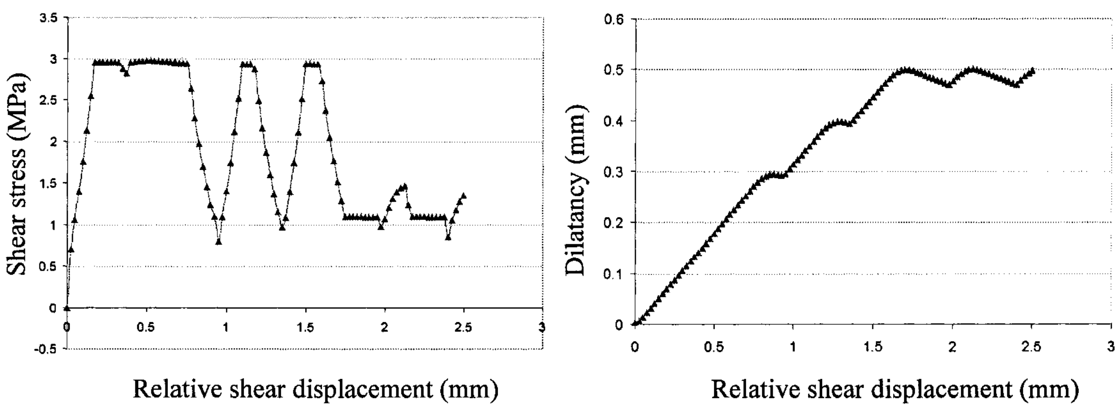

(c) Section 2-2

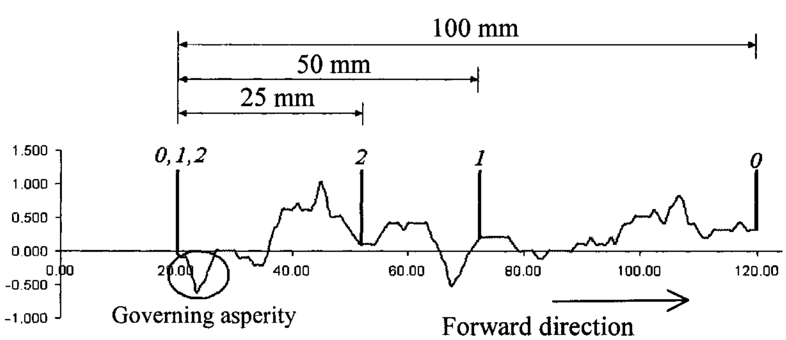

Figure 5.1 Shear behavior of dolerite joint at different lengths in the absence of rotation

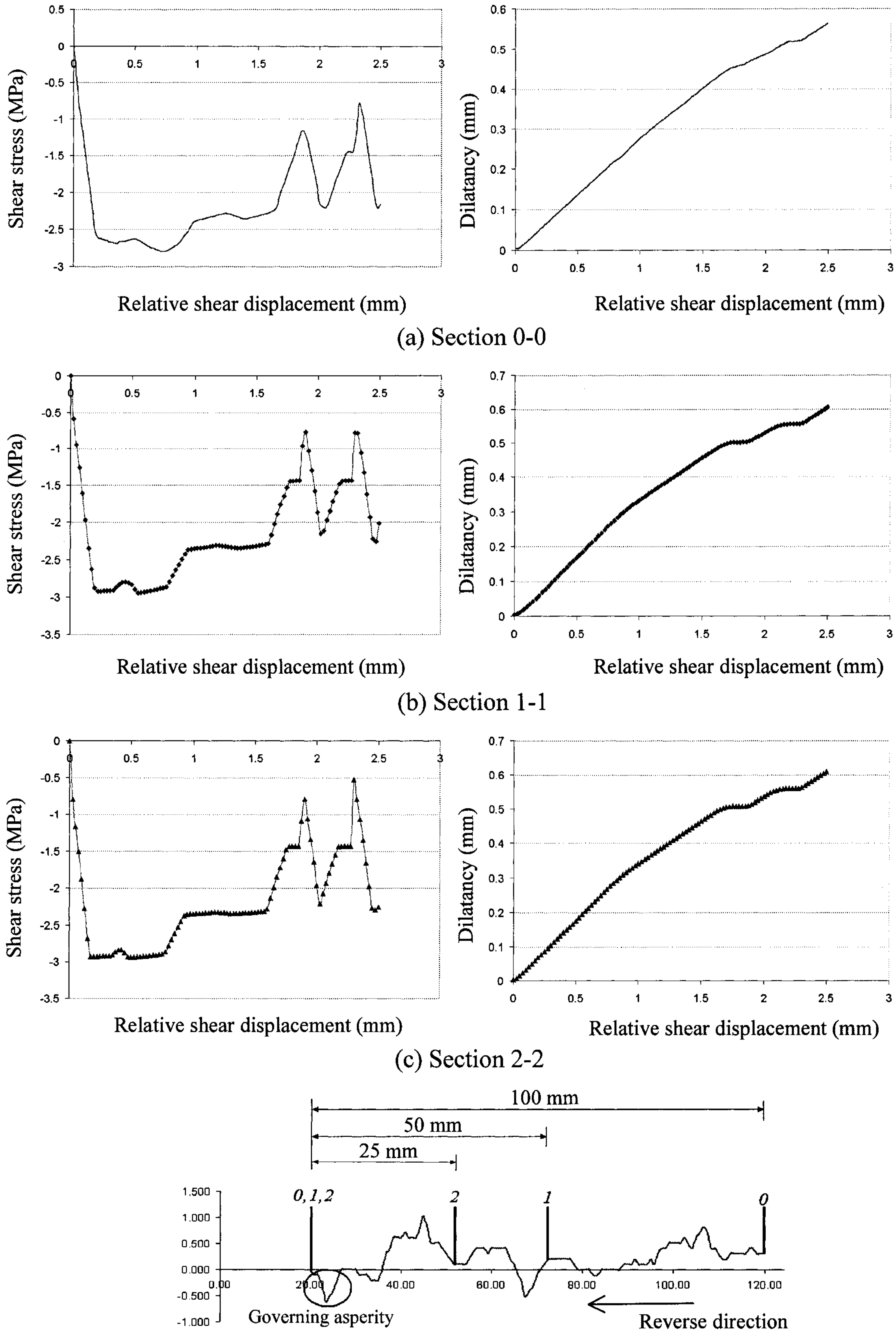

Figure 5.2 Shear behavior of dolerite joint at different lengths in the absence of rotation

5.2 Shear behavior of joints with differing surface profiles

In the second model we present the results of computational modelling conducted on joints with three types of surface profiles. Attention, however, is restricted to the two-dimensional representation of a joint. The first has a natural irregular profile discussed in Chapter 4; the second is a simplification of the joint, which disregards the small roughness, but has the same peak asperity height; the third is a regular profile, which has a different asperity height, but roughly has the same dilatancy angle. The consideration of regular joint is based on Patton's assumption, which states that an irregular joint can be idealized into a regular one exhibiting the same peak response of shear stress if both joints exhibit the same dilatancy angle. The regular joint is also referred as "Patton's joint" in this section. Shear on the irregular joint under small normal stress discussed in Chapter 4 roughly exhibited a dilatancy angle of 20°. This dilatancy angle has been chosen as the asperity angle for the regular joint. Also this value is found to be roughly equal to the asperity angle of the "*governing asperity*" discussed in section 5.1. The configurations of three joint profiles are presented in Figure 5.3(c). The single cycle shear tests are conducted under normal stresses of $3\,\mathrm{MPa}$ and $11\,\mathrm{MPa}$, which simulates an in situ stress corresponding to a depth of about 100 m and 350 m depth, respectively. The objective of the study is to examine the influences of factors such as the joint profile, normal stress, the dilatancy angle and material plasticity on the performance of the joint.

The computational model for the irregular joint is identical to that discussed in Chapter 4. For the purpose of comparison, results are also presented for two other joint profiles, namely, the simplified joint and Patton's joint model. The surface interaction properties including friction behavior and elastic slip amount are assigned the same value as those discussed in section 5.1. When considering three joint sections, initially, compatible contacts are maintained over the entire profile. The finite element discretizations are shown in Figure 5.4.

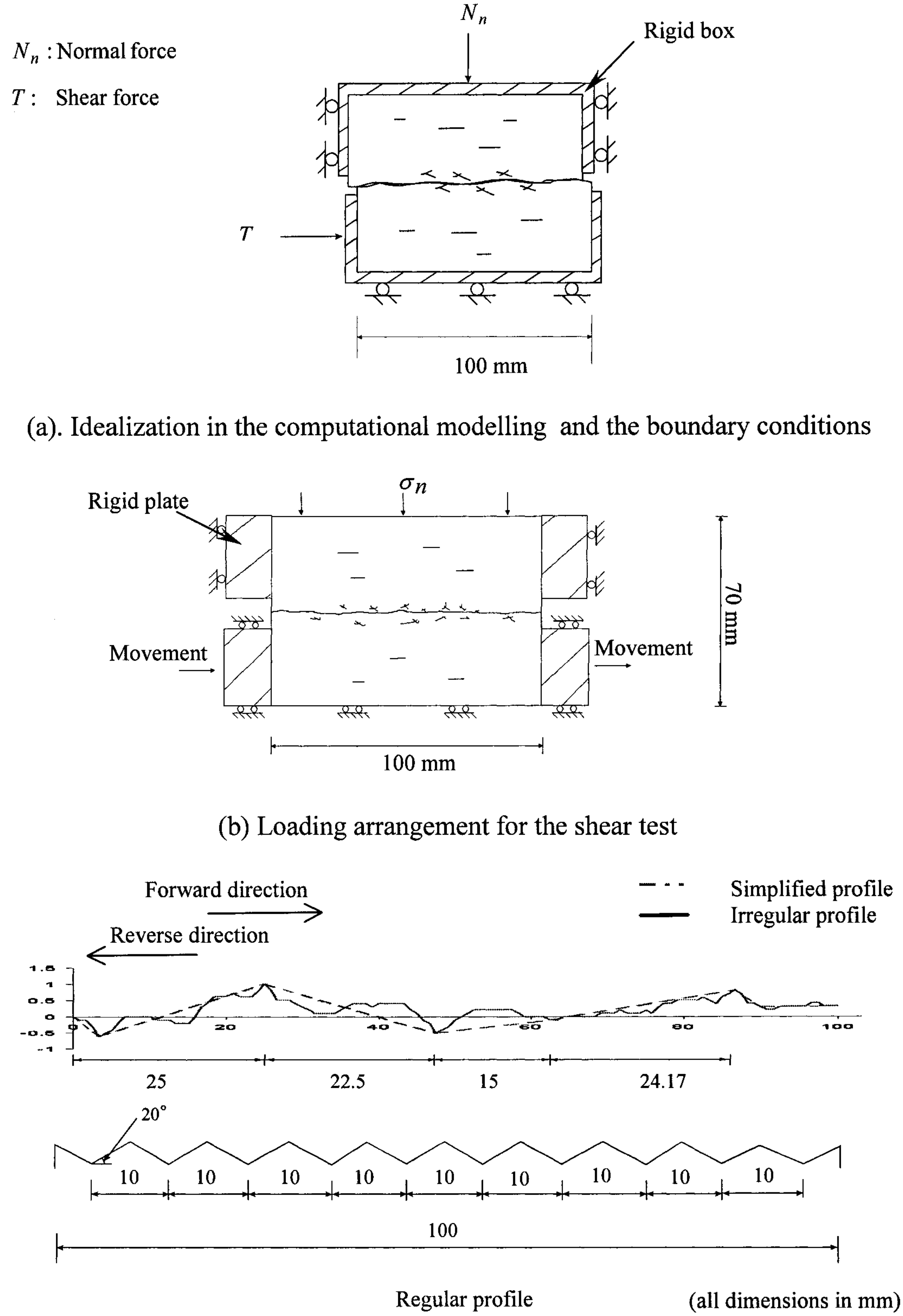

(a). Idealization in the computational modelling and the boundary conditions

(b) Loading arrangement for the shear test

(c). 2D joint surface profiles (after discretization)

Figure 5.3 Shearing of a dolerite joint with different surface profiles

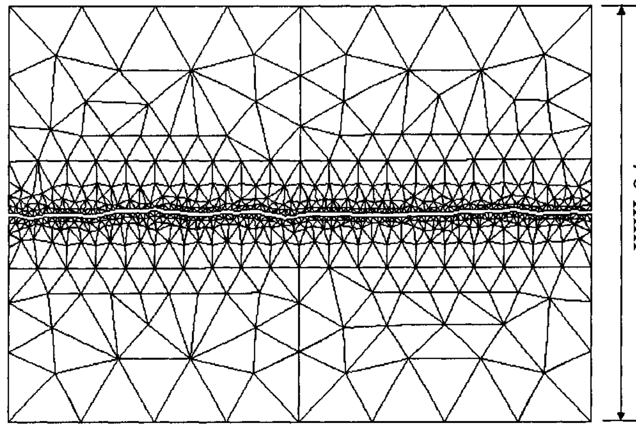

(a) Irregular joint (initially compatible mesh, 1194 elements and 2673 nodes)

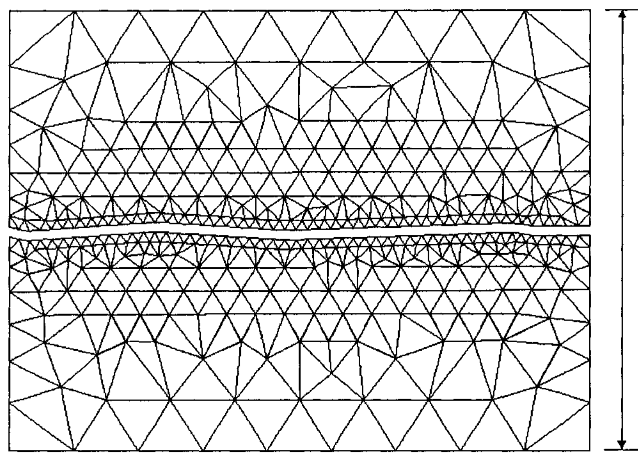

(b) Simplified joint (initially compatible mesh, 726 elements and 1600 nodes)

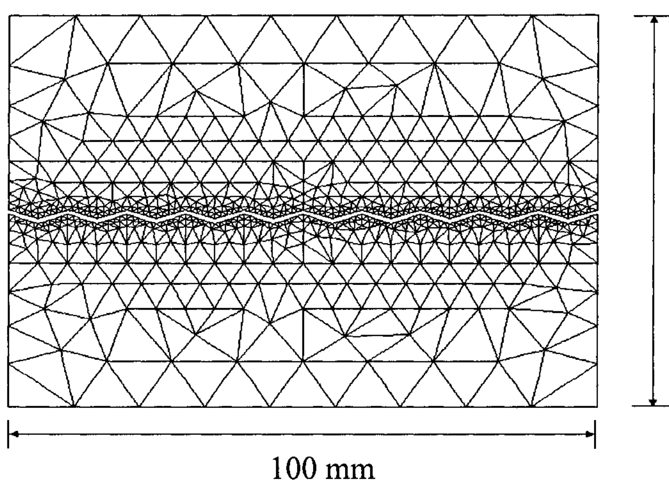

(c) Patton's joint (initially compatible mesh, 1026 elements and 2238 nodes)

Figure 5.4 Finite element discretizations of a joint with three profiles

When comparing the shear responses of irregular and regular joints, the computations indicate that the omission of the local profile of the joint or the joint roughness greatly reduces the dilatancy and peak shear stress during shear. In comparison with the irregular joint, the shear behavior of the simplified joint largely underestimates both dilatancy and peak shear stress. As shown in Figure 5.5(a) and Figure 5.6(a), these discrepancies are noticeable at normal stress levels of 3 MPa. At the same stress level, the energy dissipation due to plastic flow in parent material (Figure 5.7) appears to be two orders of magnitude smaller than the frictional energy dissipation (Figure 5.8). The material region adjacent to the joint surfaces experiences the largest plastic energy dissipation during loading process; when contacting surfaces experience separation and slip, with respect to each other, shear stress is almost constant and plastic deformations do not increase significantly; during the unloading process, asperities generally response elastically and no increase in plastic energy dissipation is observed. The irregular joint experiences a larger plastic energy dissipation under normal stress 11 MPa (Figure 5.7 and Figure 5.9). The omission of the local profile or roughness significantly underestimates the plastic energy dissipation during shear. The plastic energy dissipation in the material region of the simplified joint, which neglects contribution from small asperities, is much smaller (Figure 5.7 and Figure 5.10). In presence of the frictional forces, the frictional dissipation occurs when two contacting surfaces move respect to each other. Disregarding roughness does not neglect noticeable information of frictional dissipation. The frictional dissipation for these two joints exhibits similar trends at both normal stress levels of 3 MPa and 11 MPa (Figure 5.8).

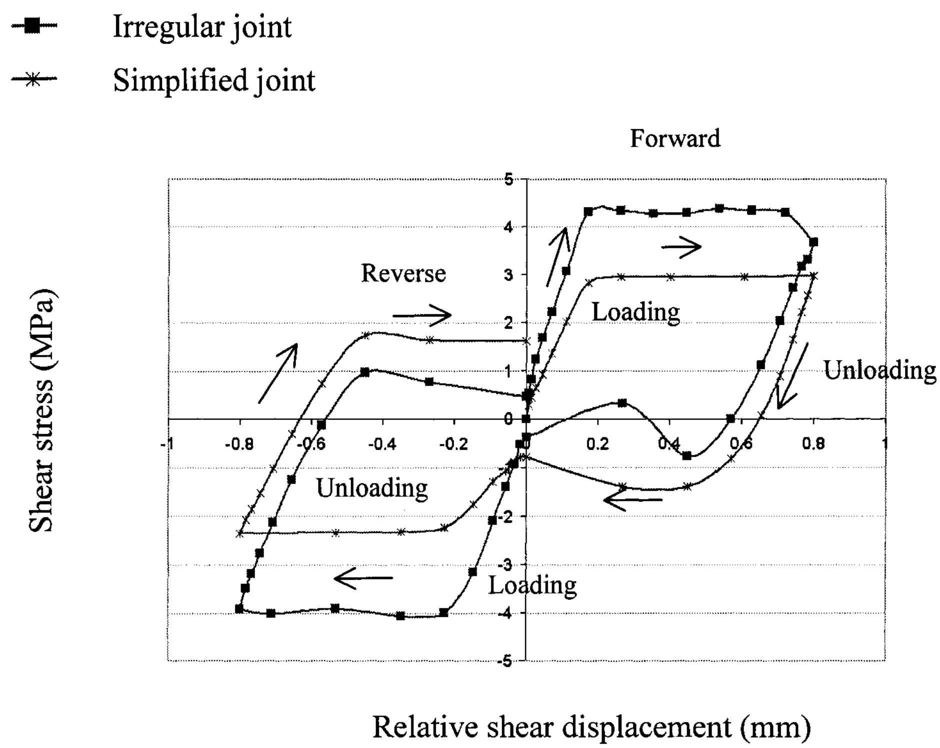

(a). $\sigma_n = 3$ MPa

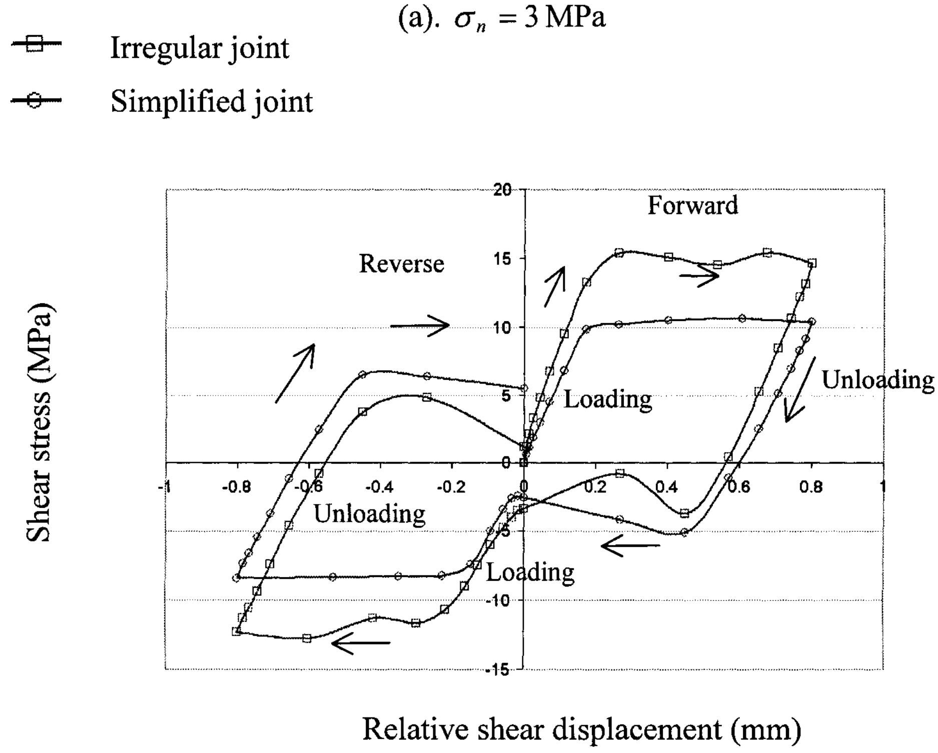

(b). $\sigma_n = 11$ MPa

Figure 5.5 Shear stress vs. relative shear displacement during shear on irregular and simplified joints

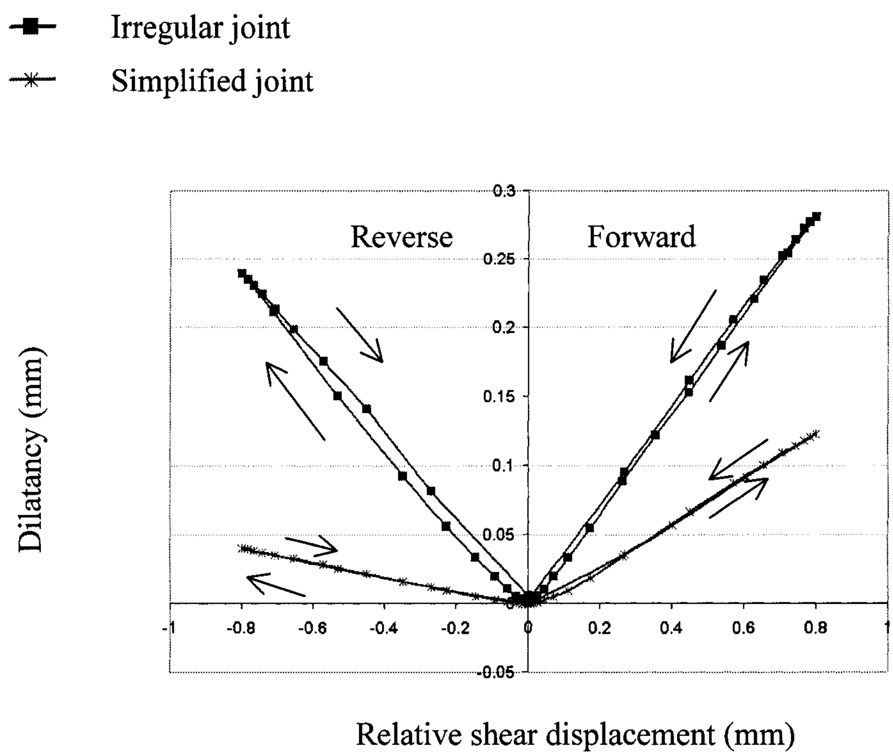

(a). $\sigma_n = 3$ MPa

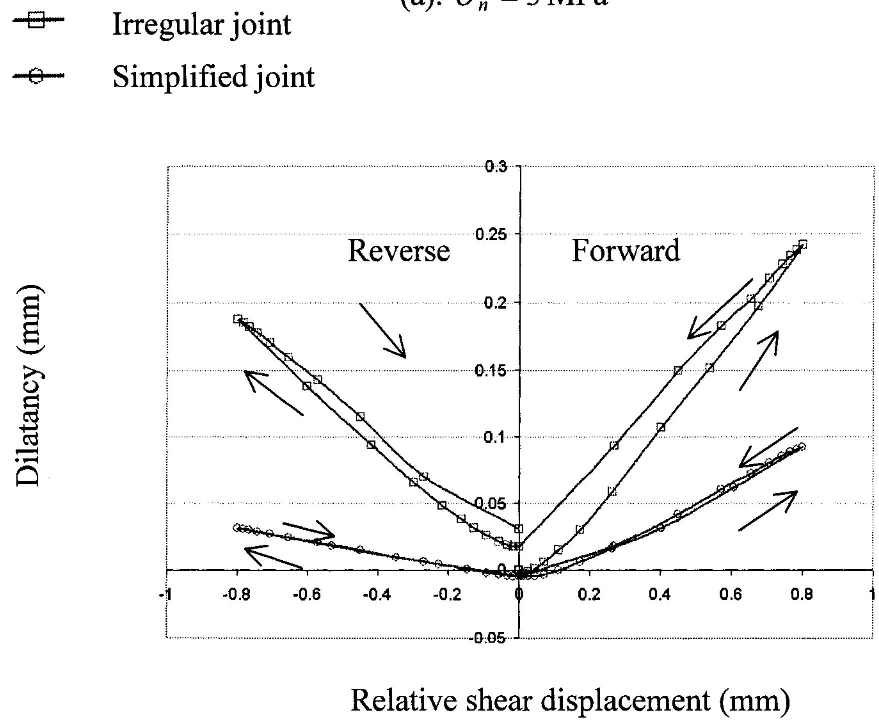

(b). $\sigma_n = 11$ MPa

Figure 5.6 Dilatancy vs. relative shear displacement during shear on irregular and simplified joints

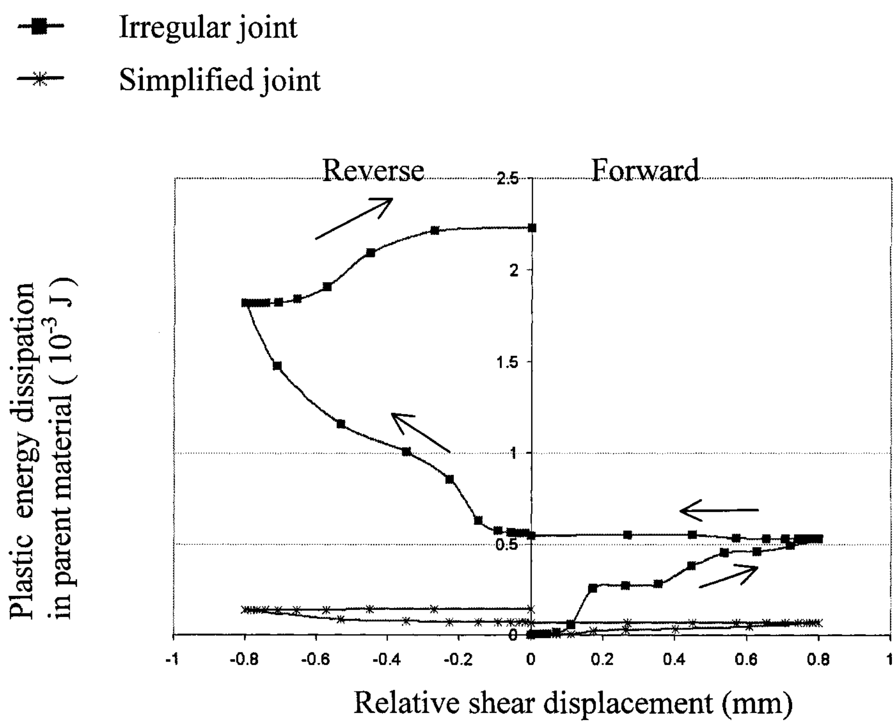

(a). $\sigma_n = 3$ MPa

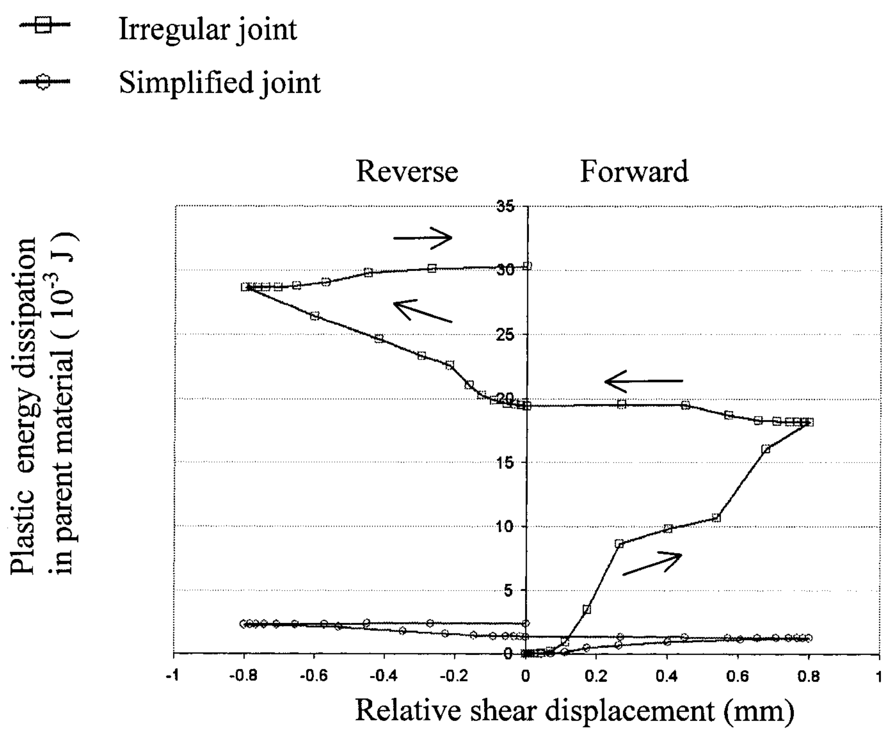

(b). $\sigma_n = 11$ MPa

Figure 5.7 Plastic energy dissipation in parent material vs. relative shear displacement during shear on irregular and simplified joints

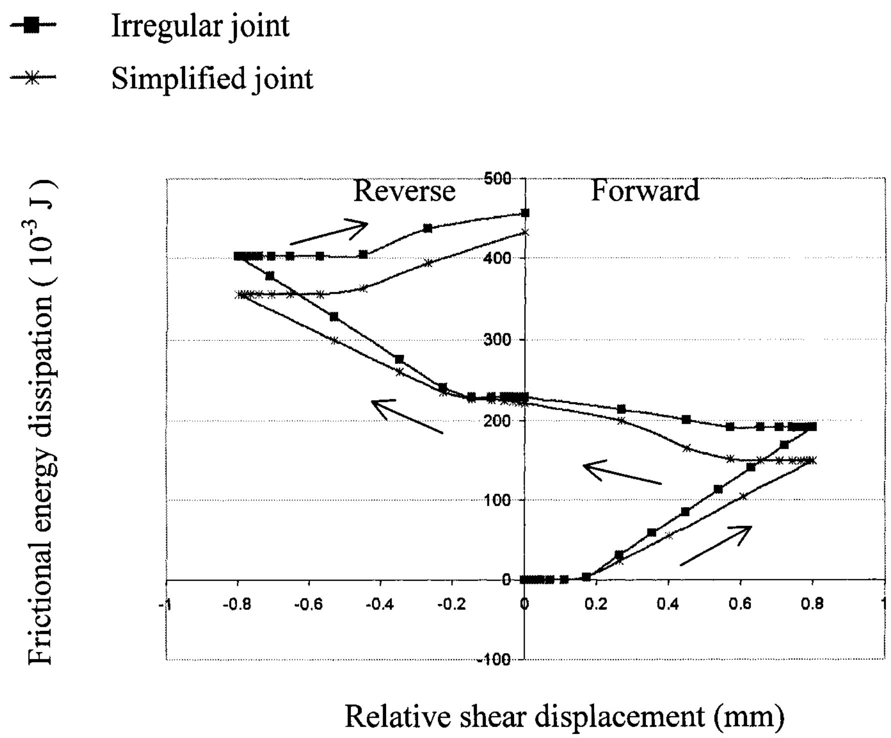

(a). $\sigma_n = 3\,\text{MPa}$

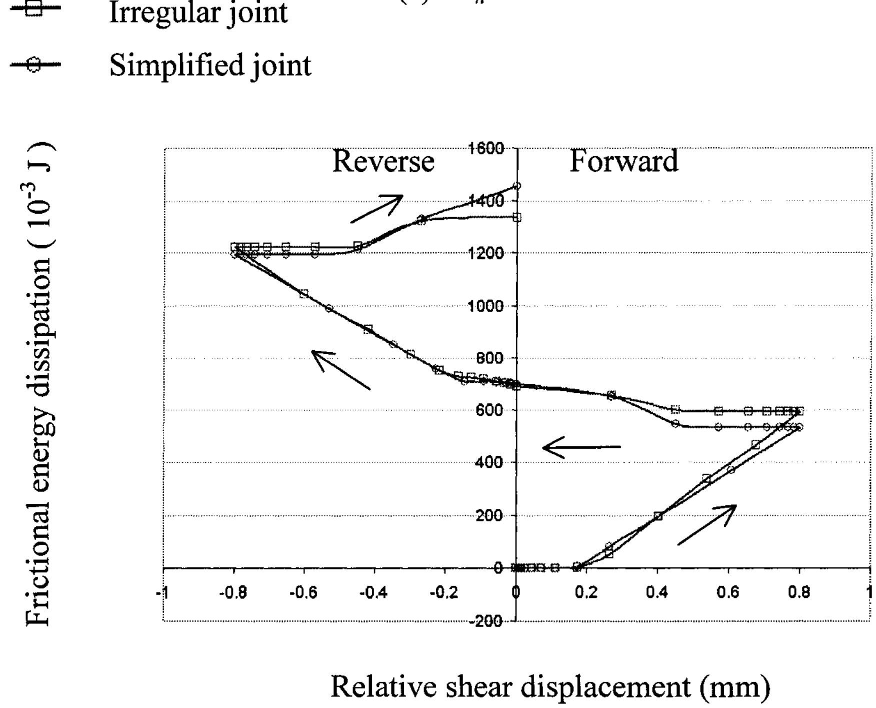

(b). $\sigma_n = 11\,\text{MPa}$

Figure 5.8 Frictional energy dissipation vs. relative shear displacement during shear on irregular and simplified joints

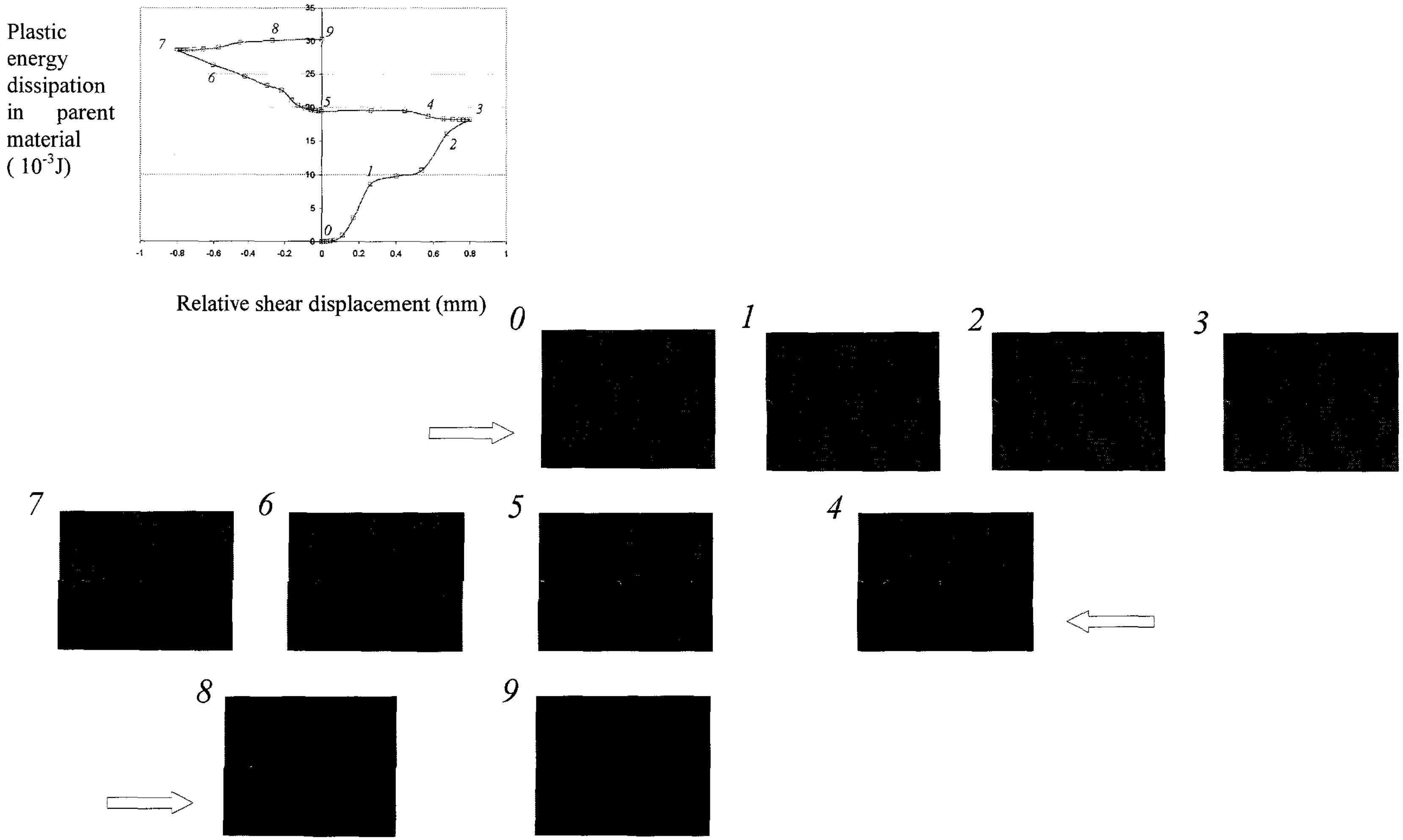

Figure 5.9 Evolution of plastic zones during relative shear of the irregular joint under constant normal stress 11 MPa

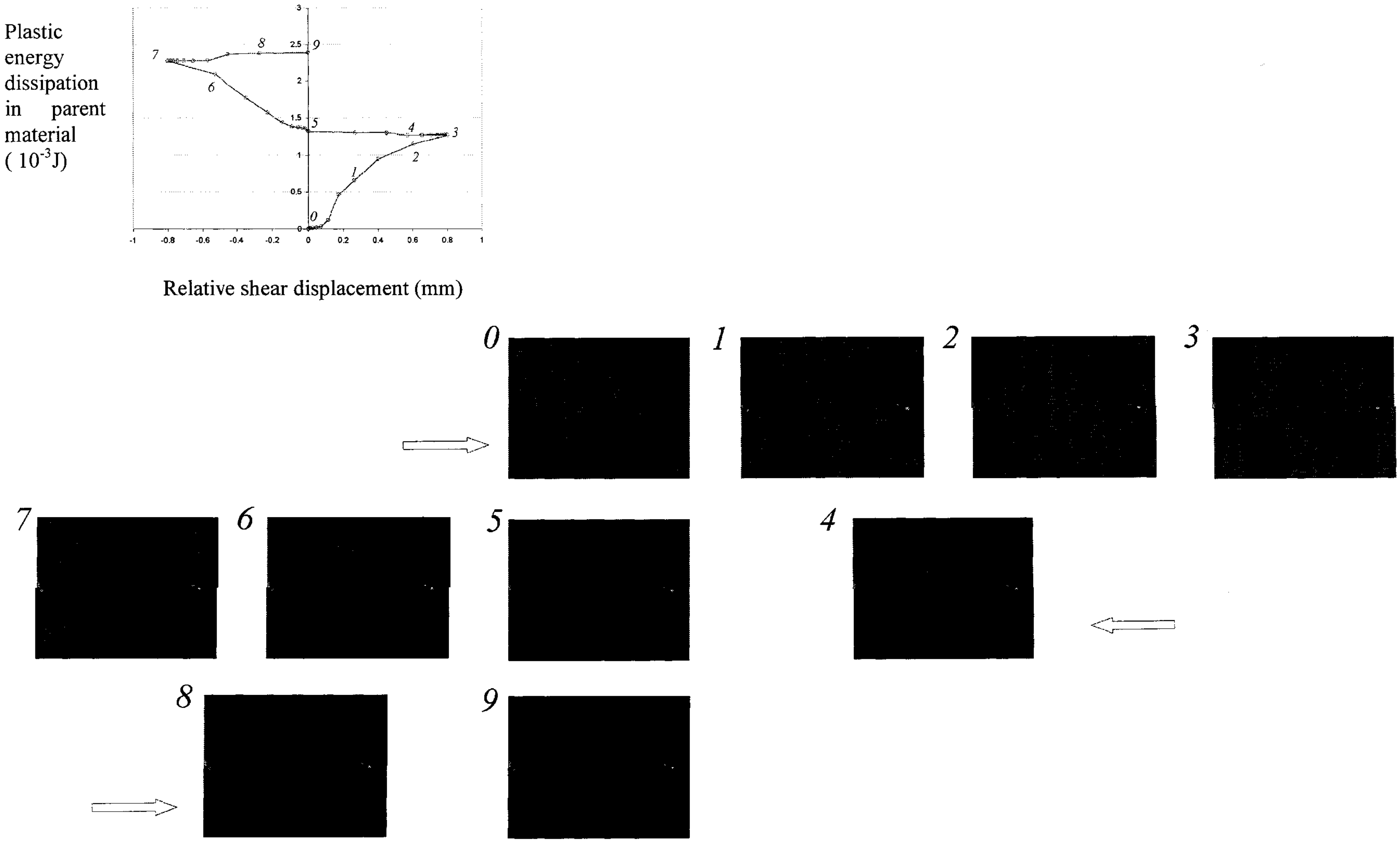

Figure 5.10 Evolution of plastic zones during relative shear of the simplified joint under constant normal stress 11MPa

The variation of dilatancy during shear of "Patton's joint", also, follows a response close to that obtained for the irregular joint at normal stress 3 MPa (Figure 5.12(a). Also partially due to this factor, the regular and irregular joints exhibit similarity of response in the shear stress [Figure 5.11(a)]. This justifies the assumption that, in addition to the peak shear stress, which should be equal according to Patton's model, the variation of shear stress with shear displacement can also be represented by a regular joint if the irregular joint is idealized into a 'saw-tooth' triangular joint by an appropriate method. The results for the higher normal stress of 11 MPa follows a similar pattern. By observations of the surface profile of the irregular joint, it is found that the slope of the "*governing asperity*" discussed in last section has a value close to the asperity angle in Patton's joint model. This points to a way to predict the peak shear stress of a natural irregular joint by identifying the "*governing asperity*" and its "slope". As shown in Figure 5.13, the regular joint model, however, neglects much of the plastic energy dissipation during shear; but it does not exhibit a significant difference in frictional dissipation when compared with results for the irregular joint, shown in Figure 5.14. In comparison to the simplified joint, this difference is, however, still appreciable. This might be due to the fact that the contacting area between two simplified surfaces is more close to that during shear of the irregular joint and that it is the normal stress and contacting area that determines the frictional dissipation during shear.

Roughness therefore, is observed to have greater influence on the plastic energy dissipation whereas the surface geometry of the "*governing asperity*" is more related to dilatancy. The slope of this "*governing asperity*" therefore determines the peak shear stress.

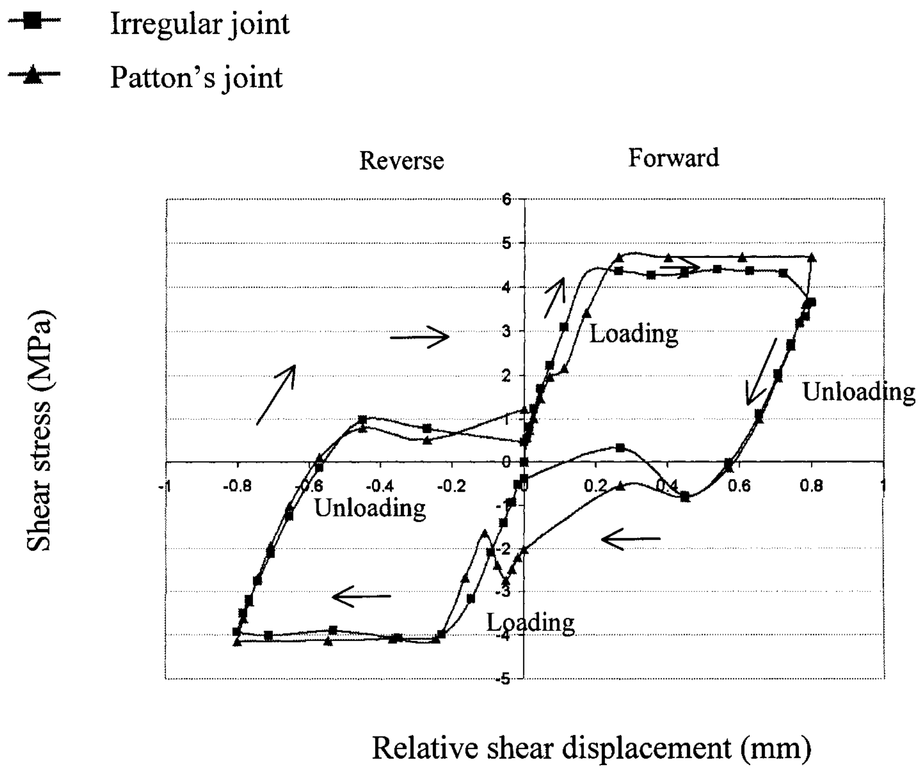

(a). $\sigma_n = 3$ MPa

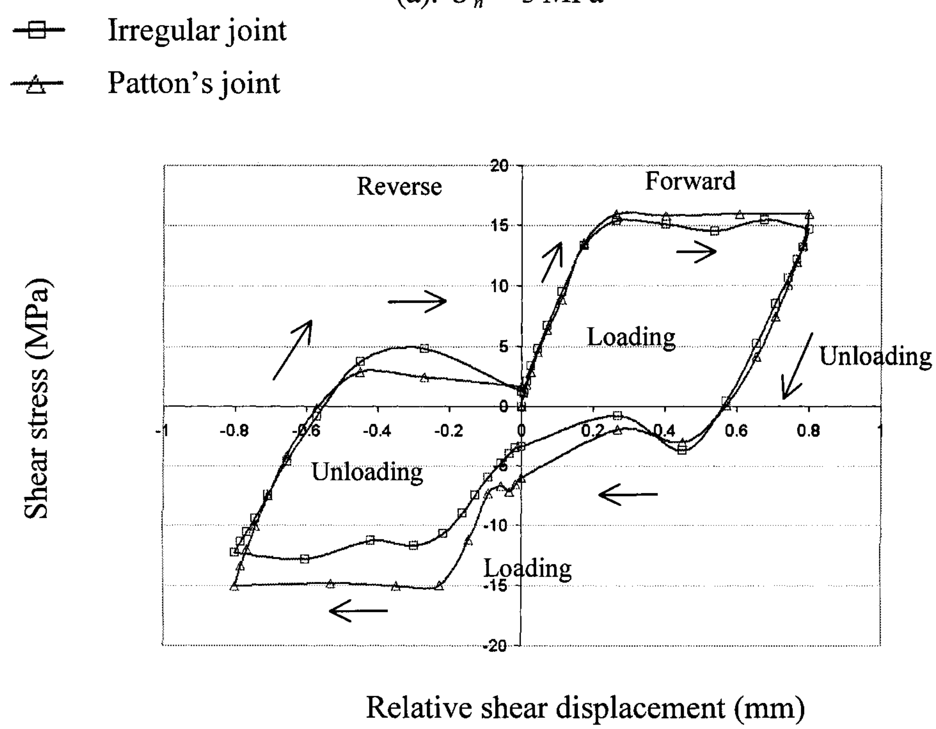

(b). $\sigma_n = 11$ MPa

Figure 5.11 Shear stress vs. relative shear displacement during relative shear of irregular and regular joints

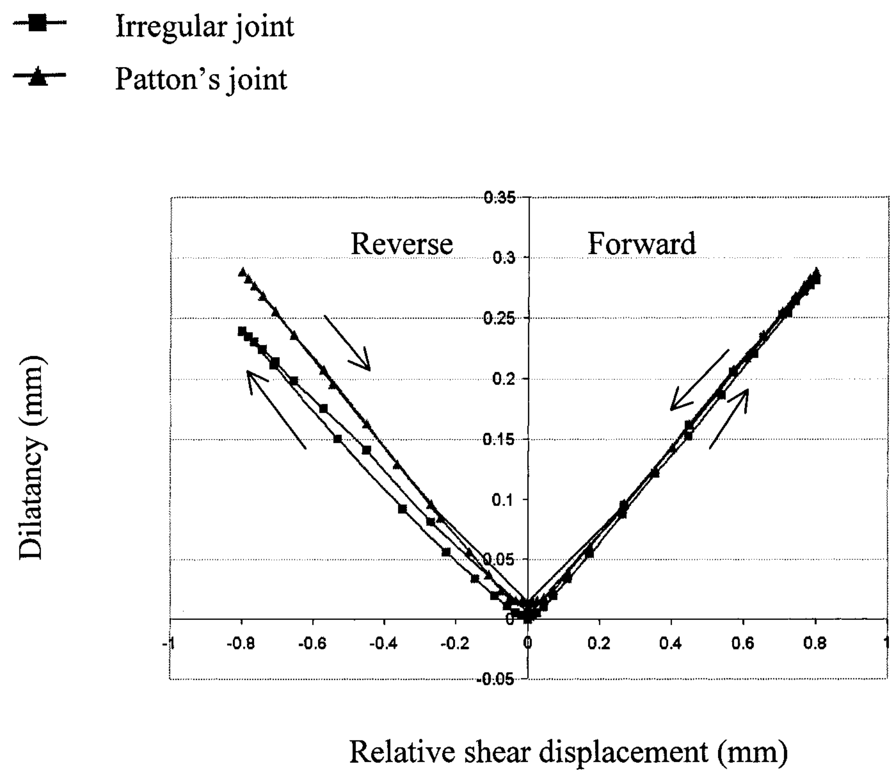

(a). $\sigma_n = 3$ MPa

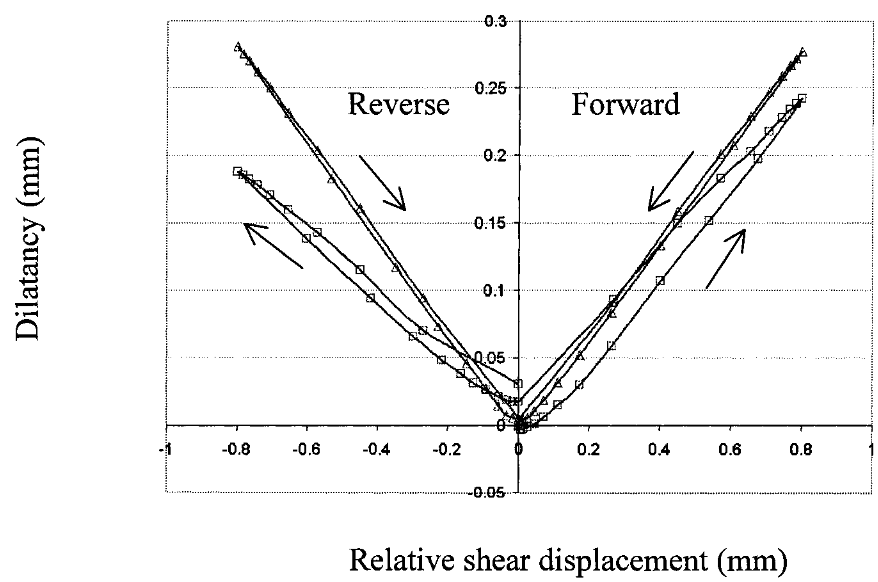

(b). $\sigma_n = 11$ MPa

Figure 5.12 Dilatancy vs. relative shear displacement during relative shear of irregular and regular joints

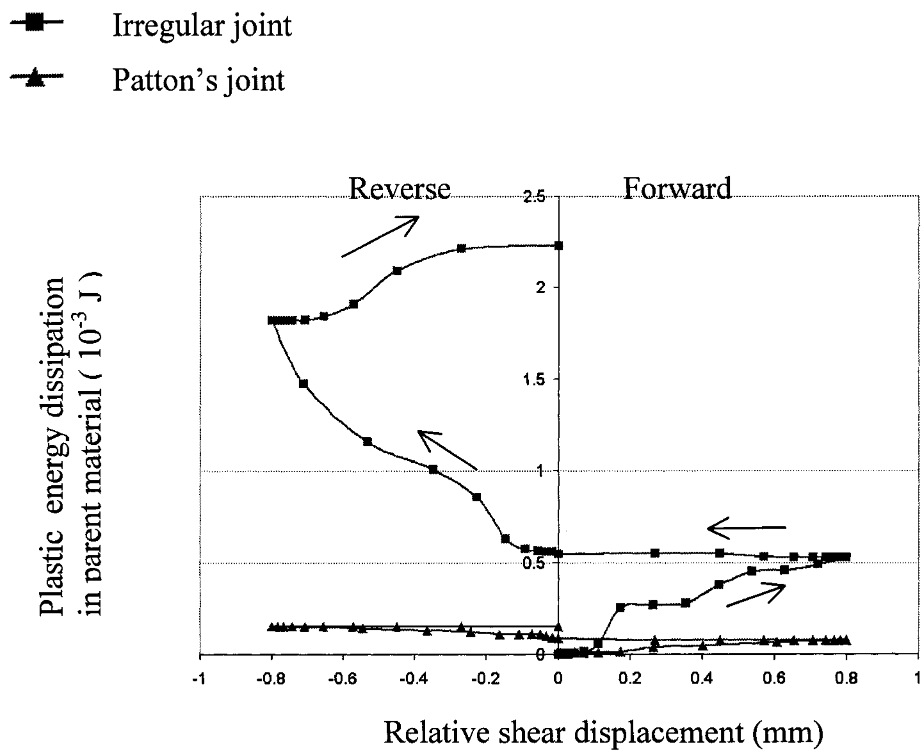

(a). $\sigma_n = 3\,\text{MPa}$

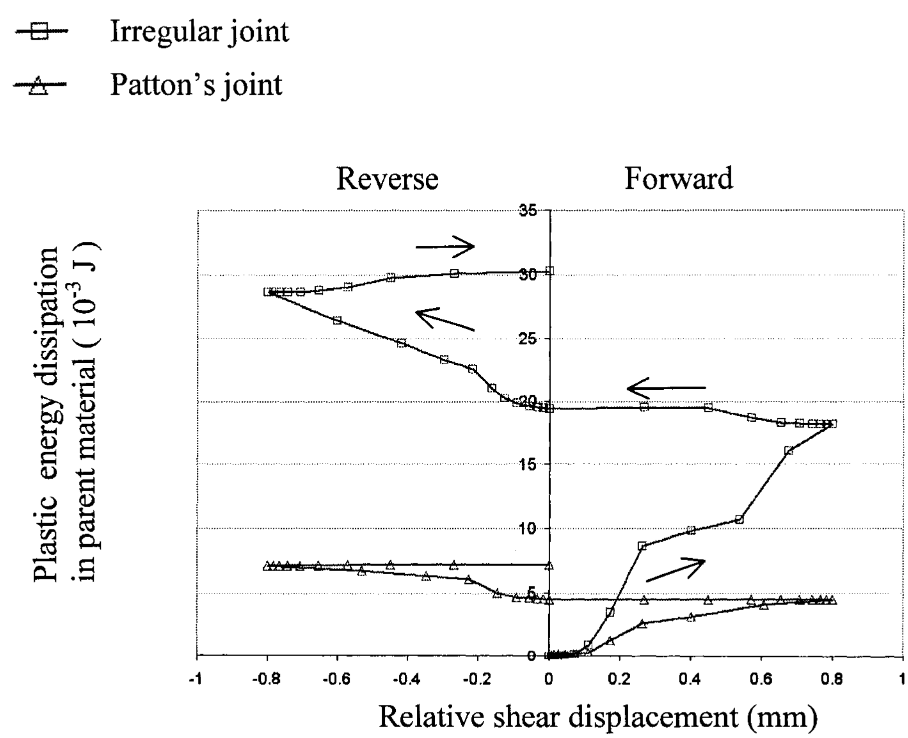

(b). $\sigma_n = 11\,\text{MPa}$

Figure 5.13 Plastic energy dissipation in material vs. relative shear displacement during relative shear of regular and irregular joints

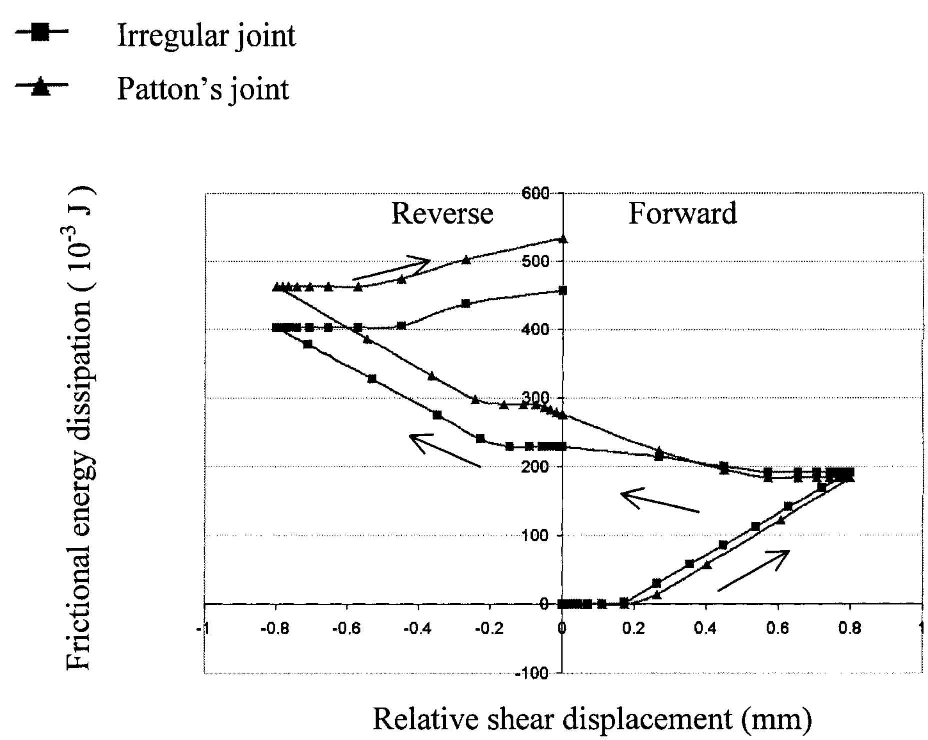

(a). $\sigma_n = 3$ MPa

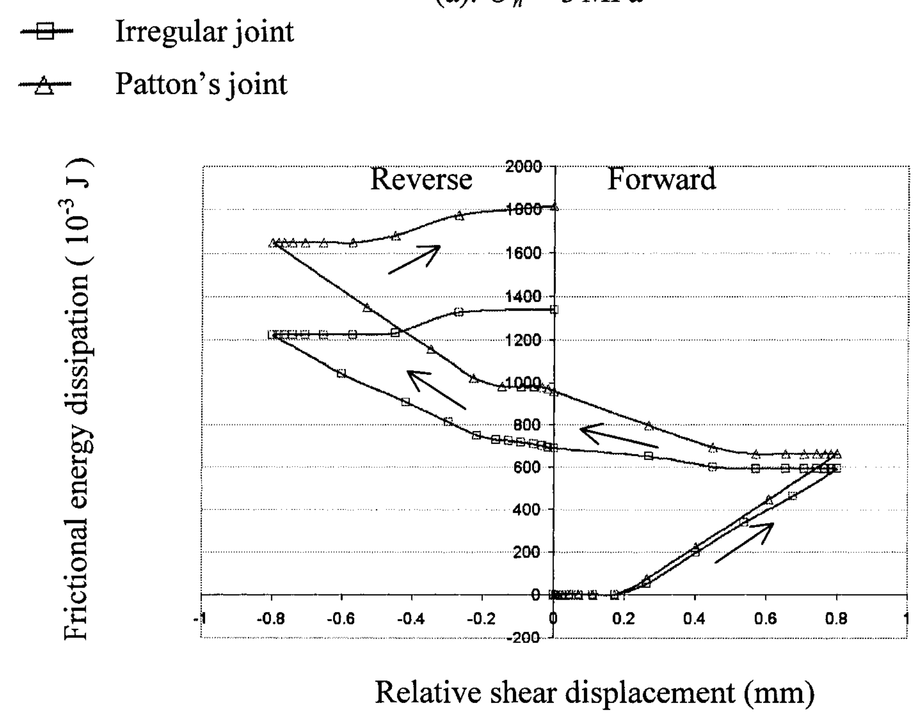

(b). $\sigma_n = 11$ MPa

Figure 5.14 Frictional energy dissipation vs. relative shear displacement during relative shear of regular and irregular joints

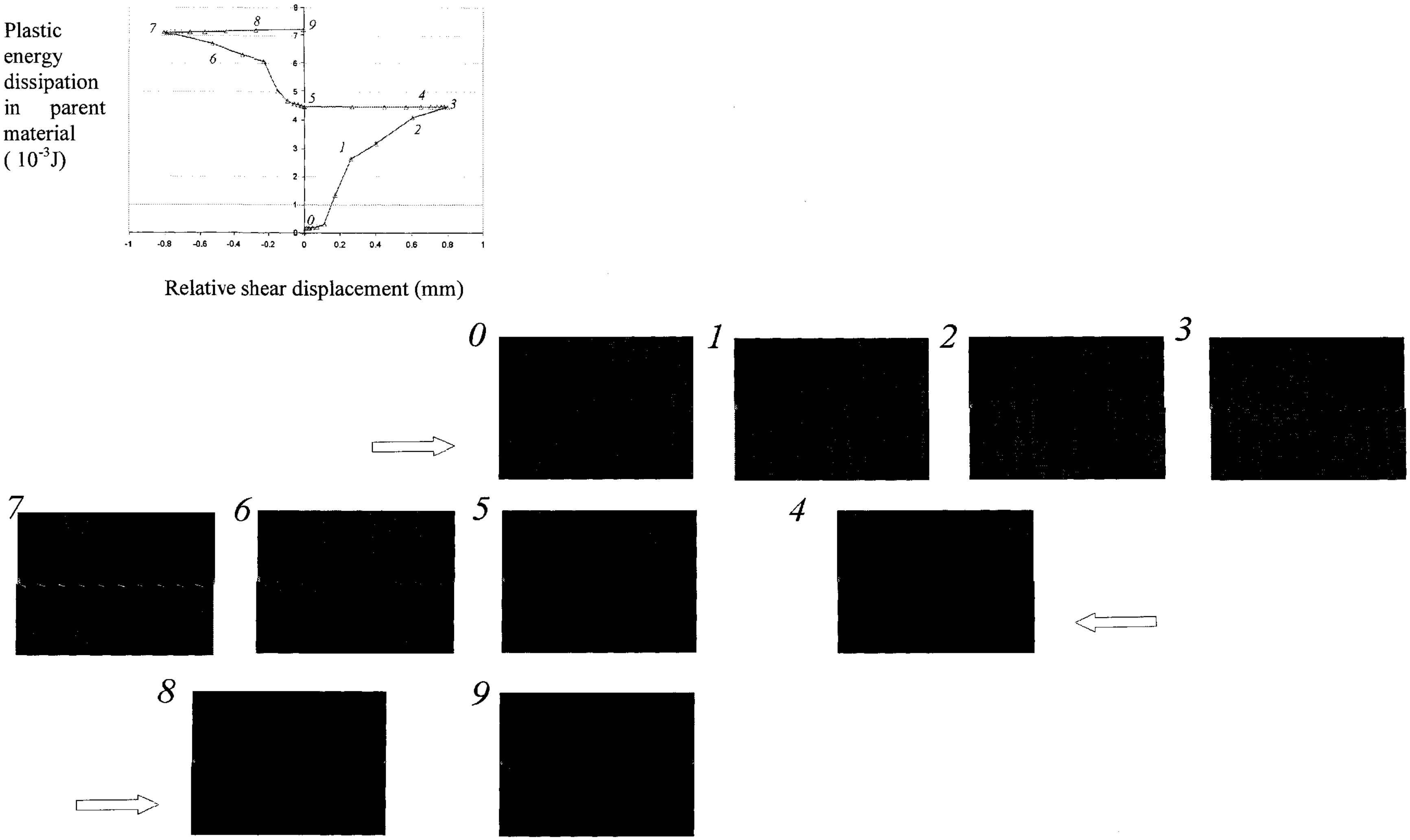

Figure 5.15 Evolution of plastic zones during relative shear of the regular joint under constant normal stress 11 MPa

5.3 Shear behavior of a joint with an idealized steep asperity profile

The objective of this part of the modelling is to determine computationally the influence of asperity angle on the shear behavior, notably the dilatancy and material plastic energy dissipation in the joint. The modelling of such an idealized joint containing regular steep asperity angle is quite arbitrary. The demarcation point between what constitutes a sharp asperity and what constitutes a shallow asperity is not known *a priori*. The behavior is influenced by other factors such as frictional behavior at the joint, joint stiffness and plasticity of material. The objective here is to present some computational results of influences of the asperity angle on the shear response. The physical configuration of the joint surface comprising of sharp asperities is shown in Figure 5.16. Three inclinations of sharp asperities are considered. These include asperity root lengths of 10 mm, 20 mm and 40 mm. The height of the asperities is kept constant at 15 mm and the corresponding asperity angles are approximately 80°, 71° and 56°, respectively. The finite element mesh configuration of conforming surfaces for an asperity angle of 80° is shown in Figure 5.17. The friction between asperity surfaces is kept constant at 0.6745 and the interface stiffness is considered to be a variable. Initial contacts are restricted to the asperities only. The normal stress acting on the idealized joint is also a variable in the problem; The results are, however, presented for normal stress of $3\,\text{MPa}$, $7\,\text{MPa}$, and $11\,\text{MPa}$. The normal stiffness at the contacting surface is assigned values of 0, $13.33\,\text{MPa/mm}$ and $133.33\,\text{MPa/mm}$. The studies by Nguyen and Selvadurai (1998) have utilized the contact stiffness of $13.33\,\text{MPa/mm}$ to model the contact normal stiffness.

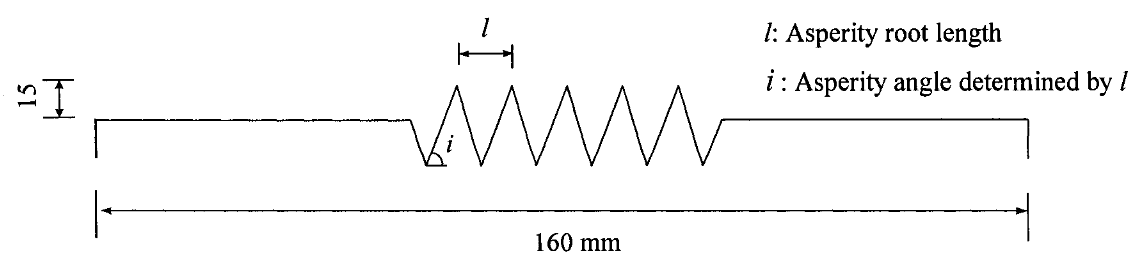

Figure 5.16 Joint profile with sharp asperities

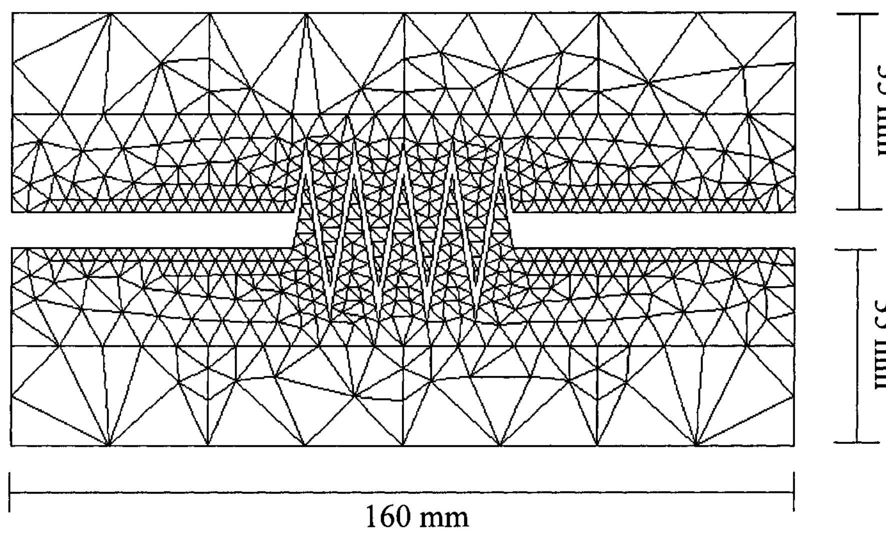

Figure 5.17 Finite element modelling of joint profile with steep asperities

Figure 5.18 and Figure 5.19 shows the influence of asperity angle on the shear response evaluated at normal stress of $7\,\mathrm{MPa}$. In Figure 5.18, plastic energy dissipation is presented. When asperity angles are steep, shear deformation does not induce large relative movement between the contacting surfaces. In this case, frictional energy dissipation is much smaller than the plastic energy dissipation. Especially when asperity is at 80°, the frictional energy dissipation disappears shown in Figure 5.18(b). The relative shear movement observed are therefore mainly due to elastic and plastic deformation in asperities. The plastic energy dissipation increases with asperity root length shown in Figure 5.18(a). The increase in asperity volume allows more plastic deformation. Longer asperity root brings higher shear resistance shown in Figure 5.19(b). Plasticity deformation increases the element volume, which affects the dilatancy. Therefore, as observed in Figure 5.19(a), higher plasticity dissipation brings higher value of dilatancy during shear. Greater value of l also leads to higher dilatancy angle. This might be due to the decreases in the deformability of the asperity, which reduces the amount of deviations of dilatancy angle from the asperity angle and therefore increases in the dilatancy angle.

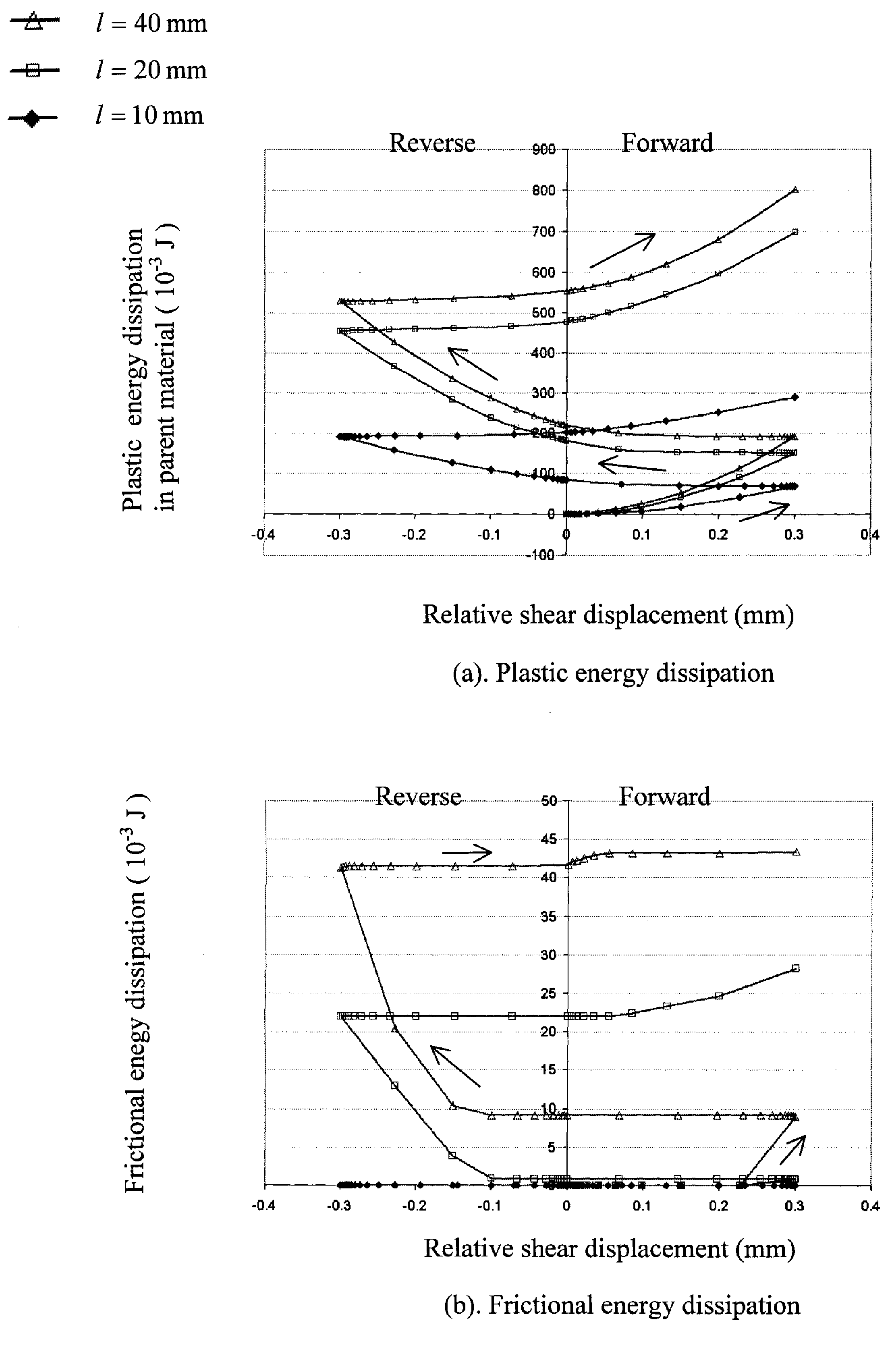

(a). Plastic energy dissipation

(b). Frictional energy dissipation

Figure 5.18 Energy dissipation during relative shear of joints with different steep asperity angles

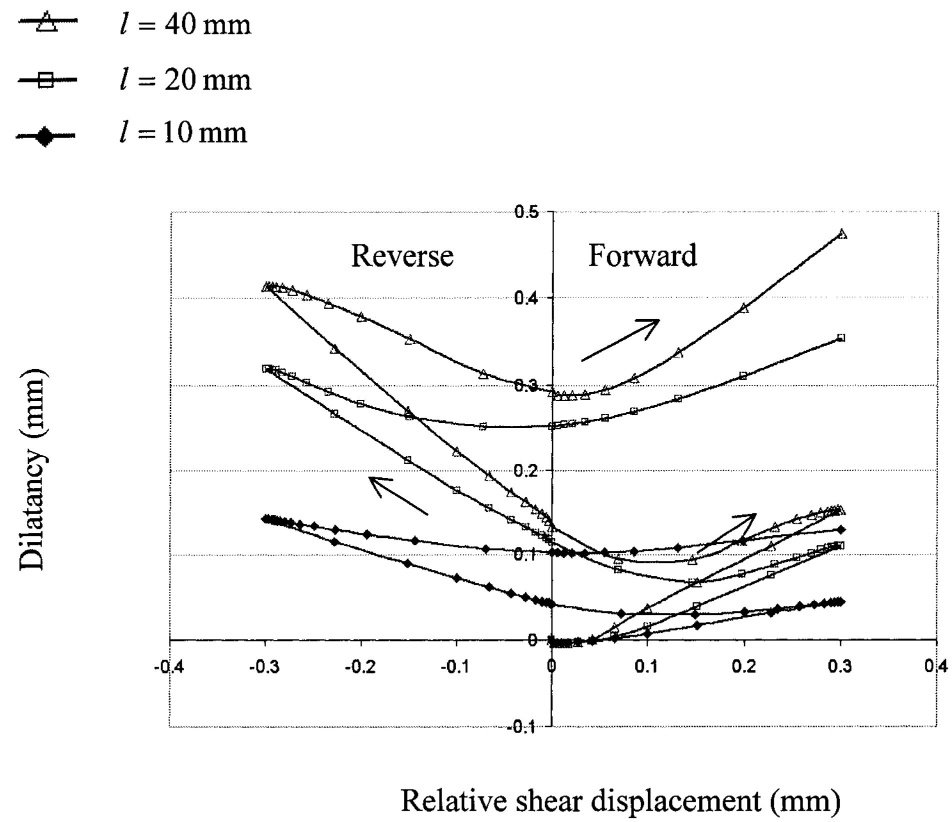

(a). $\sigma_n = 3$ MPa

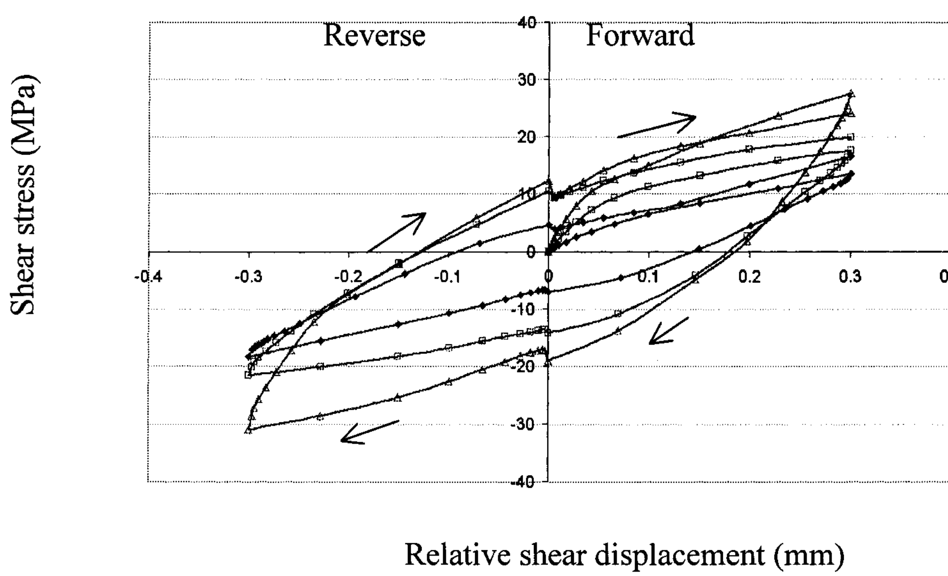

(b). $\sigma_n = 11$ MPa

Figure 5.19 Shear behavior of joints with different steep asperity angles

Figures 5.20 to Figure 5.21 illustrates the shear response of a joint with asperity angle of 80° for different levels of normal stress. Higher normal stresses lead to higher shear resistance and greater normal deformation. The contribution to the plastic energy dissipation is a combination of two factors, i.e., the shear resistance ability and stress state. Consequently, an increase in the normal stress does not necessarily translate to an increase in the plastic energy dissipation during shear. Figure 5.20 shows that, increasing in normal stress from $3\,\text{MPa}$ to $7\,\text{MPa}$ induces a greater plastic energy dissipation; further increase in normal stress from $7\,\text{MPa}$ to $11\,\text{MPa}$, increases the shear resistance [Figure 5.21(b)], but it reduces the plastic energy dissipation. The variation of dilatancy follows a similar pattern. Due to the associated flow rule used, a greater plastic deformation leads to an increase in the element volume, which contribute to dilatancy. Figure 5.21(a) shows that, a stress increase from $3\,\text{MPa}$ to $7\,\text{MPa}$ leads to greater dilatancy, whereas a further increase from $7\,\text{MPa}$ to $11\,\text{MPa}$ leads to a reduction in dilatancy.

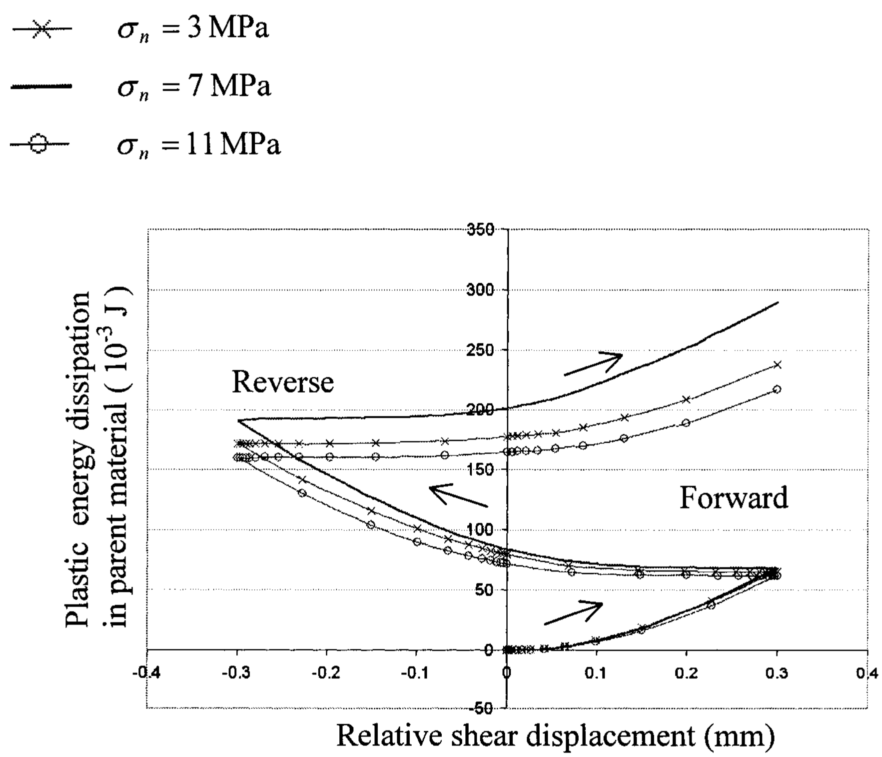

Figure 5.20 Plastic energy dissipation in material during shear at different values of normal stresses

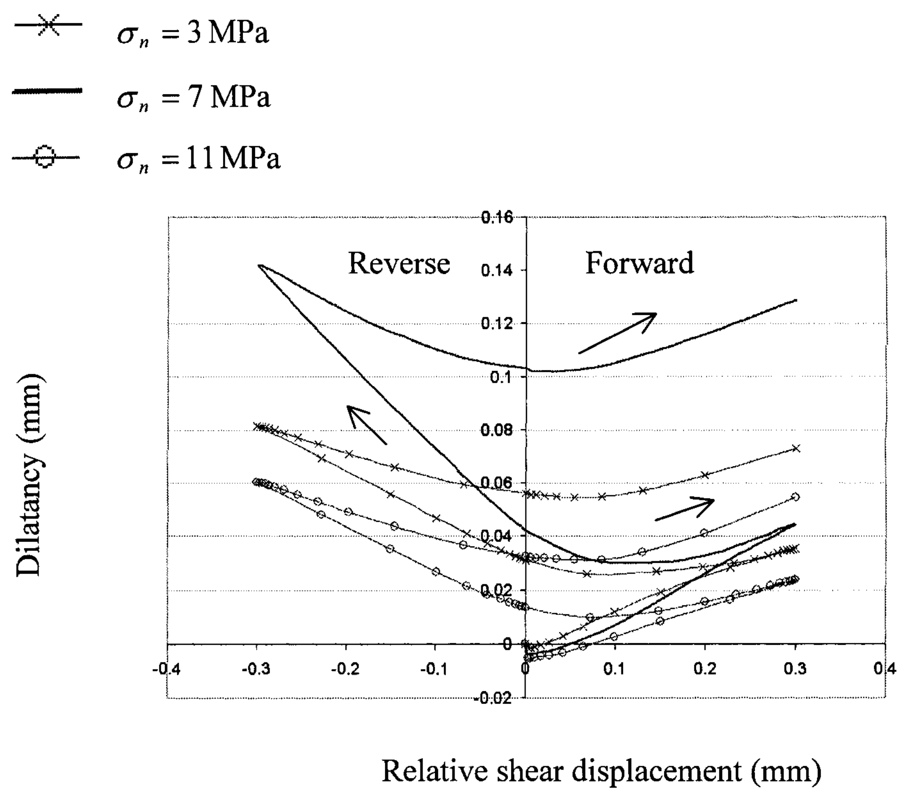

(a). Variation of dilatancy

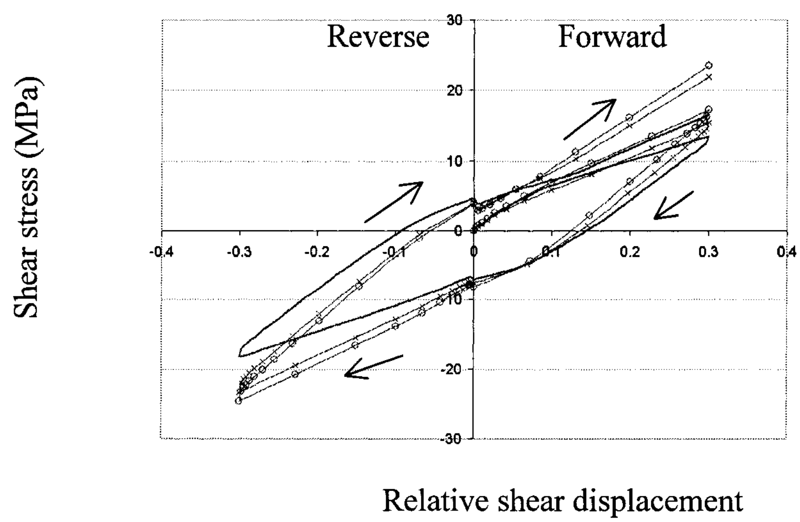

(b). Variation of shear stress

Figure 5.21 Shear behavior at different values of normal stress

Figures 5.22 to 5.24 illustrate the shear response of joints with steepest asperity angle 80° evaluted for initial normal stress of $7\,\mathrm{MPa}$ and variable normal stiffness. In these simulations, shearing of the joints does not induce relative movement between contacting surfaces. The frictional dissipation disappears in the absence of slip between contacting surfaces. In Figure 5.22, the plastic energy dissipation is presented. The difference in plastic energy dissipation in the material, during shear conducted under different stiffness condition, is small. The noticeable reduction in plastic energy dissipation at presence of normal stiffness and in latter shear cycles is due to the increase in the shear resistance. Figure 5.23 illustrates the evolution of plastic zones during shear, under an initial normal stress of $7\,\mathrm{MPa}$ and constant normal stiffness $133.3\,\mathrm{MPa/mm}$. Initially, only relative small plastic zones develop in the parent material; the plastic zones, however, extend during the later stages of the shear cycle. At the end of the shear cycle examined, almost all the asperities fail by a clear plastic zone extending through its root. Although there is no relative movement between contacting surfaces, the largest dilatancy reaches up to about $0.14\,\mathrm{mm}$ [see Figure 5.24(a)]. Dilatancy angle is, however, only around at 13.0°, which greatly deviates the asperity angle. The appearance of dilatancy at the absence of slip between contacting surfaces indicates the possibility for evolution of hydraulic conductivity only in parent material. The results shown in Figure 5.24(b) also indicate that, although a slight increase in the shear resistance is noticeable due to the presence of the shear stiffness, the shear stress-relative shear displacement behavior is insensitive to the change of the normal stiffness.

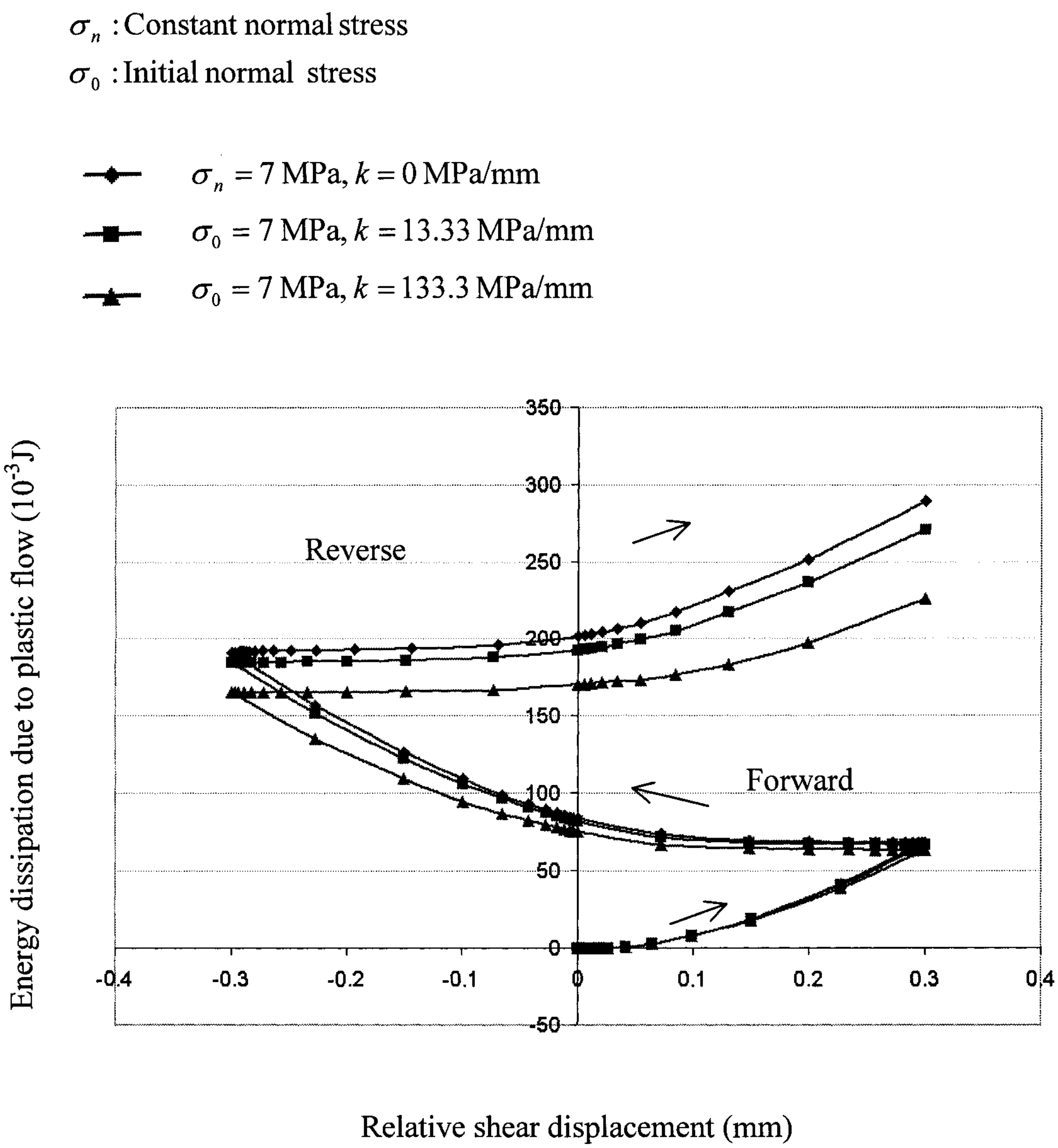

Figure 5.22 Plastic energy dissipation in material during shear of joint with steep asperity angle of 80° at different normal stiffness

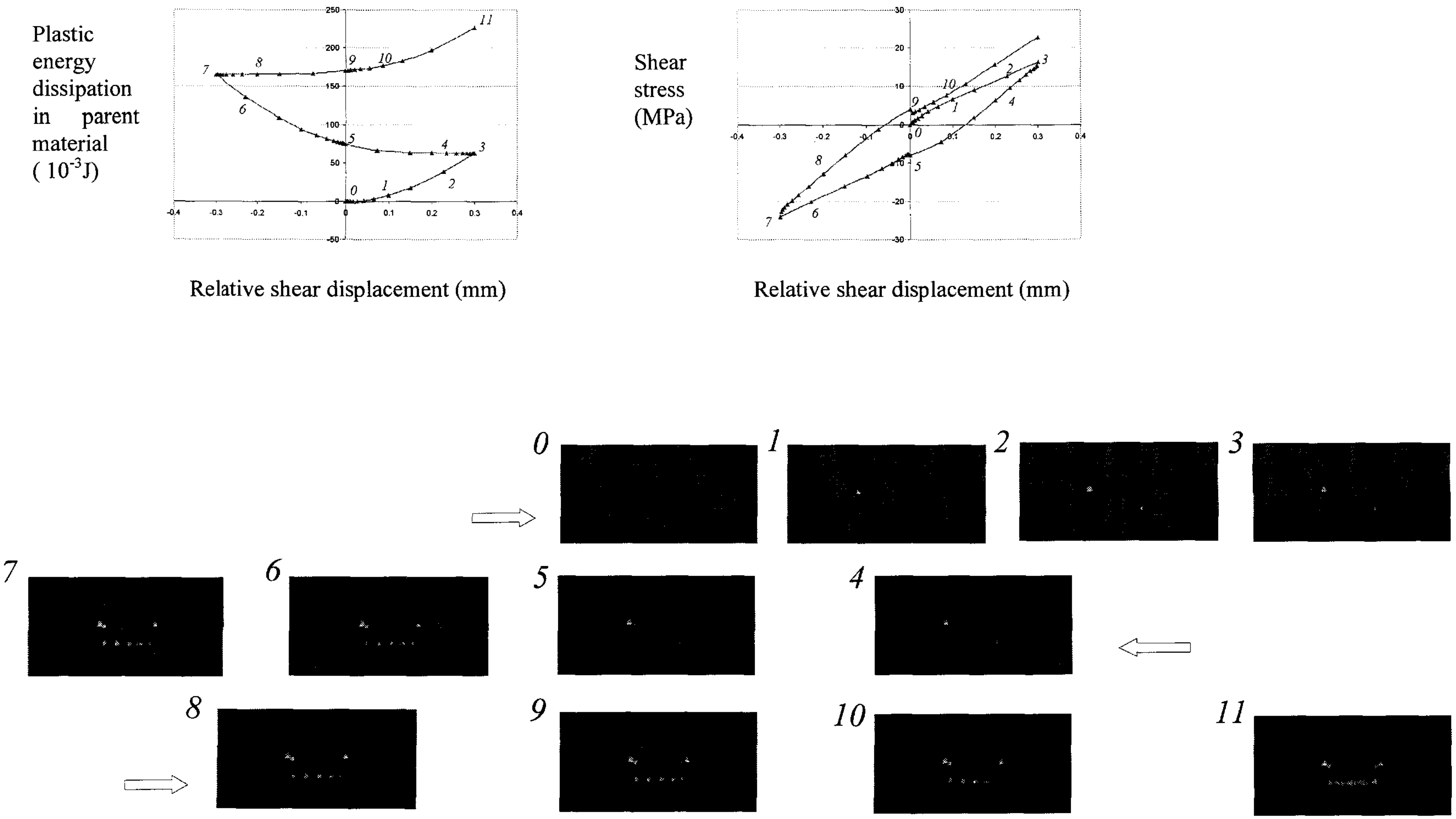

Figure 5.23 Evolution of plastic zones during relative shear in the absence of slip (under initial stress 7 MPa and constant normal stiffness 133.33 MPa/mm)

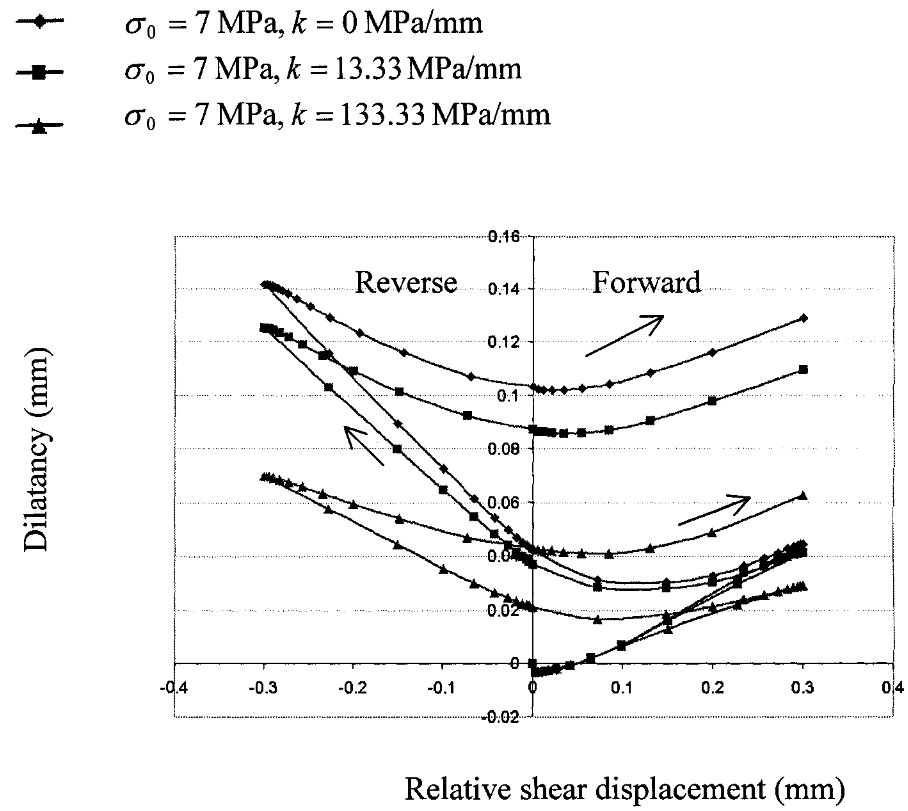

(a). Variation of dilatancy

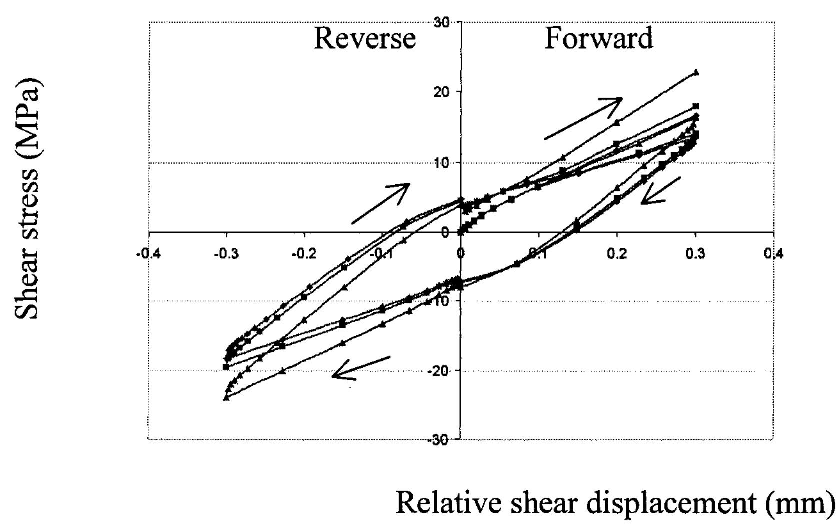

(b). Variation of shear stress

Figure 5.24 Shear behavior of joint with steep asperity angle of 80° at different normal stiffness

5.4 Shear behavior of an irregular joint under constant normal stress and constant normal stiffness

In order to examine the influence of the boundary condition of normal stress or normal stiffness on shear behavior; another rougher irregular dolerite joint, modelled under constant normal stress and constant normal stiffness, is subjected to a single cycle of shear. The natural profile used at 300 mm length is a left section of an irregular profile at 1000 mm length presented by Chryssanthakis and Barton (1990). The profile with distorted vertical scale is shown in Figure 5.25(a). The finite element mesh on an undistorted scale is shown in Figure 5.25(b). The joint is subject to initial normal stresses of 11 MPa and 20 MPa. Normal stiffness is maintained at 13.33 MPa/mm during shear under constant normal stiffness.

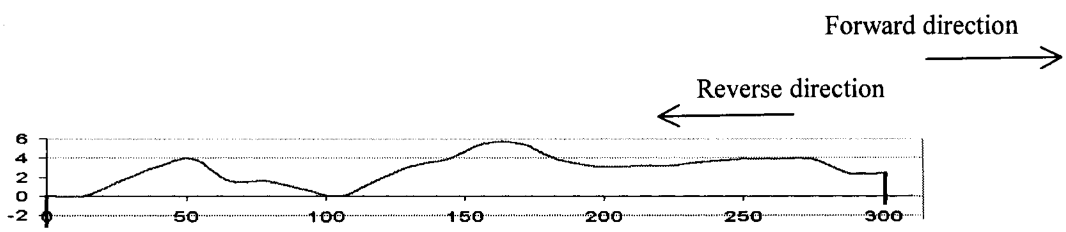

(a). 2D joint profile (after discretization)

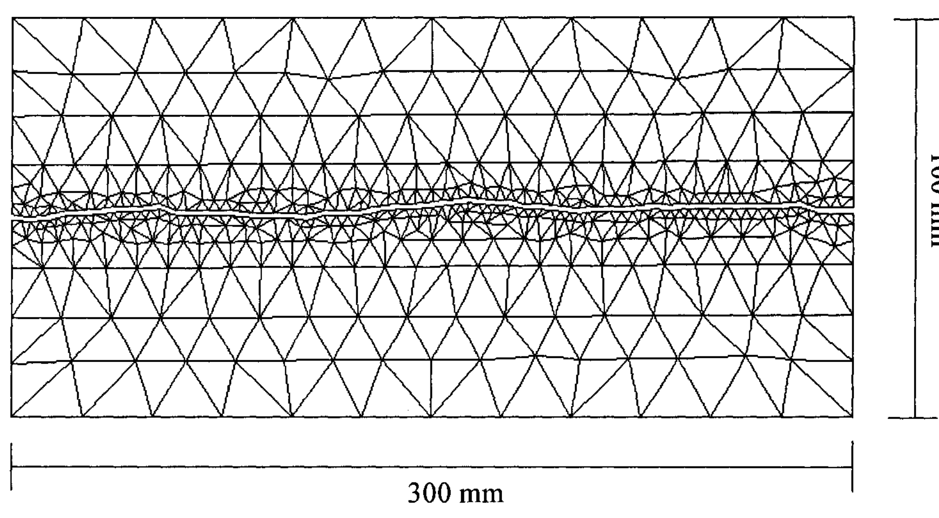

(b). Mesh configuration (initially compatible, 690 elements and 1594 nodes)

Figure 5.25 Shear of an irregular joint at 300 mm length

The presence of normal stiffness k causes a greater suppression of dilatancy (Figure 5.27) and induces higher stress normal to joint surface as relative shear takes place. Due to this, greater shear resistance is observed in Figure 5.26. Variation of frictional energy dissipation with normal stiffness follows a similar pattern (Figure 5.28). Computational modelling of shear on joints with steep asperity angle indicates that reduced plastic energy dissipation will be obtained due to increase in normal stiffness. Shearing of an irregular joint, however, gives a positive relationship between plastic energy dissipation and normal stiffness. Contacting between irregular surfaces only occurs at limited regions. Increasing in normal stress resulting from presence of normal stiffness significantly changes the stress states of these contacting regions and therefore, as shown in Figure 5.29, increases the plastic energy dissipation in material. The differences can reach up to five times at some displacement between the cases under constant normal stress and under constant normal stiffness. Figure 5.30 shows the evolution of plastic zones at a higher constant normal stress of $20\,\text{MPa}$. For purpose of comparison, Figure 5.31 illustrates the evolution of plastic zones under constant normal stiffness 13.33MPa and at an initial normal stress of $20\,\text{MPa}$. Although plastic energy dissipation in the material has different values for two cases, it seems that the plasticity occurs at similar locations and exhibits a similar pattern. The reason for this might be that zones of plastic flow are restricted to the contacting regions and the regions in contact are mainly determined by the geometry of surfaces; the absolute value of plastic energy dissipation is, however, more dependent on the stress states surrounding contacting regions.

σ_n : Constant normal stress

σ_0 : Initial normal stress

$\sigma_n = 11$ MPa, $k = 0$ MPa/mm

$\sigma_n = 20$ MPa, $k = 0$ MPa/mm

$\sigma_0 = 11$ MPa, $k = 13.33$ MPa/mm

$\sigma_0 = 20$ MPa, $k = 13.33$ MPa/mm

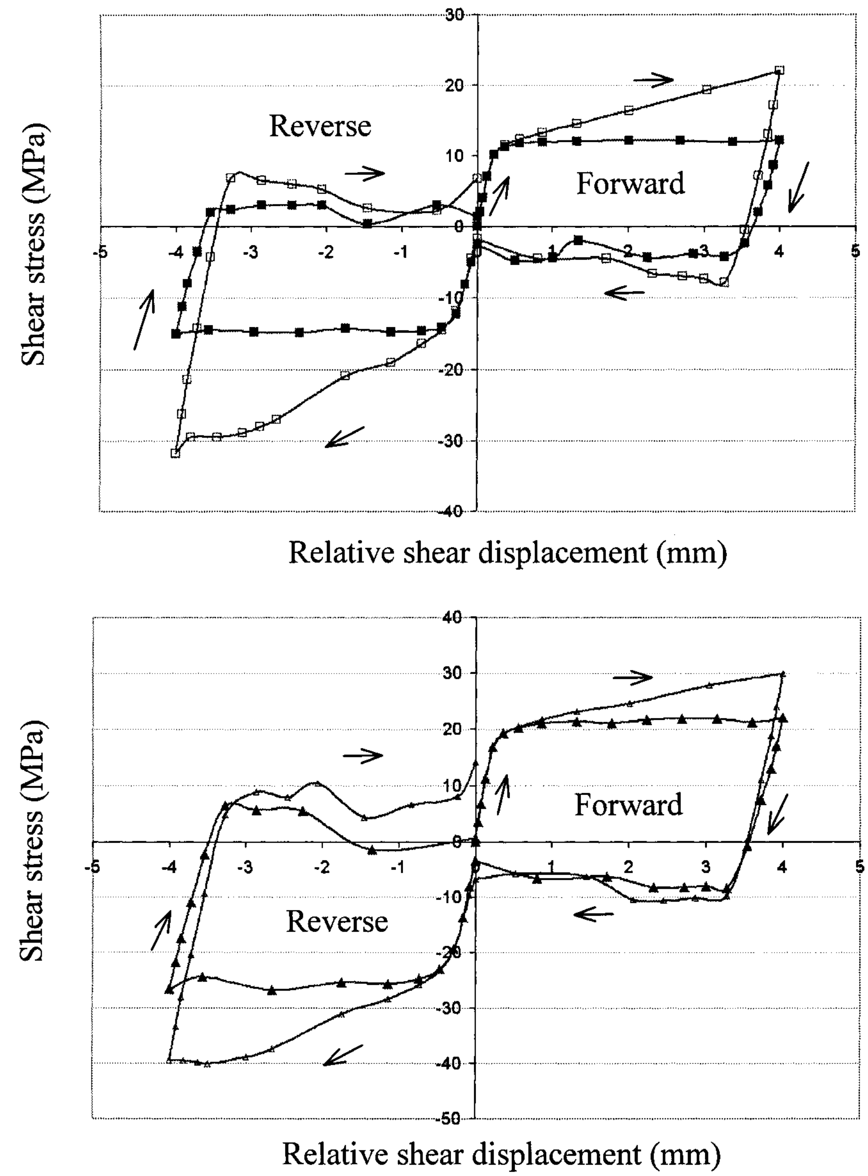

Figure 5.26 Shear stress vs. relative shear displacement during a single cycle of shear under constant normal stress and constant normal stiffness

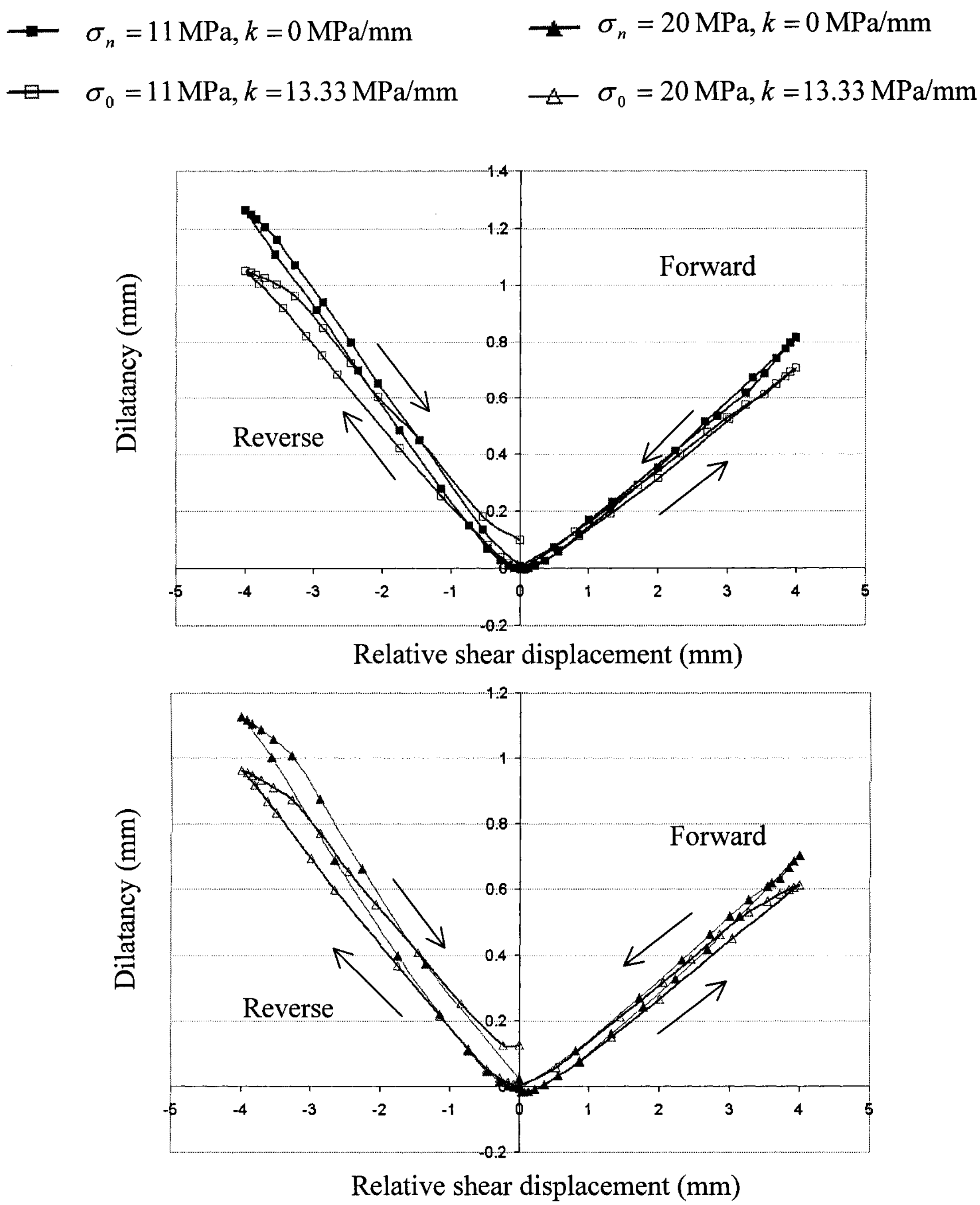

Figure 5.27 Dilatancy vs. relative shear displacement during a single cycle of shear under constant normal stress and constant normal stiffness

σ_n : Constant normal stress

σ_0 : Initial normal stress

$\sigma_n = 11$ MPa, $k = 0$ MPa/mm $\sigma_n = 20$ MPa, $k = 0$ MPa/mm

$\sigma_0 = 11$ MPa, $k = 13.33$ MPa/mm $\sigma_0 = 20$ MPa, $k = 13.33$ MPa/mm

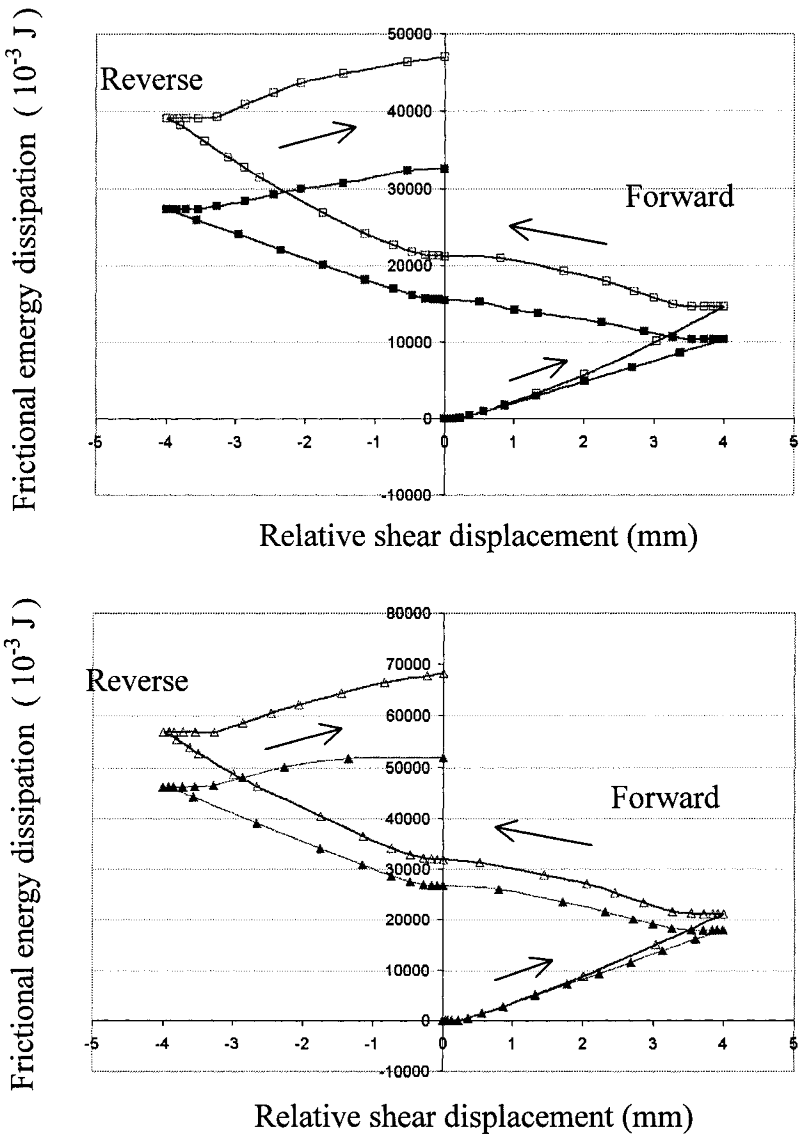

Figure 5.28 Frictional energy dissipation vs. relative shear displacement during a single cycle of shear under constant normal stress and constant normal stiffness

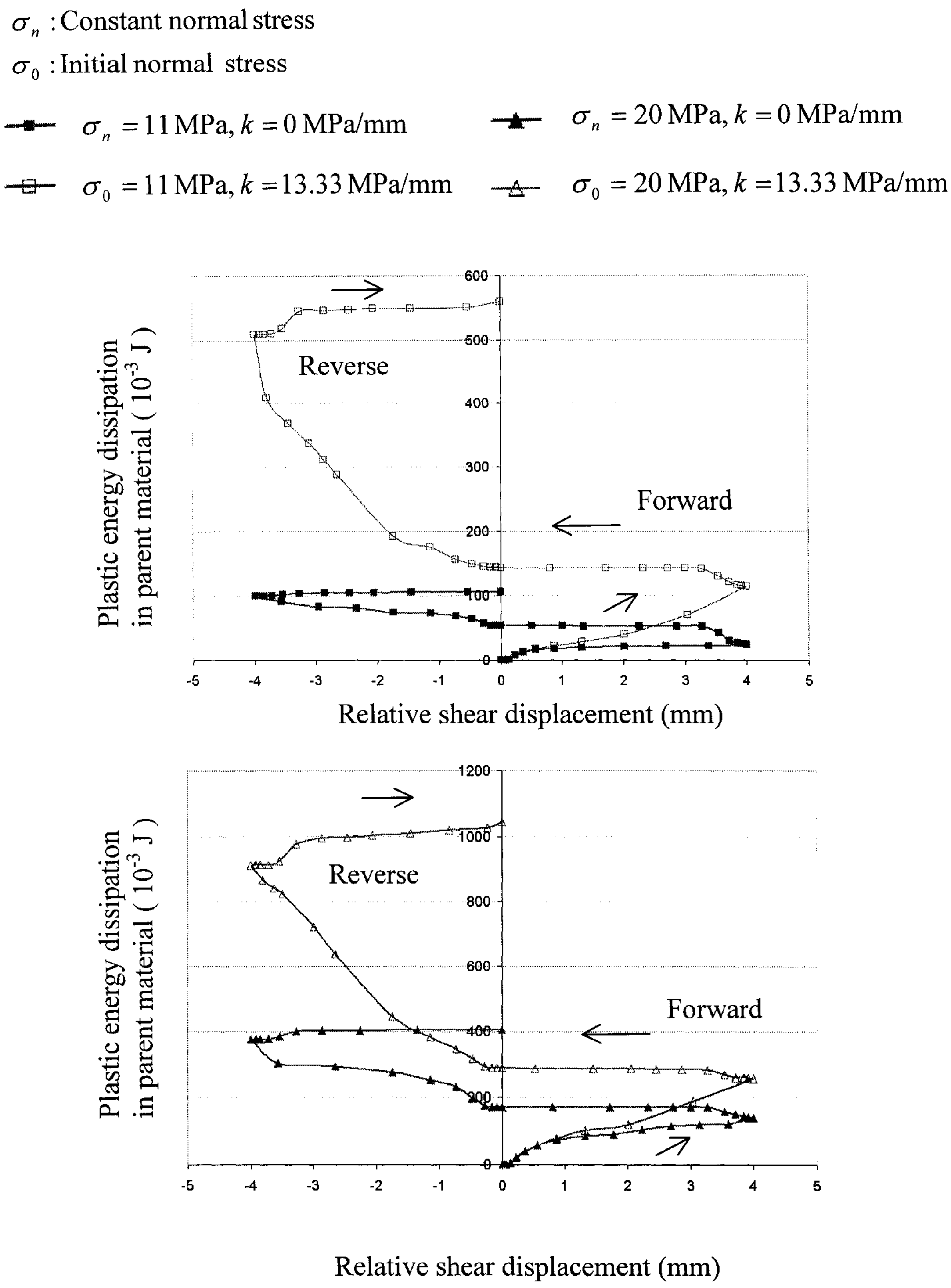

Figure 5.29 Energy dissipation due to plastic flow vs. relative shear displacement during a single cycle of shear under constant normal stress and constant normal stiffness

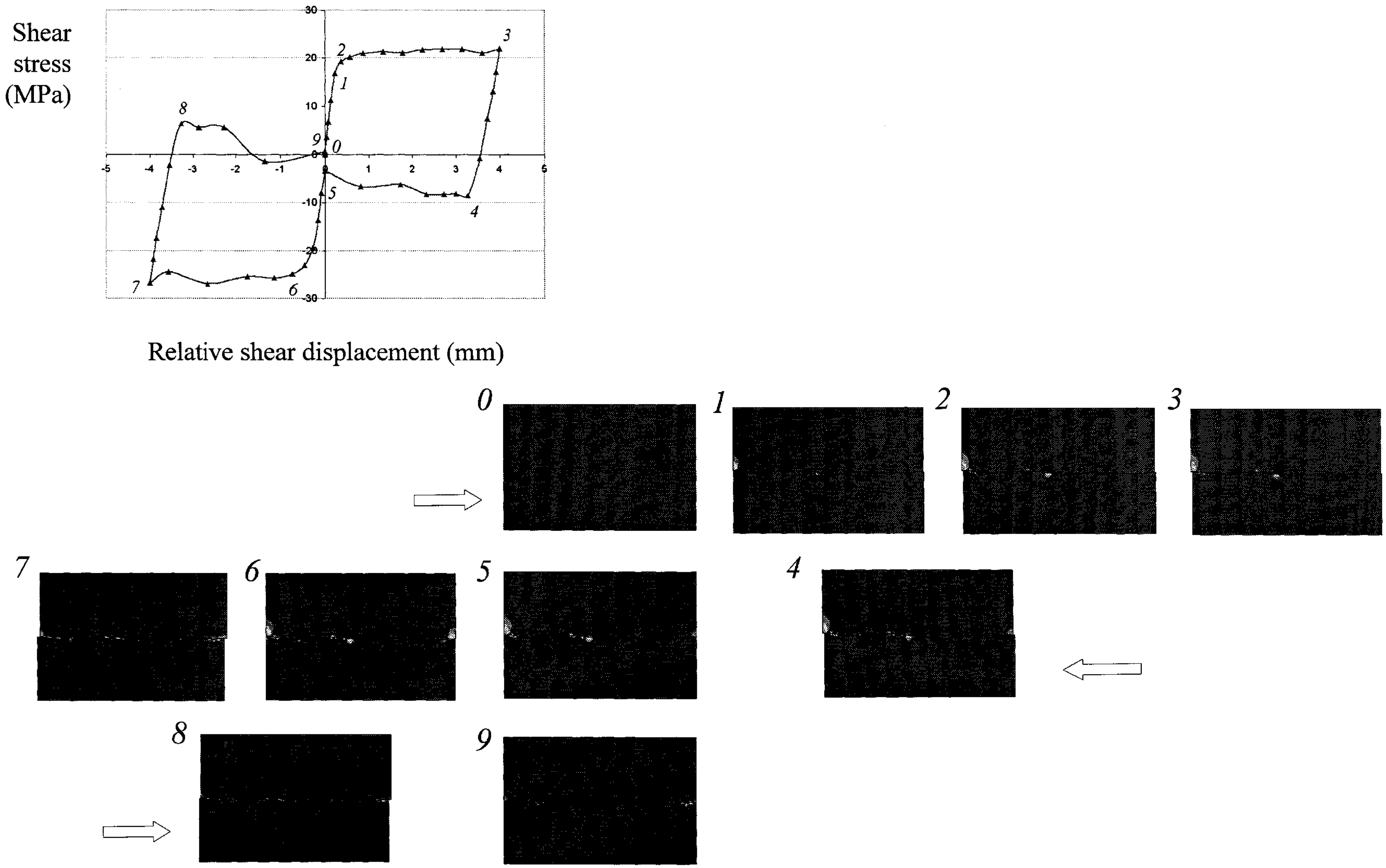

Figure 5.30 Evolution of plastic zones during a single cycle of relative shear conducted under constant normal stress 20 MPa

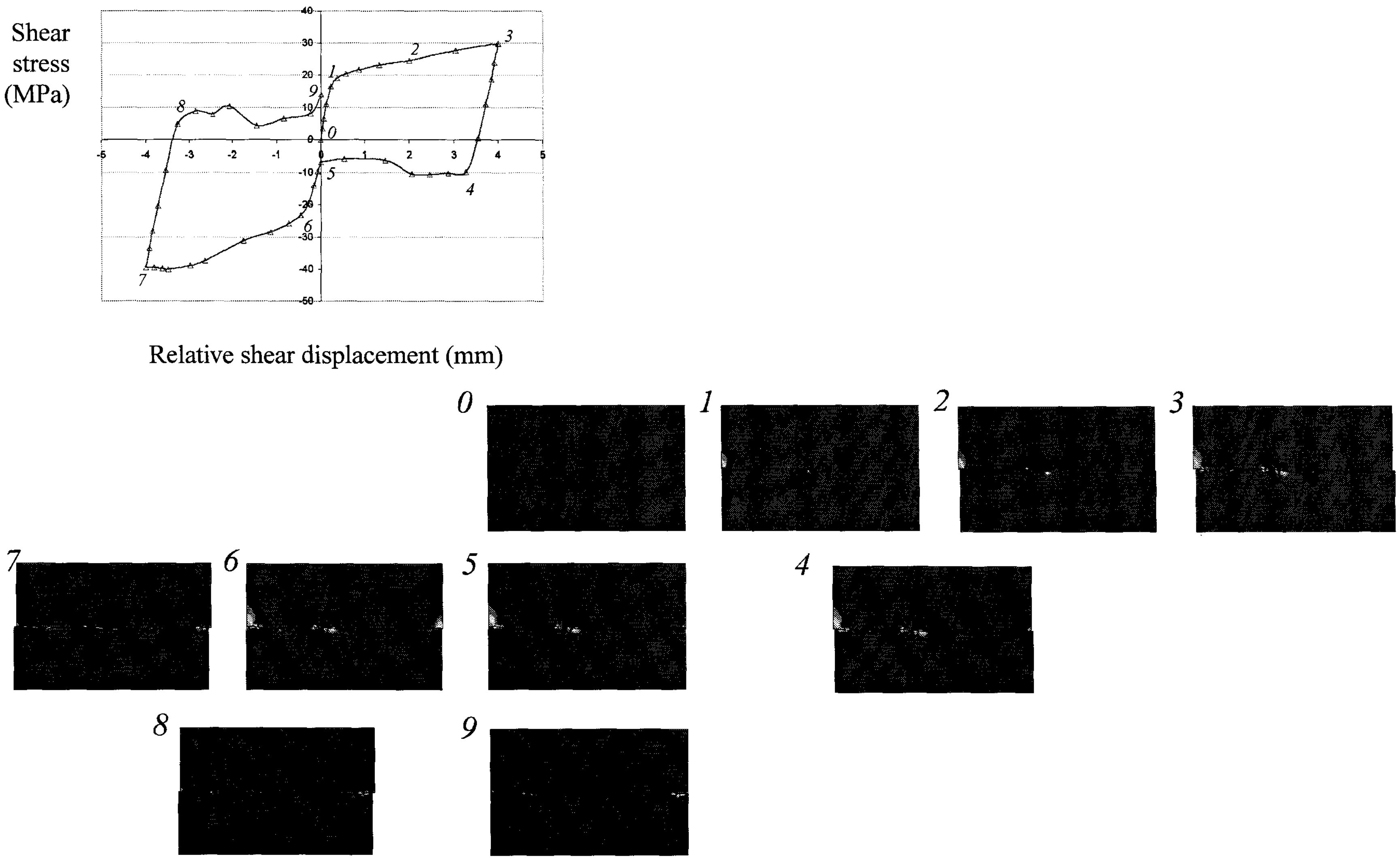

Figure 5.31 Evolution of plastic zones during a single cycle of relative shear conducted under initial normal stress 20 MPa and constant normal stiffness 13.33MPa/mm.

5.5 Variation of dilatancy during 5-cycle-shear

In a plastic material, the history of loading can influence the shear behavior. In order to investigate the influence of such an effect, a joint with an irregular profile of 300 mm length, which was presented, in the previous section, is sheared up to 5 cycles. Initial normal stress 11 MPa is applied to observe the variation of dilatancy in different cases. Figure 5.32 shows the variation of dilatancy with shear displacement during shear under constant normal stress of 11 MPa and Figure 5.33 shows the variation of dilatancy under initial stress 11 MPa and constant normal stiffness 13.33 MPa/mm. For purpose of comparison, the variation of dilatancy in the absence of plasticity is also presented in Figure 5.34. The peak dilatancy in different cycles is also presented in each Figure.

In both cases, in presence of plasticity, dilatancy increases while dilatancy angle decreases with increase in the number of shear cycles. The presence of normal stiffness enhances the development of irreversible dilatancy. In the absence of plasticity, however, the dilatancy remains independent of the number of loading reversal cycles. This indicates that the change of dilatancy during load cycling is directly related to plastic deformation of the material regions. Due to the associated flow rule adopted, material volume increases and this results in an increase in the dilatancy with increasing number of the shear cycles; material plastic deformation also increases the deformability of the contacting asperities, which reduces the dilatancy angle in later cycles. Experimental evidence (Wibowo et al., 1992), however, indicates a decrease in both dilatancy and dilatancy angle with increasing number of shear cycles. In actual experiments, asperities are damaged during shear and can further be crushed to create fragmented gouge material residing at the joint locations. In numerical modelling, however, continuum analysis makes no allowance for creation of gouge and disintegration of asperities. Asperity failure in form of plastic flow increases the element volume, which increases the dilatancy during shear cycling.

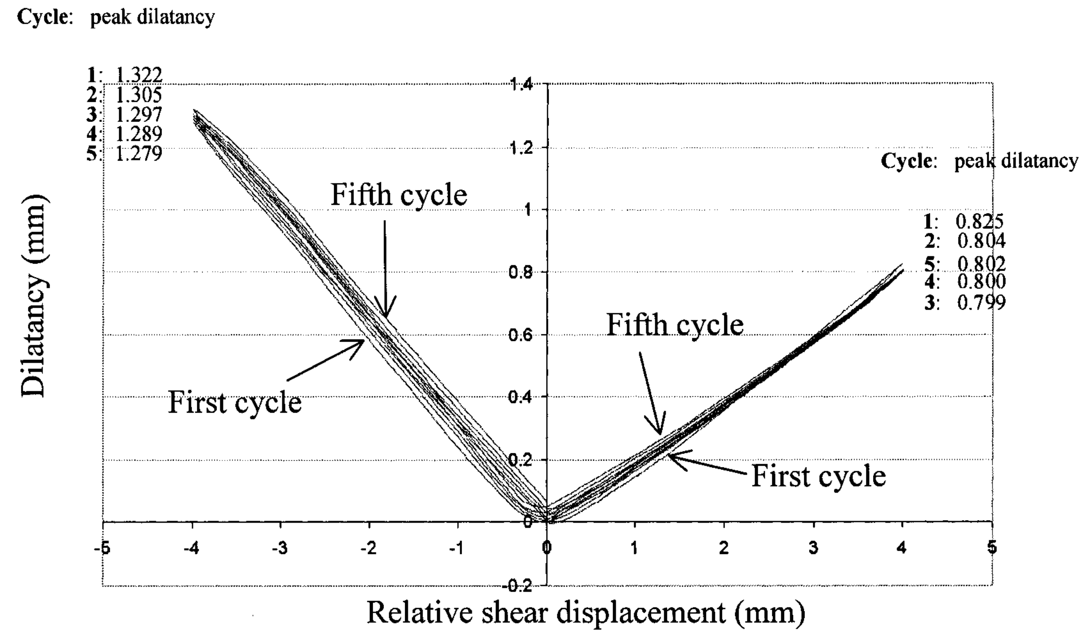

Figure 5.32 Variation of dilatancy during 5 cycles of relative shear conducted at a constant normal stress $\sigma_n = 11\,\text{MPa}$ and zero normal stiffness

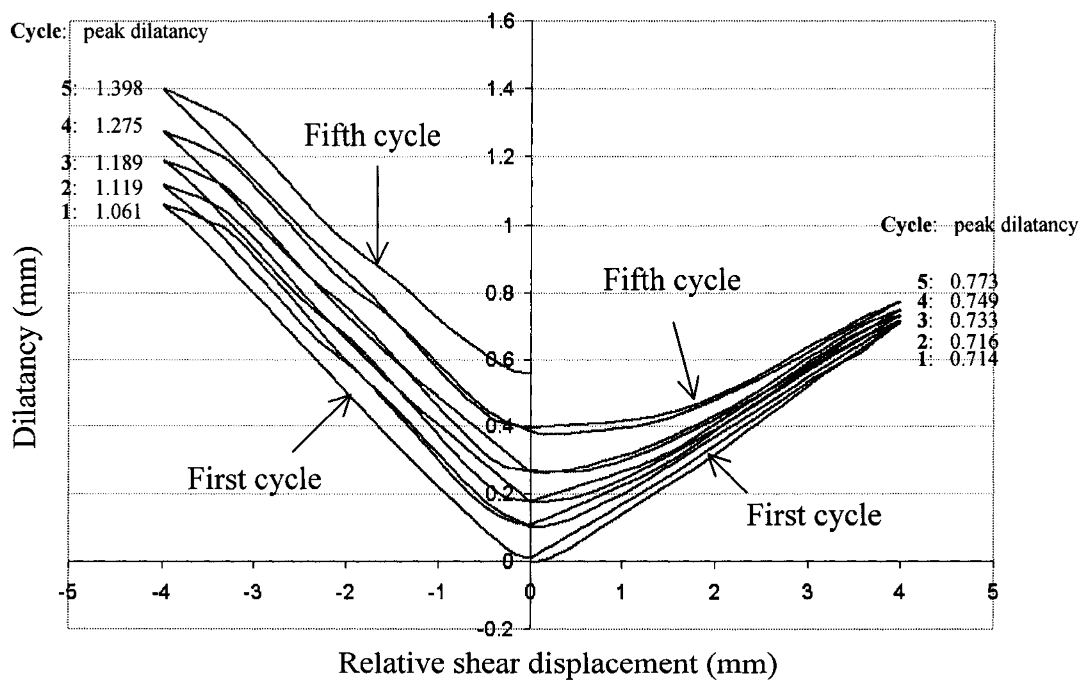

Figure 5.33 Variation of dilatancy during 5 cycles of relative shear conducted at an initial normal stress $\sigma_0 = 11\,\text{MPa}$ and constant normal stiffness $k = 13.33\,\text{MPa/mm}$

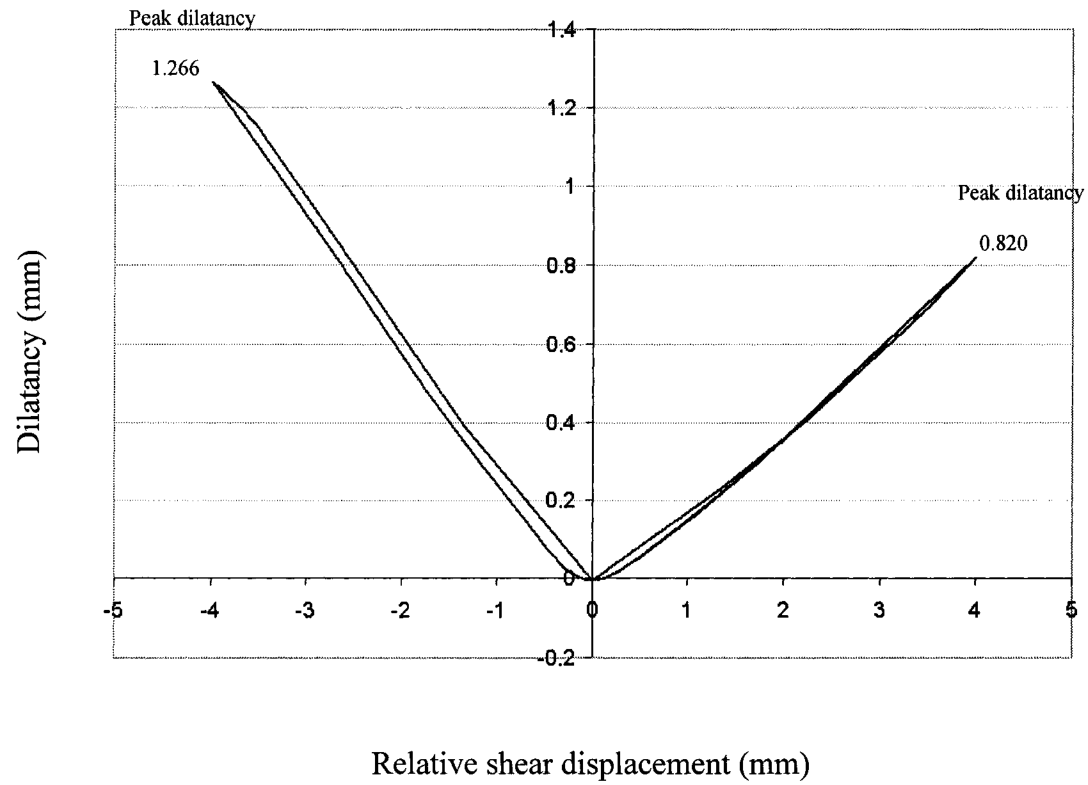

Figure 5.34 Variation of dilatancy during 5 cycles of relative shear conducted under a constant normal stress $\sigma_n = 11\,\text{MPa}$ and zero normal stiffness in the absence of plasticity

5.6 Shear behavior of an irregular joint with initial gap

The irregular dolerite joint of $300\,\text{mm}$ length discussed in previous two sections is further utilized to examine a situation involving the shear of a joint with an initial seperated gap. The existence of initial gap at joint is of some interest in connection with joints, which experience thermal shrinkage at joints and discontinuities.

The computational model used for examining the initially perfectly matched joint is the same as that discussed in sections 5.4 and 5.5. For the purpose of comparison, a monotonic shear simulation is also performed on the dolerite joint, which is configurated with initial gaps at $1\,\text{mm}$ and $2\,\text{mm}$. Since the two faces of the joint are in a separated condition, normal stresses cannot be applied to the joint. A constant normal stiffness is however applied for the loading configuration.

Figure 5.35 shows the variation of shear stress with shear displacement. Appearance of the initial aperture significantly reduces the peak shear strength. The shear behavior appears to be more ductile with the existence of initial gap. Figure 5.36 shows the variation of dilatancy with shear displacement. The dilatancy effects have been greatly reduced due to the presence of the initial gap.

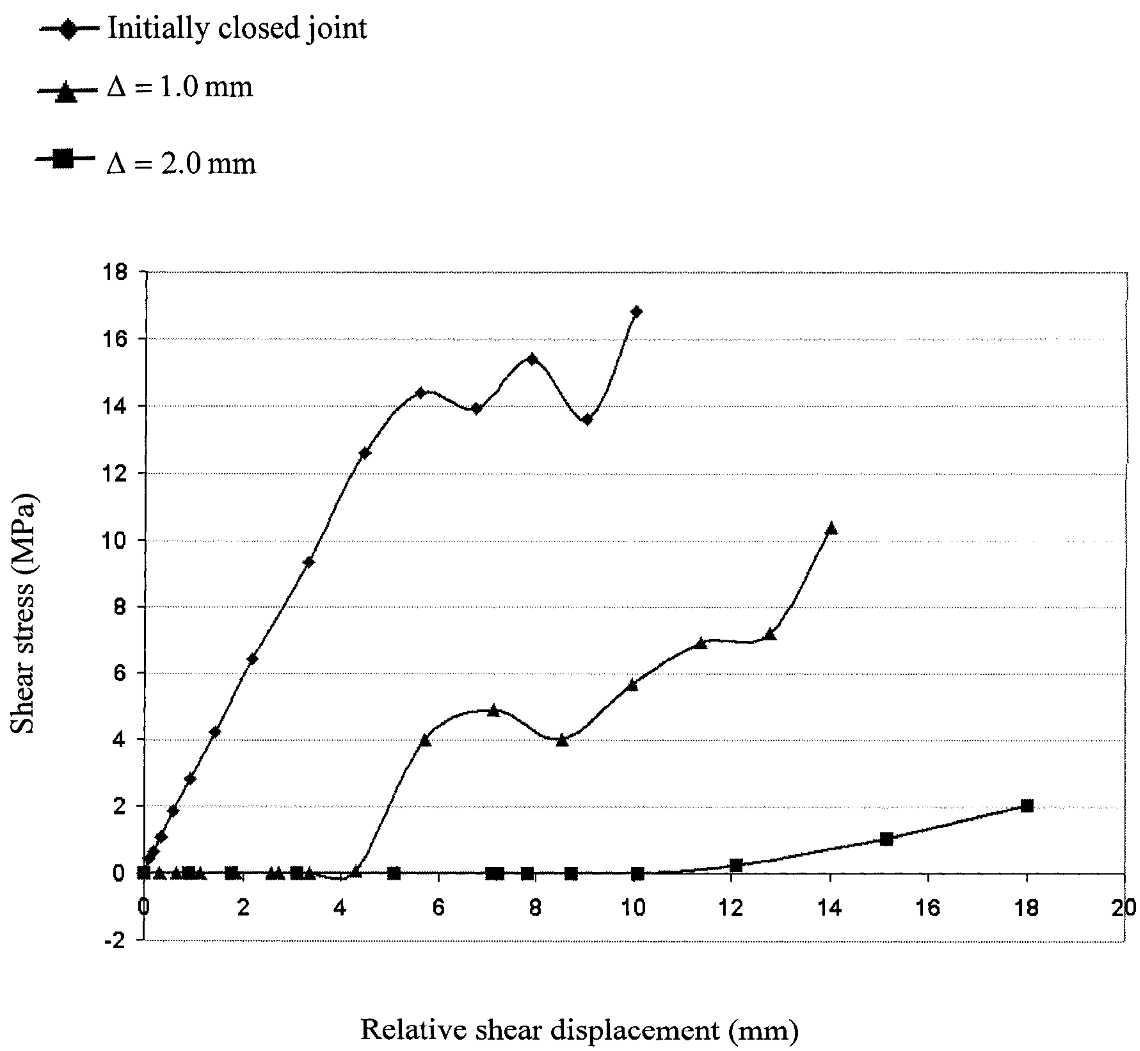

Figure 5.35 Shear behavior of joints with initial apertures

Initial normal stress $\sigma_0 = 0$ MPa

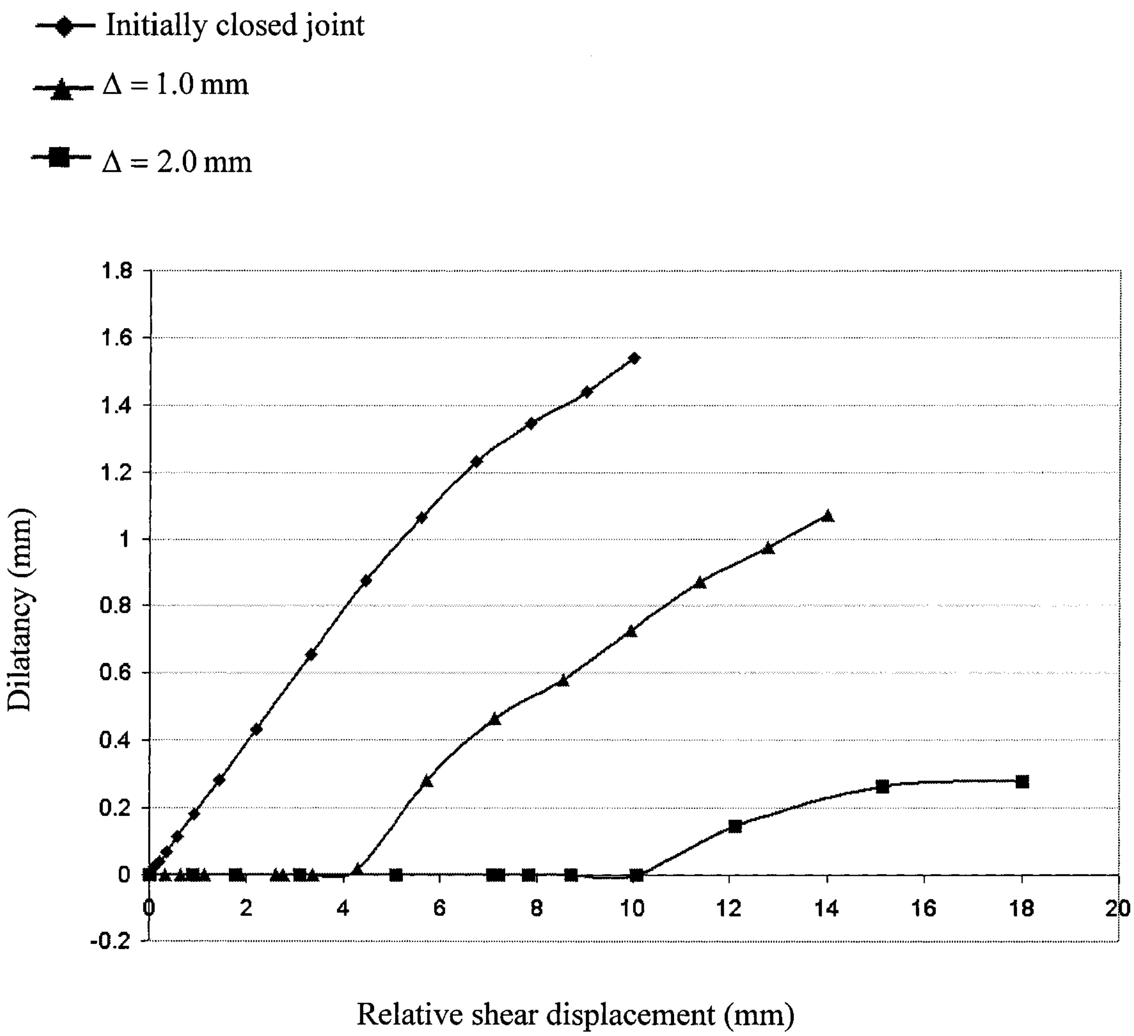

Figure 5.36 Dilatancy during relative shear of joints with initial apertures

5.7 Summary

Computational modelling can be used to examine the shear behavior of rock joints for a variety of cases of joint profiles and testing conditions. Although attention is only restricted to dolerite, similar results can also be obtained to other types of rocks or other brittle geomaterials, including concrete. The major results in this chapter are listed below:

(i) During the application of a relative shear to a rock joint, contact between the irregular surfaces is established only at limited points. The restraint against the two regions of the joint has some influence on this process. Computational simulations indicate that interfacial interaction at other sections appears to have negligible effect on the final behavior of the joint. Mechanical behavior of interface involving these critical locations therefore governs the overall shear behavior of the entire joint. Dilatancy during shear, which is also influenced by the normal stiffness, roughly follows the surface geometry of the governing asperity or asperities. A regular triangular joint with a same asperity angle as that of the "*governing asperity*" exhibits a similar response in dilatant behavior and shear stress as those associated with the irregular joint. This provides a procedure to predict the shear resistance of an irregular joint based on Patton's suggestion.

(ii) In comparison between an irregular joint and the simplified joint, we observe an important influence of roughness on the shear behavior. Omission of the local profile neglects some important information about joint feature, such as contributing dilatancy and peak shear stress. Most of the energy dissipation due to plastic deformation occurs at the small governing asperities. Disregarding such asperities contribute to a significant loss of the plastic energy dissipation in material. Frictional energy dissipation, however, is relatively not influenced by the omission of the local profile.

(iii) An increase in the normal stiffness k causes a greater suppression of dilatancy, which leads to higher shear stress and frictional energy dissipation.

Especially, due to the presence of normal stiffness, the plastic energy dissipation in the material region increases significantly during relative shear of the irregular joint.

(iv) Relative movements between irregular surfaces are accompanied by dilatancy, frictional energy dissipation and plastic energy dissipation in the parent material. In studies of the irregular joint, the plastic energy dissipation in material is two orders of magnitude smaller than the frictional energy dissipation. In studies of joints with steep asperities, however, shear induces only a slight movement with respect to each other between the contacting surfaces. The relative movement between the joint surfaces is mainly due to the plastic and elastic deformation in the asperities. The contribution of the dilatancy to the shear behavior is low and the variation of the shear stress, plastic energy dissipation with relative shear displacement is insensitive to the values of the normal stiffness. Most of the energy will then be dissipated in the form of plastic energy deformation in material instead of the frictional energy dissipation at the contact surfaces. Higher normal stress leads to higher shear resistance and higher normal deformation. The contribution of the normal stress to plastic energy dissipation is due to a combination of these two factors. When the asperity angle is steep, an increase in normal stress does not necessarily result in higher plastic energy dissipation; it might increase the plastic energy dissipation due to the increase in stress state, but sometimes this is reduced due to the increase in shear resistance.

(v) The presence of an initial aperture significantly changes dilatancy and shear stress behavior of an irregular joint. The peak shear stress values tend to be reduced as the aperture increases.

The influence of quasic-static shear cycling on the plastic behavior of the joint can also be studied through the computational modelling procedure. In actual experiments, asperities are damaged during shear and they can further be crushed to create fragmented gouge material residing at the joint locations. Experimental evidence indicates the reduction of both dilatancy and dilatancy angle with increases in shear cycles. In the current numerical modelling procedure, however, the continuum behavior of both regions of the joint makes no allowance for creation of gouge resulting from disintegration of asperities. Asperity failure in form of plastic flow increases the element volume, which increases the dilatancy during shear cycling. Plastic energy dissipation increases the deformability of asperities and reduces the dilatancy angle in latter shear cycles.

Chapter 6

CONCLUSIONS AND DISCUSSION

The study of mechanics of fractures and joints can be approached at different levels. These include phenomenon logical approaches, which considers the behavior of a joint simply as a constitutive response, to more detailed approaches, which consider the joint surface topography, the nonlinear interaction and material phenomena associated with an interface. Current available computational methodologies can be utilized to conduct studies of both approaches. This thesis examines the study of mechanics of a joint from considerations of the joint surface profile and the nonlinear interactive and material behavior. The studies are focused on the examination of an actual experiment conducted on a dolerite joint by appeal to computational modelling. The findings of the research can be summaried according to the following:

(i) Experimental investigations show the important influences of surface roughness on the shear behavior of rock joints. In modelling a joint, the actual profile of the joint as determined from surface profiling is usually considered. There are, however, limitations to the degree of refinement that can be permitted if the results of profiling are to be used in the continuum computational modelling process. Constraints of continuum modelling place restrictions on the refinement of the profile to a scale, which is not representative of the requirements for computational modelling. The smallest element dimension cannot be smaller than the largest grain size of the parent geomaterial. In this thesis, the microstructure of the rock mass is disregarded and the smallest element size is chosen close to the grain size. In addition to these constraints, the finite element discretization of the region close to the joint front can be also, to a large extent, influenced by the capacity of the computational facilities to assure computational accuracy. By defining additional surface interaction properties, the influence of joint surface geometry can be incorporated in a computational modeling to account for the mechanical interaction between surfaces composing the joint. When rotation free contact is established between irregular surfaces, contact only occurs at limited points. Computational simulations indicate that interfacial behavior of sections of surface, excluding contacting points, has negligible effect on final shear behavior of the joint. Mechanical behavior of these limited contacting points therefore has a governing effect on the shear behavior of the entire joint. Dilatancy during shear, which is also influenced by the normal stress, roughly follows the surface geometry of the "*governing asperity*". Shear response is found to be identical for surface sections at different lengths, which includes the "*governing asperity*". A regular triangular joint with a same asperity angle as that of the "*governing asperity*" exhibits similar response of dilatancy and shear stress to those of the irregular joint. The process of establishing what is a governing asperity is not a routine. The factors influencing the selection of the governing asperity can include features such as the profile of joint and the steepest acute angle in the direction of movement.

(ii) In addition to the surface roughness, surface interaction properties need to be characterized to computationally model the shear behavior of rock joints. In considering the Coulomb friction model, the elastic interaction properties are assumed before surfaces slide relative to each other. These properties can be examined by consdering the shearing of two planar surfaces. The coefficient of friction can be obtained from the peak friction stress and the limiting frictional stiffness reflects the elastic behavior of contacts. The coefficient of friction has a direct influence on the peak shear stress of joint, and the frictional stiffness determines its overall shear stiffness. Most experiments, however, only pay attention to the coefficient of friction of joint surface and observations of the frictional stiffness are scarce.

(iii) Material properties required for computational simulation of the joint include Young's modulus, Possion's ratio and strength parameters applicable to a failure criterion. Both the compressive and tensile strength influences the development of plasticity during shear. Most experiments only provide information concerning the compressive strength of the intact material mass. The tensile strength can, however, be estimated by specifying a reasonable ratio between tensile strength and compressive strength generally applicable to brittle elastic solids.

(iv) Asperities exhibit failure during shear. The failure of asperities results in plastic deformations in the asperities, which is accompanied by plastic energy dissipation in parent material. The plastic energy dissipation is generally 1 to 2 orders smaller than the frictional energy dissipation, during shear on an irregular joint. When asperity angles are steep, relative shear does not induce large relative movement between two initially matched surfaces, and most energy will be instead expended by plastic energy dissipation in material. This corresponds to the behavior expected of a joint zone in a real rock mass, where asperities interlock firmly and the joint loses stability only as a result of plastic deformation in asperties when surfaces composing the joint are forced to experience relative movement.

(v) Experimental evidence shows that reduced volume of material due to the damage process and surface wearing process can reduce the dilatancy during shear. The gouge materials produced, which residue at the joint locations, can also reduce the dilatancy angle. In numerical modelling, however, continuum modelling does not allow consideration of the disintegration of damaged asperities and gouge material. Asperity failure in the form of plastic flow increases the element volume, which eventually increases the dilatancy during multi-cycle shear.

(vi) The normal stiffness k causes a greater suppression of dilatancy, which leads to the development of higher shear stresses during relative shear of an irregular joint. Numerical model also captures similar phenomena, and evolution of energy dissipation can be traced. Presence of normal stiffness leads to a greater frictional energy dissipation. Especially, the plastic energy dissipation in the parent material can be almost doubled in the presence of normal stiffness.

(vii) The hydraulic conductivity of a joint is related to its hydraulic aperture. The normal and shear action at a joint might close or open the aperture due to contraction or dilatancy. Consequently, the hydraulic properties can vary due to the changes of aperture. The variation of hydraulic conductivity follows closely with the variation of dilatancy during shear. The appearance of dilatancy, in the absence of opening between surfaces in contact, cannot be interpreted as an alteration in the hydraulic conductivity of the joint. Seperation at the joint in the form of gap development is a necessary prerequisite for altering of hydraulic conductivity. The material dilatancy can induce alterations in the hydraulic conductivity of the parent material but that changes are expected to be of secondary importance in comparison to the hydraulic conductivity changes associated with aperture opening.

REFERENCES

Ahmad, M. and Bangash, Y. (1987) A 3-D bond analysis using FEs, *Computers and Structures*, **25**, pp. 281-296.

Amadei, B. and Illangasekare, T. (1992) Analytical solutions for steady and transient flow in non-homogeneous and anisotropic rock joints, *Int. J. Rock Mech. Min. Sci. & Geomech. Abstr.*, **29**, pp. 561–572.

Armand, G., (2000) *Contribution à la caractérisation en laboratoire et à la modélisation constitutive du comportement mécanique des joints rocheux*, thèse de doctorat, L'université Joseph Fourier-Grenoble I.

Assonyi, C. (1979) *The Continuum Theory of Rock Mechanics*, Trans. Tech. Publications, Rockport, Mass.

Bandis, S. C., Lumsden, A.C., and Barton N. R. (1981) Experimental studies of scale effects on the shear behavior of rock joints, *Int. J. Rock Mech. Min. Sci. & Geomech. Abstr.*, **18**, pp. 1-21.

Bandis, S.C., Lumsden, A.C., and Barton, N.R. (1983) Fundamentals of rock joint deformation, *Int. J. Rock Mech. Min. Sci. & Geomech. Abstr.*, **20**, pp. 249-268.

Banerjee, P. K., Butterfield, R. (1981) *Boundary Element Methods in Engineering Science*, McGraw-Hill, London.

Barla, G., Forlati, F. and Zaninetti, A. (1985) Shear behavior of filled discontinuities, *Fundamentals of rock joints: proceedings of the International Symposium on Fundamentals of Rock Joints* (Stephansson, O., Eds.), Björkliden, Lulea, Centek, pp.163-172.

Barton, N.R. (1971) A relationship between joint roughness and joint shear strength, *Rock fracture: Proceedings of International Symposium on Rock Mechanics*, Nancy, France, papers 1-8.

Barton, N.R. (1973) Review of a new shear strength criterion for rock joints, *Engineering Geology*, **7**, pp. 287-332.

Barton, N.R. (1976) The shear strength of rocks and rock joints, *Int. Rock Mech. Min. Sci. & Goemech. Abstr.*, **13**, pp. 255-279.

Barton, N.R. (1986) Deformation phenomena in jointed rock, *Geotechnique*, **36**, pp. 147-167.

Barton, N.R., Bandis, S. and Bakhtar, K. (1985) Strength, deformation and conductivity coupling of rock joints, *Int. J. Rock Mech. Min. Sci. & Geomech. Abstr.,* **22**, pp. 121-140.

Barton, N.R. and Choubey, V. (1977) The shear strength of rock joints in theory and practice, *Rock Mechanics*, Springer, Vienna, **1**, pp.1-54.

Benjelloun, Z.H., Boulon, M. and Bilaux, D. (1990) Experimental and numerical investigation on rock joints, *Rock joints: proceedings of the International Symposium on Rock Joints* (Barton, N. and Stephansson, O., Eds.), Loen, Norway, Balkema, Rotterdam; Brookfield, pp. 171-178.

Benmokrane, B. and Ballivy, G. (1989) Laboratory study of shear behavior of rock joints under constant normal stiffness conditions, *Rock mechanics as a guide for efficient utilization of natural resources: proceedings of the 30th U.S. Symposium* (Khair, A.W., Eds.), West Virginia University, Balkema, Rotterdam; Brookfield, pp. 899-906.

Berry, M.V. and Lewis, Z.V. (1980) On the Weierstrass-Mandelbrot fractal function, *R. Soc. London Proc. Ser. A.*, **370**, pp. 459-484.

Billaux, D. and Gentier, S. (1990) Numerical and laboratory studies of flow in a fracture, *Rock joints: proceedings of the International Symposium on Rock Joints* (Barton, N. and Stephansson, O., Eds.), Loen, Norway, Balkema, Rotterdam; Brookfield, pp. 369–373.

Bobji, M.S., Shivakemar, K., Alehossein, H., Venkateshwarlu, V. and Biswas, S. K. (1999), Influence of surface roughness on the scatter in hardness measurements-a numerical study, *Int. Rock Mech. Min. Sci.*, **36**, pp. 399-404.

Boulon, M.J., Selvadurai, A.P.S., Benjelloun, H. and Feuga, B. (1993) Influence of rock joint degradation on hydraulic conductivity, *Int. Rock Mech. Min. Sci.*, **30**, pp.1311-1317.

Brady, B.H.G. and Brown, E.T. (1993) *Rock Mechanics*, second edition, Kluwer Academic, Boston.

Brown, S.R. (1987) Fluid flow through rock joints: the effect of surface roughness, *J. Geophys. Res.*, **92**, No. B2, pp. 1337-1347.

Brown, S.R. and Scholz, C.I.I. (1985) Broad band width study of the topography of natural rock surfaces, *J. Geophys. Res.*, **90**, pp. 12575-12582.

Byerlee, J.D. and Brace, W.F. (1968) Stick slip, stable sliding and earthquake effect of rock type, strain rate and stiffness, *J. Geophys. Res.*, **73**, pp. 6031-6037.

Carol, I. and Alonso, E.E. (1983) A new joint element for the analysis of fractured rock, *Proceedings of the 5th Congress of International Society for Rock Mechanics,* Melbourne, F147-F151.

Charlez, P.A. (1991) *Rock Mechanics*, Éditions Technip, Paris.

Chen, W.F. (1981) *Plasticity in Reinforced Concrete*, McGraw-Hill, New York.

Chen, W.F. (1994) *Constitutive Equations for Engineering Materials*, Elsevier, Amsterdam; New York.

Chen, Z., Narayan, S.P., Yang, Z. and Rahman, S.S. (2000) An experimental investigation of hydraulic behavior of fractures and joints in granitic rock, *Int. Rock Mech. Min. Sci.*, **37**, pp. 1061-1071.

Chryssanthakis, P. and Barton, N. (1990) Joint roughness (JRC_n) characterization of a rock joint and joint replica at 1 m scale, *Rock joints: proceedings of the International Symposium on Rock Joints* (Barton, N. and Stephansson, O., Eds.), Loen, Norway, Balkema, Rotterdam; Brookfield, pp. 27-33.

Coates, D. F., (1967) *Rock Mechanics Principles*, Queen's Printer, Ottawa.

Crouch, S. L., and Starfield, A. M. (1983) *Boundary Element Methods in Solid Mechanics*, Allen & Unwin, London.

Cundall, P.A. (1971) *The Measurement and Analysis of Acceleration in Rock Slopes*, Ph.D. thesis, University of London (Imperial College).

Cundall, P.A and Strack, O.D.L. (1979) A distinct element model for granular assemblies. *Geotechnique*, **29**, pp. 47–65, 1979.

Davis, R.O. and Selvadurai, A.P.S. (1996) *Elasticity and Geomechanics*, Cambridge University Press, Cambridge.

Desai, C. S. (2001) *Mechanics of Materials and Interfaces: The Disturbed State Concept*, CRC Press, Boca Raton, Fla.

Desai, C.S., Drumm, E.C. and Zaman, M.M. (1985) Cyclic testing and modeling of interfaces, *J. Geotech. Engng.*, ASCE, **111**, pp. 793-815.

Desai, C.S., Zaman, M.M., Lightner, J.G. and Siriwardane, H.J. (1984) Thin-layer element for interfaces and joints, *Int. Rock Mech. Min. Sci. & Goemech.*, **8**, pp. 19-43.

Dight, P.M. and Chiu, H.K. (1981) Prediction of shear behavior of joints using profiles, *Int. Rock Mech. Min. Sci. & Goemech. Abstr.*,**18**, pp. 369-388.

Doltsinis, I. St. (2000) *Elements of Plasticity: Theory and Computation*, WIT press, Boston.

Drucker, D.C. and Prager, W. (1952) Soil mechanics and plastic analysis or limit design, *Q. Appl. Math.*, **10**, pp.157-165.

Durham, W.B. and Bonner, B.P. (1992) Closure and fluid flow in discrete fractures, *Fractured and jointed rock masses: proceedings of the Conference on Fractured and Jointed Rock Masses* (Myer, L.R., Cook, N.G.W., Goodman, R.E. and Tsang, C.F., Eds.), Lake Tahoe, California, Balkema, Rotterdam; Brookfield, pp. 441-446.

Engelder, T. and Scholz, C.H. (1981) Fluid flow along a very smooth joints at effective pressure up to 200 megapascals, *Mechanical behavior of Crustal Rocks, Amer. Geophys. Union Monograph*, **24**, pp. 147.

Esaki, T., Du, S., Mitani, Y., Ikusada, K. and Jing, L. (1999) Development of a shear-flow test apparatus and determination of coupled properties for a single rock joint, *Int. Rock Mech. Min. Sci.*, **36**, pp. 641-650.

Esaki, T., Nakahara, K., Jiang, Y. and Mitani, Y. (1996) Effects of proceeding shear history on shear-flow coupling properties of rock, *Mechanics of jointed and faulted rock: proceedings of the Second International Conference on Mechanics of Jointed and Faulted Rock, MJFR-2* (Rossmanith, H.P., Eds.), Vienna, Austria, Balkema, Rotterdam; Brookfield, pp. 501–506.

Fakharian, K. and Evgin, E. (2000) Elasto-plastic modeling of stress-path-dependent behavior of interfaces, *Int. J. Numer. Anal. Meth. Geomech.*, **24**, pp.183-199.

Feder, J. (1988) *Fractals*, Plenum Press, New York.

Fishman, K.L. and Desai, C.S. (1987) A constitutive model for hardening behavior of rock joints, *Constitutive Laws for Engineering Materials: Theory and Application* (Desai, C.S., Eds.), University of Arizona, pp.1043-1050.

Fox, D.J., Kana, D.D. and Hsiung, S.M (2000) Influence of interface roughness on dynamic shear behavior in jointed rock, *Int. Rock Mech. Min. Sci.*, **35,** pp. 923-940.

Frank, P., Guenot, A. and Humbert, P. (1982) Numerical analysis of contacts in Ceomechnics, *Edmonton 1982: proceedings of the fourth International Conference on Numerical Methods in Geomechanics* (Eisenstein, Z., Eds.), Edmonton, Balkema, Rotterdam, **1**, pp.37-45.

Friedman, M., Perkins, R.D. and Green, S.J. (1970) Observation of brittle-formation features at the maximum stress of Westerly granite and Solenhofen limestone, *Int. Rock Mech. Min. Sci.*, **7**, pp.297-306.

Gangi, A.F. (1978) Variation of whole- and fractured-porous-rock permeability with confining pressure, *Int. Rock Mech. Min. Sci. & Goemech. Abstr.*, **15**, pp. 249-257.

Gens, A., Carol, I. and Alonso, E.E. (1995) Rock joints: FEM implementation and applications, Selvadurai, *Mechanics of Geomaterial Interfaces* (Selvadurai, A.P.S. and Boulon, M.J., Eds.), pp. 395-420.

Gentier S. (1986) *Morphologie et comportement hydromécanique d'une fracture naturelle dans le granite sous contrainte normale; étude expérimentale et théorique*. Documents du B.R.G.M. b 134, B.R.G.M., Orléans, France.

Gentier, S., Riss, J., Archambault, G., Flamand, R. and Hopkins, D. (2000) Influence of fracture geometry on shear behavior, *Int. Rock Mech. Min. Sci.*, **37**, pp. 161-174.

Geological Survey of New South Wales (1974) *Geology of the Wollongong, Kiama & Robertson 1:50000 Sheets: 9029-II 9028-I&IV*, Department of Mines, pp.179.

Goodman, R.E. (1970) *The deformability of joints, determination of the in-situ modulus of deformation of rocks*, special technical publication, ASTM, Philadelphia, No. 477, pp. 174-196.

Goodman, R.E. (1976) *Methods of Geological Engineering*, West Publishing Company, St. Paul.

Goodman, R.E. (1989) *Introduction to Rock Mechanics*, Wiley, New Work.

Goodman, R.E., Taylor, R.L. and Brekke, R.L. (1968) A model for the mechanics of jointed rock, *J. Soil Mech. and Found. Div.*, **94**, pp. 637-659.

Grabinsky, M.W. and Kamaleddine, F.F. (1997) Numerical analysis of an extended arrangement of periodic discrete fractures, *Int. J. Rock Mech. Min. Sci.*, **34:3–4**, Paper No. 109.

Handanyan, J.M., Danek, E.R., D'andrea, R.A. and Sage, J.D. (1990) The role of tension in failure of jointed rocks, *Rock joints: proceedings of the International Symposium on Rock Joints* (Barton, N. and Stephansson, O., Eds.), Loen, Norway, Balkema, Rotterdam; Brookfield, pp. 195-202.

Hencher, S.R. and Richards, L.R. (1989) Laboratory direct shear testing of rock discontinuities, *Ground Engineering*, pp. 24-31.

Hoek, E. (1977) Rock mechanics laboratory testing in the context of a consulting engineering organisation, *Int. J. Rock Mech. Min. Sci. & Geomech. Abstr.*, **14**, pp. 93-101.

Hoek, E. (1983) Strength of jointed rock masses, *Geotechnique*, **33**, pp.187-223.

Hoek, E. (1990) Estimating Mohr-Coulomb friction and cohesion values from the Hoek-Brown failure criterion, *Int. J. Rock Mech. Min. Sci. & Geomech. Abstr.*, **27**, pp. 227-229.

Homand-Etienne, F., Belem, T., Sabbadini, S., Shtuka, A. and Royer, J.J. (1995) Analysis of the evolution of rock joints morphology with 2-D autocorrelation (variomaps), *Applications of Statistics and Probability* (Lemaire, M., Favre, J.L. and Mébarki, A., Eds.), Balkema, Rotterdam, pp. 1229-1236.

Huang, X. (1990) *A Laboratory Study of the Mechanical Behavior of Rock Joints, with Particular Interest to Dilatancy and Asperity Surface Damage Mechanism*, Ph. D. thesis, University of Wisconsin Madison.

Huang, X., Haimson, B.C., Plesha, M.E. and Qiu, X. (1993), An investigation of the mechanics of rock joints - part I. Laboratory investigation, *Int. J. Rock Mech. Min. Sci. & Geomech. Abstr.*, **30**, No. 3, pp. 257-269.

Huang, S.L., Oelfke, S.M. and Speck, R.C. (1992) Application of fractal characterization and modeling to rock joint profiles, *Int. Rock Mech. Min. Sci. & Goemech. Abstr.*, **29**, No. 2, pp 89-100.

Huang, T.H. and Doong, Y.S. (1990) Anisotropic shear strength of rock joints, *Rock joints: proceedings of the International Symposium on Rock Joints* (Barton, N. and Stephansson, O., Eds.), Loen, Norway, Balkema, Rotterdam; Brookfield, pp. 211-218.

Indraratna, B. and Haque, A. (2000) *Shear Behavior of Rock Joints*, Balkema, Rotterdam; Brookfield.

Indraratna, B., Haque, A. and Aziz, N. (1998) Laboratory modelling of shear behavior of soft joints under constant normal stiffness condition, *J. Gotechnical and Geological Engineering*, **16**, pp. 17-44.

Indraratna, B., Haque, A. and Aziz, N. (1999) Shear behavior of idealised infilled joints under constant normal stiffness, *Geotechnique*, **49**, pp. 331-355.

International Society for Rock Mechanics, Commission on Standardization of Laboratory and Field Tests (1978) Suggested methods for the quantitative description of discontinuities in rock masses, *Int. Rock Mech. Min. Sci. & Goemech. Abstr.*, **15**, pp. 319-368.

Iwai, K. (1976*) Fundamental Studies of Fluid Flow in A Single Fracture,* Ph.D. thesis, University of California, Berkeley.

Iwano, M. and Einstein, H.H. (1995) Laboratory experiments on geometric and hydromechanical characteristics of three different fractures in granodioritc, *Proceedings of the Eighth International Congress on Rock Mechanics* (Fujui, T., Eds.*)*, **2**, Balkema, Rotterdam; Brookfield, pp. 743-750.

Jaeger, J.C. and Cook, N.G.W. (1976) *Fundamentals of Rock Mechanics*, Second edition, Wiley, New York.

Jing, L., Nordlund, E. and Stephansson, O. (1992) An experimental study on the anisotropy and stress-dependency of the strength and deformability of rock joints, *Int. J. Rock Mech. Min. Sci. & Geomech. Abstr.*, **29**, pp. 535-542.

Jumikis, A.R. (1983) *Rock Mechanics*, Trans. Tech., Clausthal, Germany.

Kachanov, L.M. (1971) *Foundations of the Theory of Plasticity*, North-Holland Pub. Co., Amsterdam.

Kanji, M.A. (1974) Unconventional laboratory tests for the determination of the shear strength of soil-rock contacts, *Proceedings of the 3rd Congress of International Society for Rock Mechanics,* Denver, **2**, pp. 241-247.

Kodikara, J. K. and Johnston, I.W. (1994) Shear behavior of irregular triangular rock-concrete joints, *Int. J. Rock Mech. Min. Sci. & Geomech. Abstr.*, **31**, pp. 313-322.

Krahn, J. and Morgenstern, N.R. (1979) The ultimate frictional resistance of rock discontinuities, *Int. Rock Mech. Min. Sci. & Goemech. Abstr.*, **16**, pp. 127-133.

Kranz, R.L., Frankel, A.D., Engelder, T. and Scholz, C.H. (1979) The permeability of whole and jointed barre granite, *Int. Rock Mech. Min. Sci. & Goemech. Abstr.*, **16**, pp. 225-234.

Kulatilake, P.H.S.W., Shou, G., Huang, T.H. and Morgan R.M. (1995) New peak shear strength criteria for anisotropic rock joints, *Int. Rock Mech. Min. Sci. & Goemech. Abstr.*, **32**, pp. 673-697.

Kwafniewski, M.A. and Wang, J.A. (1993) Application of laser profilometry and fractal analysis to measurement and characterisation of morphological features of rock fracture surfaces, *Géotechnique et Environnement, Vandouvre-les-Nancy, Sciences de la Terre* (Piguet, J.P. and Homand, F., Eds.), pp. 163-196.

Kwafniewski, M.A. and Wang, J.A. (1997) Surface roughness evolution and mechanical behavior of rock joints under shear, *Int. J. Rock Mech. Min. Sci.*, **34:3–4**, Paper No. 157.

Ladanyi, H. K. and Archambault, G. (1977) Shear strength and deformability of filled indented joints, *International Symposium: the Geotechnics of Structurally Complex Formations* (Associazione geotecnica italiana, Eds.), Capri, pp. 371-326.

Lama, R.D. (1978) Influence of clay fillings on shear behavior of joints, *Proceedings of the 4th International Conference on Rock Mechanics*, Montreux, **1**, pp. 221-227.

Lee, S.D., Lee, C.I. and Park, Y. (1997) Characterisation of joint profiles parameters, *Int. J. Rock Mech. Min. Sci.*, **34:3–4**, Paper No. 174.

Lee, Y.H., Carr, J.R., Barr, D.J. and Haas, C.J. (1990) The fractal dimension as a measure of the roughness of rock discontinuity profile, *Int. Rock Mech. Min. Sci. & Goemech. Abstr.*, **27**, pp. 453-464.

Leichnitz, W. (1985) Mechanical properties of rock joints, *Int. Rock Mech. Min. Sci. & Goemech. Abstr.*, **22**, pp. 313-321.

Maclaughlin, M.M. and Sitar, N. (1996) Rigid body rotations in DDA, *Discontinuous deformation analysis (DDA) and simulations of discontinuous media: proceedings of the first International Forum on Discontinuous Deformation Analysis (DDA) and Simulations of Discontinuous Media* (Salami, M.R., Banks, D.C. and Shi, G.H., Eds), Berkeley, California, USA, TSI Press, Albuquerque, N.M.

MacKenzie, W. S. (1994) *A Color Atlas of Rocks and Minerals in Thin Section*, Wiley, New York.

Maerz, N.H., Franklin, J.A. and Bennett, C.P. (1990) Joint roughness measurement using shadow profilometry, *Int. Rock Mech. Min. Sci. & Goemech. Abstr.*, **27**, pp. 329-343.

Makurat, A., Barton, N., Rad, N.S. and Bandis, S. (1990) Joint conductivity due to normal and shear deformation, *Rock joints: proceedings of the International Symposium on Rock Joints* (Barton, N. and Stephansson, O., Eds.), Loen, Norway, Balkema, Rotterdam; Brookfield, pp. 535–540.

Malinverno, A. (1990) A simple method to estimate the fractal dimension of a self-affinity series, *Geophys. Res. Lett.*, **17**, pp. 1953-1956.

Mandelbrot, B.B. (1983) *The Fractal Geometry of Nature*, W. Freeman, San Francisco.

Matsushita, M. and Luchi, S. (1989) On the self affinity of various curves, *Physica D.*, **38**, pp.246-251.

Miller, S.M., McWilliams, P.C. and Kerkering, J.C. (1990) Ambiguities in estimating fractal dimensions of rock fracture surfaces, *Rock Mechanics: Contributions and Challenges: proceedings of the 31st U.S. Symposium* (Hustrulid, A. and Johnson, G.A., Eds.), Colorado School of Mines, Golden, Balkema, Rotterdam; Brookfield, pp. 471-478.

Navayogarajah, N., Desai, C.S. and Kiousis, P.D. (1992) Hierarchical single-surface model for static and cyclic behaviour of interfaces, *J. Engng. Mech.*, **118**, No. 5, pp. 990-1011.

Nguyen, T.S. and Selvadurai, A.P.S. (1998) A model for coupled mechanical and hydraulic behavior of a rock joint, *Int. J. Numer. Analyt. Meth. Geomech.*, **22**, pp. 29-48.

Odling, N.E. (1994) Natural fracture profiles, fractal dimension and joint roughness coefficients, *Rock Mechanics and Rock Engineering*, **27**, pp. 246-251.

Ohnishi, Y. and Dharmaratne, P.G.R. (1990) Shear behavior of physical models of rock joints under constant normal stiffness conditions, *Rock joints: proceedings of the International Symposium on Rock Joints* (Barton, N. and Stephansson, O., Eds.), Loen, Norway, Balkema, Rotterdam; Brookfield, pp. 267-274.

Ohnishi, Y. and Yoshinaka, R. (1992) Laboratory investigation of scale effect in mechanical behavior fo rock joint, *Mechanics of jointed and faulted rock: proceedings of the Second International Conference on Mechanics of Jointed and Faulted Rock, MJFR-2* (Rossmanith, H.P., Eds.), Vienna, Austria, Balkema, Rotterdam; Brookfield, pp. 465-470.

Ohnishi, Y., Yamamukai, K. and Chen, G.Q. (1996) Application of DDA in rock fall analysis, *Rock Mechanics: Tools and Techniques: proceedings of the 2nd North American Rock Mechanics Symposium* (Aubertin, M., Hassani, F. and Mitri, H., Eds.), Montréal, Balkema, Rotterdam; Brookfield, pp. 2031-2037.

Olsson, W.A. and Brown, S.R. (1993) Hydromechanical response of a fracture undergoing compression and shear, *Int. Rock Mech. Min. Sci. & Goemech. Abstr.*, **30**, No. 7, pp. 845-851.

Orey, S. (1970) Gaussian simple functions and Haushoff dimension of level crossing, *Z. Wahrscheinlichkeitstheor. Verw. Gebiete*, **15**, pp. 249-256.

den Outer, A., Kaashoek, J.F. and Hack, H.R.G.K. (1995) Difficulties with using continuous fractal theory for discontinuity surfaces, *Int. Rock Mech. Min. Sci. & Goemech. Abstr.*, **32**, pp 3-10.

Pande, G.N , Beer, G., Williams, J.R. (1992) *Numerical Methods in Rock Mechanics*, Wiley, Chichester; New York.

Patton, F.D. (1966) Multiple modes of shear failure in rock, *Proceeding of the First Congress of International Society of Rock Mechanics,* Laboratório nacional de engenharia civil, Lisboa, **1**, pp. 509-513.

Pereria, J.P. (1990) Shear behavior of filled discontinuities, *Rock joints: proceedings of the International Symposium on Rock Joints* (Barton, N. and Stephansson, O., Eds.), Loen, Norway, Balkema, Rotterdam; Brookfield, pp. 283-287.

Pereria, J.P. (1997) Rolling friction and shear behavior of rock continuities filled with sand, *Int. J. Rock Mech. Min. Sci.*, **34:3–4**, Paper No. 244.

Phien-wej, N., Shrestha, U.B. and Rantucci, G. (1990) Effect of infill thickness on shear behavior of rock joints, *Rock joints: proceedings of the International Symposium on Rock Joints* (Barton, N. and Stephansson, O., Eds.), Loen, Norway, Balkema, Rotterdam; Brookfield, pp. 289-294.

Plesha, M.E. (1987) Constitutive models for rock discontinuities with dilatancy and surface degradation, *Int. J. Numer. Analyt. Meth. Geomech.*, **11**, pp. 345-362.

Power W.L. and Tullis T.F. (1991) Euclidean and fractal models for the description of rock surface roughness, *J. Geophys. Res.,* **96**, pp. 415-424.

Prager, W. (1959) *An Introduction to Plasticity*, Addison-Wesley Pub. Co., Reading, Mass.

Prager, W. and Hodger, P.G. (1951) *Theory of Perfectly Plastic Solids*, Wiley, New York.

Pyrak-Nolte, L.J and Morris, J.P. (2000) Single fractures under normal stress: The relation between fracture specific and fluid flow, *Int. Rock Mech. Min. Sci.,* **37**, pp. 245-262.

Pyrak-Nolte, L.J., Myer, L.R. and Cook, N.G.W. and Witherpoon, P.A. (1987) Hydraulic and mechanical properties of natural joints in low permeability rock, *Proceeding of the Sixth International Congress on Rock Mechanics* (Herget, G. and Vongpaisal, S., Eds.), Montreal, Balkema, Rotterdam, pp. 225-231.

Raven, K.G. and Gale, J.E. (1985) Water flow in a natural rock fracture as a function of stress and sample size, *Int. J. Rock Mech. Min. Sci. & Geomech. Abstr.,* **22**, pp. 251–261.

Re, F., Scavia, C. and Zaninetti, A. (1997) Variation in contact areas of rock joint surfaces as a function of scale, *Int. J. Rock Mech. Min. Sci.*, **34:3–4**, Paper No. 254.

Roberds, W.J. and Eistein, H.H. (1978) Compressive model for rock discontinuities, *J. Geotech. Engng.*, **104**, pp. 553-569.

Roberds, W.J., Iwano, M. and Einstein, H.H. (1990) Probabilistic mapping of rock joint surfaces, *Rock joints: proceedings of the International Symposium on Rock Joints* (Barton, N. and Stephansson, O., Eds.), Loen, Norway, Balkema, Rotterdam; Brookfield, pp. 681-692.

Sabbadini, S. (1994) *Analyses geostatistique et fractale de l'évolution de la morphologie de discontinuités au cours du cisaillement,* Thèse doctorat, Génie Civil et Minier, Nancy, France.

Sabbadini, S., Homand-Etienne, F. and Belem, T. (1995) Fractal and geostatistical analysis of rock joint roughness before and after shear tests, *Mechanics of jointed and faulted rock: proceedings of the Second International Conference on Mechanics of Jointed and Faulted Rock, MJFR-2* (Rossmanith, H.P., Eds.), Vienna, Austria, Balkema, Rotterdam; Brookfield, pp. 535–541.

Saeb, S. and Amadei, B. (1992) Modelling rock joints under shear and normal loading, *Int. J. Rock Mech. Min. Sci. & Geomech. Abstr.*, **29**, pp. 267-278.

Schweiger, H.F., Haas, W. and Handle, E. (1990) A thin-layer element for modelling joints and faults, *Mechanics of jointed and faulted rock: proceedings of the Second International Conference on Mechanics of Jointed and Faulted Rock, MJFR-2* (Rossmanith, H.P., Eds.), Vienna, Austria, Balkema, Rotterdam; Brookfield, pp. 559-564.

Seidel, J.P. and Haberfield, C.M. (1995) The use of fractal geometry in a joint shear model, *Mechanics of jointed and faulted rock: proceedings of the Second International Conference on Mechanics of Jointed and Faulted Rock, MJFR-2* (Rossmanith, H.P., Eds.), Vienna, Austria, Balkema, Rotterdam; Brookfield, pp.529-534.

Selvadurai, A.P.S. (1995) The role of geomaterial interface degradation on the mechanics of a fracture, *Mechanics of jointed and faulted rock: proceedings of* *the Second International Conference on Mechanics of Jointed and Faulted Rock, MJFR-2* (Rossmanith, H.P., Eds.), Vienna, Austria, Balkema, Rotterdam; Brookfield, pp.1031-1038.

Selvadurai, A.P.S. (2000) *Partical Differetial Equations in Mechanics*, **2**, Springer, Berlin; New York.

Selvadurai, A.P.S. and Au, M.C. (1987) Boundary element modelling of interface phenomena, *Topics in Boundary Element Research*, Ch. 5, Brebbia, C.A. (Eds.), Springer Verlag, Berlin, pp. 112-126.

Selvadurai, A.P.S. and Boulon, M.J. (Eds.) (1995) *Mechanics of Geomaterial Interfaces*, Elsevier, Amsterdam; New York.

Selvadurai, A.P.S. and Sepehr, K. (1997) Discrete element modelling of pipe uplift in frozen soil regimes, *Ground Freezing* (Knusson, S., Eds.), Balkema, Rotterdam, pp. 479-486.

Selvadurai, A.P.S. and Sepehr, K. (1998) Fragmentation modes for impacting ice floes, *Ice in Surface Waters* (Shen, H.T., Eds.), Balkema, Rotterdam pp. 483-489.

Selvadurai, A.P.S. and Sepehr, K. (1999) Two-dimensional discrete element simulations of ice-structure interaction, *Int. J. Solids and Struct.*, **36**, pp. 4919-4940.

Selvadurai, A.P.S. and Voyiadjis, G.Z. (Eds.) (1986) *Mechanics of Material Interfaces*, Elsevier, New York; Amsterdam.

Shi, G.H. (1988) *Discontinuous Deformation Analysis: A New Numerical Model for the Statics and Dynamics of Block Systems*, Ph.D. thesis, Department of Civil Engineering, University of California, Berkeley.

Shirono, T. and Kulatilake, P.H.S.W. (1997) Accuracy of the spectral method in estimating fractal/spectral parameters for self-affine roughness profiles, *Int. Rock Mech. Min. Sci. & Goemech. Abstr.*, **34**, pp. 789-804.

Skinas, C.A., Bandis, S.C. and Demiris, C.A. (1990) Experimental investigations and modeling of rock joint behavior under constant stiffness, *Rock joints: proceedings of the International Symposium on Rock Joints* (Barton, N. and

Stephansson, O., Eds.), Loen, Norway, Balkema, Rotterdam; Brookfield, pp. 301-308.

Snow, D.T. (1965) *A Parallel Plate Model of Fractured Permeable Media*, Ph.D. thesis, University of California, Berkeley.

Swan, G. and Zongqi, S. (1985) Prediction of shear behavior of joints using profiles, *Rock Mechanics and Rock Engineering*, **18**, pp. 183-212.

Thomas, S. K. L. and Johnston, I.W. (1987) Shear behavior of regular triangular concrete/rock joints-evaluation, *Journal of Geotechnical Engineering*, **115**, No. 5, May, pp. 728-741.

Thomas, T. Y. (1961) *Plastic Flow and Fracture in Solids*, Academic Press, New York.

Timushenko, G. and Goodier, J.N. (1970) *Theory of Elasticity*, McGraw-Hill, New York.

Toledo, P.E.C. and de Freitas, M.H. (1992) The peak shear strength of filled joints, *Mechanics of jointed and faulted rock: proceedings of the Second International Conference on Mechanics of Jointed and Faulted Rock, MJFR-2* (Rossmanith, H.P., Eds.), Vienna, Austria, Balkema, Rotterdam; Brookfield.

Tsang, Y.W. and Tsang, C.F. (1987) Channel model of flow through fractured media, *Water Resources Res.,* **23**, pp. 467.

Tse, R. and Cruden, D.M. (1979) Estimating joint roughness coefficients, *Int. Rock Mech. Min. Sci. & Goemech. Abstr.*, **16**, pp. 303-307.

Turk, N., Grieg, M.J., Dearman, W.R. and Amin, F.F. (1987) Characteriztion of rock joint surfaces by fractal dimension, *Rock Mechanics: proceedings of 28th U.S. Symposium* (Farmer, I.W., Eds.), University of Arizona, Balkema, Boston, pp.1223-1236.

Van Sint Jan, M.L. (1990) Shear tests of model rock joints under stiff normal loading, *Rock joints: proceedings of the International Symposium on Rock Joints* (Barton, N. and Stephansson, O., Eds.), Loen, Norway, Balkema, Rotterdam; Brookfield, pp. 323-328.

Wahlstrom, E.E. (1947) *Igneous Minerals and Rocks*, Wiley, New York.

Wakabayashi, N. and Fugushige, I. (1995) Experimental study on the relation between fractal dimension and shear strength, *Mechanics of jointed and faulted rock: proceedings of the Second International Conference on Mechanics of Jointed and Faulted Rock, MJFR-2* (Rossmanith, H.P., Eds.), Vienna, Austria, Balkema, Rotterdam; Brookfield, pp. 119-124.

Wawerisk, W.R. and Fairhurst, C. (1970) A study of brittle rock failure in laboratory compression experiments, *Int. Rock Mech. Min. Sci. & Goemech. Abstr.*, **7**, pp.561-575.

Westergaard, H.M. (1952) *Theory of Elasticity and Plasticity*, Dover Publications, New York.

Wibowo, J.T., Amadei, B., Sture, S., Robertson, A.B. and Price, R. (1992) Shear response of a rock under different boundary conditions: A experimental study, *Mechanics of jointed and faulted rock: proceedings of the Second International Conference on Mechanics of Jointed and Faulted Rock, MJFR-2* (Rossmanith, H.P., Eds.), Vienna, Austria, Balkema, Rotterdam; Brookfield, pp. 425-430.

Williams, J.R. and Mustoe, G.G.W. (Eds.) (1993) *Proceedings of the 2nd International Conference on Discrete Element Methods (DEM)*, Massachusetts Institute of Technology, IESL Publications.

Williams, J.R., Hocking, G. and Mustoe, G.G.W. (1985) The theoretical basis of the discrete element method, *Proceedings of the 1985 Conference on Numerical Methods in Engineering, Theory and Application*, pp. 897–906.

Wills-Richards, J., Watanabe, K and Takahashi, H. (1996) Progress toward a stochastic rock mechanics model of engineered geothermal system. *J. Geophys. Res.*, **101**, pp. 17481-17496.

Wischers, G. (1978) Application of effects of compressive loads on concrete, *Betontech., Ber.*, Nos. 2 and 3, Duesseldorf.

Witherpoon, P.A., Wang, J.S., Iwai, K. and Gale, J.E. (1980) Validity of cubic law for fluid flow in a deformable rock fracture, *Water Resources Res.*, **16**, pp. 1016-1024.

Wu, H. and Ali, M. (1978) Statistical representation of joint roughness, *Int. Rock Mech. Min. Sci. & Goemech. Abstr.*, **15**., pp 259-262.

Xie, H. (1993) *Fractals in Rock Mechanics*, Balkema, Rotterdam/Brookefield.

Xie, H. and Pariseau, W.G. (1994) Fractal estimation of joint roughness coefficient, *Sci. China Ser. B.*, **37**, pp. 1269-1275.

Xie, H., Wang, J.A. and Xie W.H. (1997a) Fractal effects of surfaces roughness on the mechanical behavior of rock joints, *Chaos, Solitons & Fractals*, **8**, pp. 221-252.

Xie, W. H., Li, H.Q., Zhang, Y, Z and Li, S. P. (1997b) A photoelastic investigation on the effect of roughness on the stress field of fractal rock joint, *Int. J. Rock Mech. Min. Sci.*, **34:3–4**, Paper No. 341.

Yeo, W.I., Freitas, M.H.D. and Zimmerman, R.W. (1998) Effect of shear displacement on the aperture and permeability of a rock fracture, *Int. Rock Mech. Min. Sci.*, **35**, pp. 1051-1070.

Yoshinaka, R., Yoshida, J., Shimizu, T., Arai, H. and Arisaka, S. (1991) Scale effect in shear strength and deformability of rock joints, *Proeeding of the 7th Congress of International Society for Rock Mechanics*, Aachen, West Germany, Central Borad of Irrigation & Power, New Delhi, pp. 371-374.

Yu, X. and Vayssade, B. (1991) Joint profiles and their roughness parameters, *Int. Rock Mech. Min. Sci. & Geomech. Abst.*, **28**, pp. 333-336.

Zimmerman, R.W., Kumar, S. and Bodvarsson, G.S. (1991) Lubrication theory analysis of the permeability of rough-walled fractures, *Int. Rock Mech. Min. Sci. & Goemech. Abst.*, **28**, pp. 325-331.

Zienkiewicz, O. C. and Taylor, R.L. (2000) *The Finite Element Method*, fifth edition, Vol. **2**, Butterworth-Heinemann, Oxford.

Zienkiewicz, O.C., Best, B., Dullage, C. and Stagg, K.G. (1970) Analysis of nonlinear problems in rock mechanics with particular reference to jointed rock systems, *Proceednigs of the 2nd Congress of International Society for Rock Mechanics,* Beograd, "Jaroslav Cerni" Institute for Development of Water Resources, Beograd, **2**, pp.501-509.